Author:
Lewis, Tim D

Title:
Development of inerter-based suspension systems for railway vehicles

Development of Inerter-Based Suspension Systems for Railway Vehicles

Timothy D. Lewis

Department of Mechanical Engineering
University of Bristol

A dissertation submitted to the University of Bristol in accordance with the requirements for award of the degree of Doctor of Philosophy in the Faculty of Engineering.

December 2019

Word count: 50,000

Abstract

The suppression of unwanted railway vehicle vibrations and the reduction of maintenance costs associated with tracks and wheels are two vitally important objectives for the railway industry. The trade-off between passenger comfort and trackwear, which has long plagued railway vehicle dynamicists, arises from the Primary Yaw Stiffness's propensity to inhibit the wheelsets to yaw, increasing slip and hence increasing forces at the wheel-rail contact patch, yet decreasing the acceleration of the carbody. Active railway vehicle control methods have successfully been implemented, to reduce the need for a high Primary Yaw Stiffness. However, with the introduction of the inerter, scope for passive control, which does not run the risk of measurement error or require power input to deliver similar benefits, has greatly expanded. This thesis studies the extent to which the inerter can be of benefit to both the curving and straight running performance of railway vehicles, by way of the optimisation of inertance-integrated passive suspension layouts. A variety of modelling approaches are employed, most notably numerical simulation and optimisation in MATLAB®, and more accurate, nonlinear analysis using the multi-body railway vehicle modelling software VAMPIRE®.

A two-axle railway vehicle model is considered in MATLAB®. Straight running and curving performance is analysed by respectively subjecting the vehicle to a variety of straight, rough tracks, and a curve defined by ramped cant and curvature inputs. It is shown that the trade-off between passenger comfort and trackwear can be improved through the use of optimised, inertance-integrated lateral suspensions, with a further improvement discovered when an optimised HALL-Bush structure is used in the longitudinal direction. With the aim of validating the initial results, a location matrix technique of dynamic system simulation is developed which enables Laplace domain optimisations to take place on linearised VAMPIRE® models.

The final section of this thesis combines MATLAB® and VAMPIRE®, for respectively optimisation and multi-body dynamics modelling purposes. It demonstrates that the Primary Yaw Stiffness of a four-axle, industrial railway vehicle model can be significantly lowered, hence wheel and track maintenance costs decreased, whilst optimised inertance-integrated primary suspensions enable the ride quality to remain satisfactory. The structure-immittance approach to network-synthesis is used to identify beneficial suspension configurations, and numerous contact conditions and velocities are considered in the optimisation to cover a wide range of operating conditions. Further reality checks are performed on the vehicles with beneficial suspension configurations, the results of which reveal no significant detriment to other performance indices.

The findings of this project form an intermediate step towards the anticipated adoption of inertance-integrated suspension systems by the railway industry. These devices, if tailored and incorporated correctly, have the potential to significantly reduce track and wheel maintenance costs, as well as improve stability for future generations of rolling stock.

Author's declaration

I declare that the work in this dissertation was carried out in accordance with the requirements of the University's Regulations and Code of Practice for Research Degree Programmes and that it has not been submitted for any other academic award. Except where indicated by specific reference in the text, the work is the candidate's own work. Work done in collaboration with, or with the assistance of, others, is indicated as such. Any views expressed in the dissertation are those of the author.

SIGNED:

DATE:

Acknowledgements

I would like to take this opportunity to thank everyone who has helped, supported and encouraged me throughout my postgraduate period at the University of Bristol.

I will begin by thanking my supervisor, Dr. Jason Zheng Jiang. I have profoundly appreciated his continued help and dedicated support throughout my PhD and my fourth year undergraduate project, and thank him also for providing numerous opportunities for academic and industrial collaboration. I would also like to thank my co-supervisor and undergraduate tutor, Prof. Simon Neild, for his valuable discussions, guidance, and enthusiasm during both my undergraduate and postgraduate University years. I also extend my thanks to my supervisors for supporting me through my 3rd year undergraduate summer project, and inspiring me to pursue a research doctorate.

I have benefited from both academic and industrial collaboration during my PhD, and therefore I extend my thanks to Prof. Malcolm Smith, Prof. Roger Goodall, Prof. Simon Iwnicki, Dr. Yunshi Zhao, Dr. Cencen Gong, and Neil Dinmore for their technical advice, support and valuable discussions during meetings. Most notably I would like to express my gratitude to Dr. Gareth Tucker, for his close support and collaboration at the University of Huddersfield, and Dr. Yuan Li for her dedicated assistance and advice at Bristol.

I would like to thank Dr. Irina Lazar, Dr. Alicia Gonzalez-Buelga, Dr. Brano Titurus, Rory White, Dr. Chris Szczyglowski, Dr. Robert Dibble, Chris Mair, Dr. Tom Hill and Dr. Robert Wragge-Morley for being such excellent colleagues outside my PhD at the Univeristy, also Dr. Andrew Harrison and Dr. Djamel Rezgui for guiding me through the review process so swimmingly, and Prof. David Stoten for introducing me to the ACT Laboratory back in November 2015, advocating numerous mandatory coffee sessions.

From a personal point of view, thank you to friends and colleagues in the lab for making the place such a pleasant environment in which to carry out research. From the Dynamics and Control Group, I would like to mention Yi-Yuan Li, Ming Zhu, Hui Yuan, Dr. Ying Zhang, Duanqi Zhao, Dr. Jiannan Luo and Dr. Xiaofu Lu, and more generally, all friends and colleagues from ACT Lab East, West, and outside the academic sphere.

Finally, I acknowledge the EPSRC for funding this project, and would like to thank both of my parents for their ongoing and steadfast support throughout every aspect of my life.

Publications

Journal publications

- T. D. Lewis, J. Z. Jiang, S. A. Neild, C. Gong, and S. D. Iwnicki. Using an inerter-based suspension to improve both passenger comfort and track wear in railway vehicles. *Vehicle System Dynamics: International Journal of Vehicle Mechanics and Mobility*, 2019.
- T. D. Lewis, Y. Li, G. J. Tucker, J. Z. Jiang, Y. Zhao, S. A. Neild, M. C. Smith, R. Goodall, N. Dinmore. Improving the track friendliness of a four-axle railway vehicle using an inertance-integrated lateral primary suspension. *Vehicle System Dynamics: International Journal of Vehicle Mechanics and Mobility*, 2019.

Conference papers

- Y. Zhang, T. D. Lewis, J. Z. Jiang, and S. A. Neild. Passive vibration suppression using multiple inerter-based devices for a multi-storey building structure. *Proceedings of the 6th European Conference on Structural Control (EACS)*, 2016.
- T. D. Lewis, J. Z. Jiang, S. A. Neild, C. Gong, and S. D. Iwnicki. Improving ride comfort and trackwear of two-axle railway vehicles using inerter-based lateral suspension layouts. *Proceedings of the 6th Conference; Noise and Vibration Emerging Methods (NOVEM)*, 2018.
- T. D. Lewis, Y. Li, J. Z. Jiang, S. A. Neild, G. J. Tucker, S. Iwnicki, R. Goodall, M. C. Smith. Enabling the optimisation of the primary suspension with passive components for an industrial railway vehicle model. *Proceedings of the 28th International Conference on Noise and Vibration Engineering (ISMA)*, 2018.
- T. D. Lewis, Y. Li, G. J. Tucker, J. Z. Jiang, S. A. Neild, M. C. Smith, R. Goodall, S. Iwnicki, N. Dinmore. Inertance-integrated primary suspension optimisation on an industrial railway vehicle model. *Proceedings of the 26th IAVSD International Symposium on Dynamics of Vehicles on Roads and Tracks (IAVSD)*, 2019.

Contents

List of figures

List of tables

Nomenclature

General notations

$\ddot{\alpha}$	The second derivative of α, with respect to time
$\dot{\alpha}$	The first derivative of α, with respect to time
λ	Wheel conicity
$\tilde{\alpha}$	The Laplace transform of α
b	General inertance term
c	General damping term
g	Acceleration due to gravity (9.8ms^{-2})
I	Identity matrix
k	General stiffness term
s	Laplace variable
t	Time
T_γ	Frictional energy lost at the wheel-rail contact patch, see Eq. (3.34)

Literature review

A_1	Cross-sectional area of main cylinder
A_2	Cross-sectional area of helical tubing
F	Applied force
K	Static stiffness
$L(s)$	Laplace domain immittance function of an optimisable suspension structure
m	Mass of fluid in the helical tubing

N_f	RCF damage index parameter
u	Relative velocity between the suspension structure's terminals
v_1	Velocity of inerter terminal 1
v_2	Velocity of inerter terminal 2

Two-axle vehicle analysis

λ_0	Base cone profile
μ	Coefficient of friction between the wheels and track
ν	Poisson's ratio of steel
θ	The yaw DOF
θ_{c1}	Cant angle of curved track at front wheelset
θ_{c2}	Cant angle of curved track at rear wheelset
$A(s)$	System matrix, see Eq. (3.10)
a_c	Contact angle constant
$A_c(t)$	Carbody acceleration timeseries
A_l	Lateral track roughness factor
ab	Elliptical contact patch dimension product
B	The general input matrix, see Eq. (3.9)
B_c	The input matrix, specific to curving conditions, see Eq. (3.15)
B_s	The input matrix, specific to straight running conditions, see Eq. (3.14)
b_{syp}	A parallel inerter within a lateral suspension network, see Fig. 4.1
b_{sy}	A series inerter within a lateral suspension network, see Fig. 4.1
C_{11}	Longitudinal Kalker coefficient
C_{22}	Lateral Kalker coefficient
C_{23}	Spin Kalker coefficient
c_{sx}	A damper within a longitudinal suspension network, see Fig. 4.1
c_{sx}	Default longitudinal damping per axle box
c_{sy}	A damper within a lateral suspension network, see Fig. 4.1

c_{sy}	Default lateral damping per axle box
E	Young's modulus of steel
f_s	Spatial frequency (cycles/m), see Eq. (3.19)
f_{11}	Longitudinal creep coefficient
f_{22}	Lateral creep coefficient
f_{23}	Spin creep coefficient
F_x	Longitudinal creep force
F_y	Lateral creep force
$G(j\omega)$	Transfer function with an input of the lateral track displacement at the front wheelset, and an output of the lateral carbody acceleration
$H_1(s)$	Filter, see Eq. (3.21)
H_ω	Overall system transfer function, see Eq. (3.16)
I_v	Carbody yaw inertia
I_w	Wheelset yaw inertia
J_{5y}	Root Mean Square carbody acceleration
K_x	Default longitudinal stiffness per axle box
K_y	Default lateral stiffness per axle box
k_{sx}	A dynamic spring within a longitudinal suspension network, see Fig. 4.1
k_{sy}	A spring within a lateral suspension network, see Fig. 4.1
l_x	Semi-lateral spacing of longitudinal suspension connections
l_{wx}	Half the wheelset spacing
l_{wy}	Half the vehicle gauge
$L_{xi}(s)$	The j^{th} longitudinal suspension layout (see Fig. 4.1)
$L_{yi}(s)$	The i^{th} lateral suspension layout (see Fig. 4.1)
m_v	Carbody mass
m_w	Wheelset mass
N	Normal force at the contact patch
P	The cost function representing the dimensionless reduction in the average carbody acceleration for both real track inputs, see Eq. (4.7)

r_0	Nominal wheel radius
R_1	Radius of curved track at front wheelset
R_2	Radius of curved track at rear wheelset
$S_y(f_s)$	Single sided power spectrum, see Eq. (3.19)
T_d	Time delay between the front and rear wheelsets, at velocity V
u	Input timeseries of either lateral track displacements or cant and radius of curvature information, for respectively straight running and curving conditions
V	Vehicle forward speed
V_{op}	Vehicle nominal operational velocity
v_x	Longitudinal creepage
v_y	Lateral creepage
v_z	Spin creepage
x	The longitudinal direction (in the direction of travel) and the state matrix
y	The lateral direction, perpendicular t the direction of travel in the horizontal plane
y_{t1}	Lateral track displacement at front wheelset
y_{t2}	Lateral track displacement at rear wheelset
z	The vertical direction

Location matrix method

κ	The diagonal Single Value Decomposition matrix, see Eq. (5.50)
ϕ	The highest power of s on the denominator of $Y'(s)$, see Eq. (5.6)
ψ	The highest power of s on the numerator of $Y'(s)$, see Eq. (5.6)
Σ	The diagonal eigenvalue matrix, see Eq. (5.51)
$\underline{u}$	Input matrix
$\underline{x}$	State matrix
$\underline{z}$	Forces provided by $Y(s)$
A_1, b_1, c_1, d_1	The non-unique canonical decomposition matrices, see Eq. (5.7)

A_{ss}	The system matrix, see Eq. (5.36)
B	Input coefficient matrix
B_{ss}	The input coefficient matrix, see Eq. (5.36)
C_0	System damping matrix
C_0'	Modified damping matrix, see Eq. (5.34)
F_i	Net force exerted on the i^{th} device
F_{fi}	Net fictitious force exerted on the i^{th} device
K_0	System stiffness matrix
L_m	Location matrix, identifying coupling locations and coefficients corresponding to the addition to the model of the $Y(s)$ suspension.
M_0	System mass matrix
M_0'	Modified stiffness matrix, see Eq. (5.33)
Q	The transformation matrix; such that $Q = U^T V^{-T}$
U	A decomposition of L_m, such that $L_m = UU^T$
U_e	From the eigenvalue decomposition Eq. (5.51)
U_s	From the eigenvalue decomposition Eq. (5.48)
V	A decomposition of L_m, such that $L_m = VV^T$
V_s	From the eigenvalue decomposition Eq. (5.48)
w_f	Fictitious state
X	The state matrix, see Eq. (5.40)
$Y'(s)$	Force to acceleration transfer function across the $Y(s)$ suspension network
$Y(s)$	The admittance function of the suspension network being investigated
$\alpha_{1\ldots p}$	$Y'(s)$ denominator coefficients, see Eq. (5.6)
$\beta_{0\ldots p}$	$Y'(s)$ numerator coefficients, see Eq. (5.6)
Δa_i	Relative change in acceleration between the DOFs associated with the i^{th} device
Δa_{fi}	Relative change in acceleration between the fictitious DOFs associated with the i^{th} device
Δv_i	Relative change in velocity between the DOFs associated with the i^{th} device

Δv_{fi}	Relative change in velocity between the fictitious DOFs associated with the i^{th} device
U'_e	From the eigenvalue decomposition Eq. (5.51)

Four-axle vehicle analysis

Δ	Change in quantity
Λ	Klingel wavelength, see Eq. (3.36)
a	Semi-lateral spacing between the trailing arm bushes
c_e	Inerter end damping
c_{bx}	Trailing arm bush longitudinal damping
c_{by}	Trailing arm bush lateral damping
k_e	Inerter end stiffness
k_{bx}	Trailing arm bush longitudinal static stiffness
k_{by}	Trailing arm bush lateral static stiffness
k_{cx}	Trailing arm bush longitudinal damping end stiffness
k_{cy}	Trailing arm bush lateral damping end stiffness
K_{sx}	Primary spring longitudinal shear stiffness
K_{sy}	Primary spring lateral shear stiffness
L	Lateral distance between the contact points
P	The pitch DOF
r_0	Nominal wheel radius
T	The roll DOF
W	The yaw DOF
W_L	The static axle-load
X	The longitudinal DOF (direction of travel)
Y	The lateral DOF (perpendicular to the direction of travel in the horizontal plane)
Y_A	The lateral force transmitted per axle box

Z	The vertical DOF (positive downwards)

Abbreviations

CAD	Computer Aided Design
DOF	Degree(s) of Freedom
FSS	Frequency Selected Stiffness
GN1	Generic Network 1
GN2	Generic Network 2
HALL	Hydraulic Radial Arm (from the German *Hydraulisches Achslenkerlager*)
IRW	Independently Rotating Wheelsets
kph	kilometres per hour
LHP	Left-Hand-Plane
mph	Miles per hour
MTBF	Mean Time Before Failure
PSD	Power Spectral Density
PYS	Primary Yaw Stiffness
RCF	Rolling Contact Fatigue
RMS	Root Mean Square
rrd	rolling radius difference
SVD	Single Value Decomposition
TAC	Track Access Charge
TID	Tuned Inerter Damper
TMD	Tuned Mass Damper
VTISM	Vehicle-Track Interaction Strategic Model
VUC	Vehicle Usage Charge
WLRM	Whole Life Rail Model
wrt.	with respect to

Chapter 1

Introduction

From the introduction of flanged wheels, and the coning of the wheel-tread in the early 19^{th} century, to the developments in active suspension control using tilting mechanisms and magnetic levitation in recent decades, the railway industry has undergone substantial changes in its 250 year history. Initially, fundamental problems concerning guidance, the kinematic oscillation, and material strength presented major engineering challenges. However, towards the latter part of the 20th century, as vehicle speeds increased, and experimental, analytical and numerical modelling capabilities rapidly expanded, the focus slowly shifted towards other aspects, such as preventing instabilities and improving the environmental impacts of vehicles by decreasing maintenance costs, and nationwide electrification.

With such a variety of performance criteria to optimise railway vehicles for, numerous trade-offs exist when it comes to their suspension design. One of the most troublesome of these trade-offs concerns curving and straight running performance. When a railway vehicle is subject to curving conditions (which include a curving radius and track cant angle), the rolling radius difference (rrd) between the left and right wheels on each wheelset results in creep forces occurring at the wheel-rail contact patch. These forces, which increase when the curving radius tightens, are usually presented as an energy loss in the form of the parameter T_γ, and increase the propensity for the track and wheel material to wear and succumb to Rolling Contact Fatigue (RCF). Under straight running conditions, the main inputs affecting dynamic vehicle behaviour are the undesirable irregularities in the tracks' dimensions (i.e. lateral, vertical and gauge variations). In general, the passenger comfort and stability are usually assessed purely under straight running conditions, as the tracks' transition period under curving is rarely the highest contributing factor to passenger comfort.

The vehicle's Primary Yaw Stiffness (PYS), the sum of the stiffnesses in the longitudinal direction (direction of travel) between a wheelset and its corresponding bogie, plays a significant role in determining the vehicle's curving and straight running performance. In general, a higher PYS decreases a wheelset's propensity to yaw, thus

allowing the wheelsets to position themselves more radially (becoming less parallel with one another). This increases the wheelset's steady state lateral displacement in a curve, and in turn increases wheel-rail forces at the contact patch, degrading trackwear. However it also improves passenger comfort due to the less rigid overall connection between the carbody and wheelset.

Research into active and semi-active control and steering systems, including the use of tilting carriages and Independently Rotating Wheelsets (IRWs), has proven fruitful in terms of balancing the stability and desire for passenger comfort improvements. These systems, however, have high actuator power requirements, are susceptible to measurement error, and have high fault tolerances, making them more expensive than purely passive suspensions, with higher risks and power usage. An attractive alternative to these costly active systems is to pursue an intelligent and systematic approach to passive vibration suppression. The HALL-bush, a device with both a static and dynamic stiffness, is already in use in the primary longitudinal suspension of a number of vehicles, and addresses, to a limited extent, the performance trade-off described above. A relatively new mechanical device, named the inerter, has the potential to improve passive railway vehicle vibration suppression capabilities yet further.

First conceived and formally developed in 2002, both academically and experimentally, and then used *in-secret* in Formula One until 2008, the inerter is a two-terminal passive mechanical element which resists acceleration, much like a damper resists velocity, and a spring displacement. The reaction force produced is proportional to the relative acceleration between the terminals, with the proportionality constant named inertance, measured in kg. Manifesting in many designs (rack and pinion, ball-screw, fluid passageway, mechatronic inerters for example), an inerter's inertance need not extensively correlate with its mass, due to system gearing; this *up-scaling* makes inerters attractive and applicable to a wide variety of dynamic systems. The main benefit that inerters bring to the field of vibration suppression is that they complete the electrical-mechanical, force-current analogy (being analogous to a two-terminal capacitor) thus allowing any passive mechanical impedance to be synthesised, and widening the capabilities for vibration control.

Inertia-like mechanisms have been around for centuries in the form of mechanical-flywheels, flowing fluid and acceleration resistance in general, however the concept has only been studied from a mathematical and circuit-theory point of view for the past two decades. Modern inerter-type devices are steadily making their way into many engineering systems and their identified applications are wide ranging. From their initial use in Formula One and then general automotive systems, to their anticipated adoption by the civil industry in the form of Tuned-Inerter-Damper (TID) structures, a wide range of industries can see their potential. A vast amount of research and testing is needed though for such a step change to be warranted and implemented,

especially in the railway industry, where such large, heavy and expensive vehicles exist and such a complicated set of system interactions occur.

Within the railway vehicle dynamics literature, inerters have already proven to be valuable assets to suspension design. It has been shown that vehicles' critical speeds can be increased with the adoption of parallel inerter layouts in a range of suspension locations, and that significant passenger comfort improvements can be obtained by the use of inerters in both the lateral and vertical suspension. Research also suggests that actuator force requirements can be reduced in semi-active skyhook-damping based systems with the inclusion of mechatronic inerters, and, in a separate study, that contact patch forces can be reduced whilst levels of passenger comfort are maintained (quantified by the system's least damping ratio). Broadly speaking, however, these sets of analyses have been performed on simplified models, with simplified system inputs. There is a need, in this line of research, for more realistic models to be studied, with more realistic inputs (such as track irregularities), and a wider range of cost functions (such as both curving and straight running performances, and other vehicle assessment criteria).

To this end, this thesis will explore the extent to which optimised inerter-based suspensions, which are incorporated into the primary bush, can improve the performance of railway vehicles from a trackwear, passenger comfort and stability perspective. Employing numerical simulation and optimisation techniques in MATLAB® and the commercial railway vehicle modelling software VAMPIRE®, a variety of beneficial spring-inerter-damper suspension configurations will be explored initially for a simple two-axle vehicle, and then for a more complex four-axle vehicle. These configurations, which can be thought of as variants of the traditional trailing arm bush layout, are shown to respectively permit the concurrent improvement of both curving and straight-running performance in the simplified model, and more significant trackwear improvements in the more realistic model, whilst passenger comfort levels are maintained.

Chapter 2

Literature review

Although widely considered to be a Victorian invention, the dynamic analysis of railway vehicles and their interaction with the track and the surrounding environment is extremely complex, and a variety different methods are used to assess the vehicles' performance and behaviour, and model the system dynamics. A relatively new, passive mechanical device, named the inerter, has the potential to benefit railway suspensions to a great extent. However, the size and complexity of both the overall railway industry infrastructure, and railway vehicles themselves, means that significant financial and passenger experience improvements need to be proven possible with inerters, both theoretically and experimentally, before their adoption by companies.

This section begins by discussing important challenges in railway dynamics, most notably the trade-off between straight running and curving performance. Passive and active railway vehicle suspensions are then reviewed before the inerter is introduced as an attractive addition to springs and dampers in mechanical suspension networks, significantly increasing vibration suppression capabilities. Applications of the inerter to date in both academic literature and industry are assessed, and then, more generally, the three main passive vibration approaches are reviewed and critiqued. Research concerning how the inerter can be implemented in railway vehicles specifically is then reviewed, with relative merits stated. Finally, the overall motivation for this thesis is laid out, the main aims are laid out, and the contents of each chapter is outlined.

2.1 Railway vehicle dynamics trade-off

The trade-off between reducing the lateral acceleration of the vehicle body (referred to as the carbody in this thesis) whilst on a straight track and reducing the magnitude of the wheel-rail creep forces under curving conditions has long been problematic. When a railway vehicle travels around a curve, a decreased static longitudinal stiffness, and therefore a decreased Primary Yaw Stiffness (PYS), results in a reduction in the energy lost due to friction at the contact patch, quantified by the commonly used

parameter T_γ [1]. T_γ can also be defined as the wheel-rail tangential force multiplied by wheel-rail tangential creepage, or the energy lost at the contact patch. Reducing T_γ leads, for moderate values of T_γ, to a reduction in Rolling Contact Fatigue (RCF), which in turn reduces the maintenance costs related to the tracks and wheels, and the overall Network Rail Variable Usage Charge (VUC) [2]. See Section 2.2.1 for a more detailed explanation on how both the *RCF* and *wear* components of general trackwear vary with T_γ. The VUC includes a calculation of the marginal cost of rail surface damage caused by rail vehicles based on the T_γ for a variety of curving radii. A decrease in PYS, however, can lead to a loss of stability and an increase in the lateral acceleration of the vehicle body during straight running conditions, causing a deterioration in passenger comfort as the wheelset and the carbody move increasingly independently from one another. A loss of stability is also problematic from a safety perspective, as this would make the vehicle more susceptible to derailment and increase the risk of it being blown over in gales. The concepts of T_γ and VUC are discussed more detail in Sections 3.2.2 and 6.3.2 respectively.

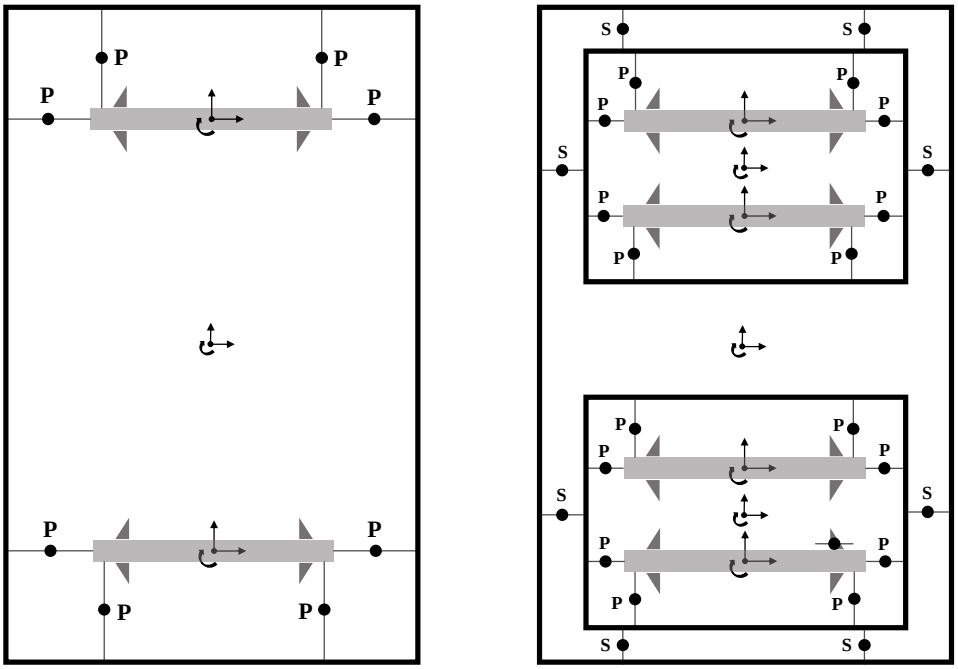

(a) A simple schematic of a two-axle railway vehicle.

(b) A simple schematic of a four-axle railway vehicle.

Fig. 2.1 Simplified generic plan views of two-axle and four-axle railway vehicles, showing the carbody, wheelsets and bogies. P represents the approximate locations of primary suspension elements, and S represents the locations of secondary suspension elements. More accurate diagrams can be seen in Figs. 3.2 and 3.6.

2.2 Railway vehicle suspension development

2.2.1 Passive railway vehicle suspension designs

Considering a typical bogied passenger vehicle, with four-axles (see Fig. 2.1(b)), the primary suspension connects the wheelsets to the bogies, and the secondary suspension connects the bogies to the carbody. Freight vehicles are often single-stage, or two-axle (see Fig. 2.1(a)), as they do not have to adhere to as strict passenger comfort standards; however around half of the current freight rolling stock are multi-stage. The terms primary bush and trailing arm bush are used interchangeably, and refer to the rubber bushing structure which connects the wheelset to the bogie. The default lateral component of this comprises a static spring in series with a damper which exhibits a certain compliance. The PYS comprises primary suspension stiffness components, more specifically, the longitudinal stiffness of the trailing arm bush and the longitudinal component of the shear stiffness, which acts in all six DOF (Degree(s) of Freedom). The work of [3] provides an overview of railway vehicle suspension development.

Examples of literature detailing the continued development of passive railway vehicle suspensions are detailed as follows. The analysis of [4] focuses on a secondary vertical suspension component which comprises both a rubber element, and a coil spring; named together as a *mix*. Modelling both nonlinear elastic components, as well as viscous and friction aspects, the study concludes that high hysteresis rates occur in the spring's force-displacement characteristic. These rates are exacerbated further by an increased displacement input and excitation frequency, which in turn leads to stiffness dominating viscous damping aspects. For ride comfort evaluation and prediction purposes, a finite element vehicle model was proposed and developed in [5], with the frequency domain results correlating well with standard ride comfort predictions based on measurements. The standards by which bogie yaw resistance (measured using the *X-factor* method) is quantified were put into question when an analysis of a multi-stage vehicle, including flexi-coil springs with tilting spring pads [6], concluded that the bogie yaw resistance, as well as the quasi-static guiding force, was highly dependent on cant deficiency, hence vehicle curving speed. It is likely, therefore, that the vehicle model used in the latter part of this thesis [7] also exhibits this sensitivity. The research of [8] analyses the vertical vibration of a relatively simplistic triple-bogie railway vehicle model, with the aim of optimising the damping ratio. It is concluded that, when considering pitch *and* bounce carbody accelerations, a compromise in the damping ratio is required for optimum overall performance. An important point is made in this analysis; namely, that carbody accelerations are highly dependent on where on the carbody they are measured, and that they normally increase with increased vehicle forward velocity; however local maxima may be observed due to the filtering effects arising from the wheelsets.

The HALL-bush and the RCF damage function

A recently introduced passive vibration suppression technique which, to a certain extent, alleviates the trade-off described in Chapter 1 and Section 2.1 is the use of the HALL-bush structure in the longitudinal suspension (see Fig. 2.2). Discussed in detail in [9, 10], and developed by Freudenberg Schwab, the HALL-bush (derived from the German Hydraulisches Achslenkerlager, which translates as *Hydraulic Radial Arm*), is a bushing device with cavities in the rubber which contain hydraulic fluid. These provide internal damping in the longitudinal direction, resulting in a high (dynamic) stiffness at higher frequencies (straight track disturbances), and a low (static) stiffness at lower frequencies (curving). In the work of [10] it is refereed to as a Frequency Selected Stiffness (FSS) device. An inerter (introduced in Section 2.3 and used widely throughout this thesis) of the fluid variety differs to a HALL-bush by using helical tubing to create an inertial effect.

The HALL-bush has been shown to enable a reduction in PYS, thus reducing trackwear, and maintaining a satisfactory level of passenger comfort [9, 10]. It has already been implemented in some vehicles to date, and could also allow for a lower wheel conicity profile to be used, without excessive flangewear becoming an issue. However it is also suggested in [9] that, for certain tight radius curves, the damage caused by Rolling Contact Fatigue (RCF) could increase with the use of the HALL-bush. It is suggested in [9, 10] that difference in the static and dynamic effective stiffnesses within a HALL-bush can be around an order of magnitude, however further work on how the ride comfort and vehicle stability is affected is necessary to establish this.

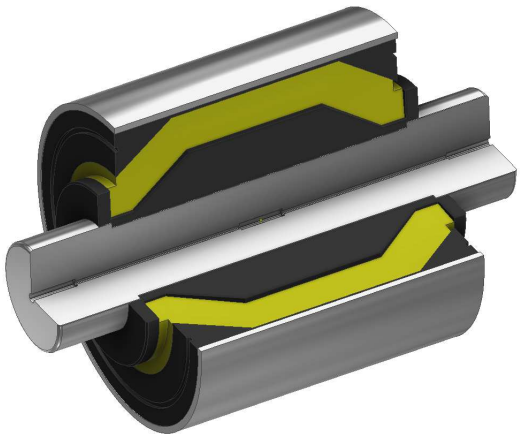

Fig. 2.2 A CAD drawing of the longitudinal suspension HALL-bush device, with the fluid passageways visible in yellow, inspired by the design seen in [9].

As alluded to earlier in this section, the RCF (crack growth) and wear (wearing away of material) at the contact patch interact in a non-trivial manner. Figure 2.3 details the Whole Life Rail Model (WLRM) [11–13] which combines the interactions of the two phenomena into a *damage function*.

The differing rates of increase of RCF and wear (Fig. 2.3(a)) lead to Fig. 2.3(b) where the two effectively compete. Point A is the fatigue threshold, at region A-B only RCF occurs, at region B-C wear increases at a faster rate and cracks are partially worn away, and from point C onwards there is sufficient wear to completely remove all cracks. Later on in this thesis, to simplify the analysis, the term *trackwear* is used as a general measure of a combination of wear and RCF, and the energy loss T_γ is used to quantify it. It should be noted therefore that any device placed in the primary suspension allowing the PYS to be reduced may reduce T_γ in the B-C region, hence causing an effective increase in RCF, but a decrease in wear).

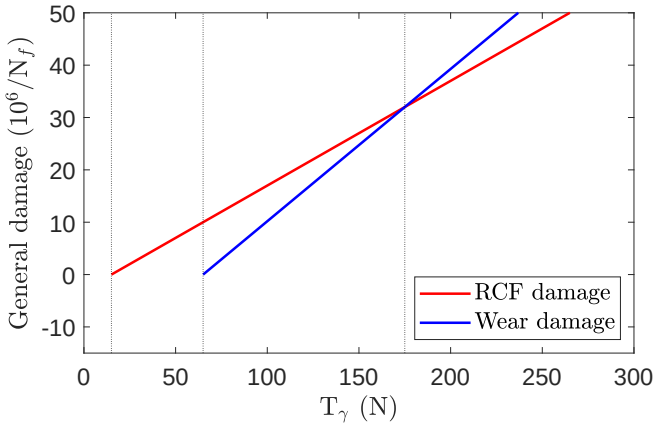

(a) The rate of increase of RCF and wear damage, both defined as positive for clarity.

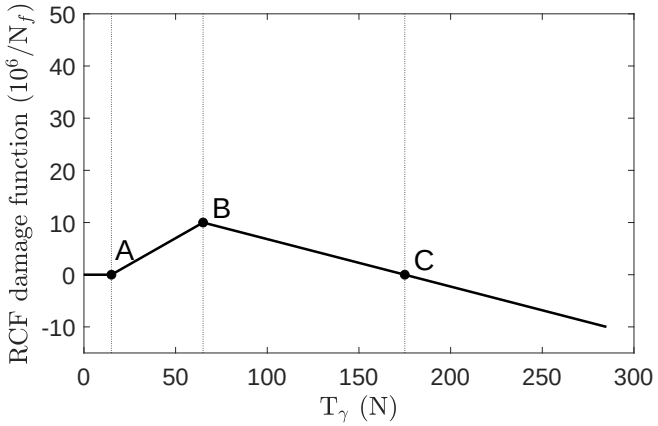

(b) The overall RCF damage function, showing how RCF and wear interact.

Fig. 2.3 The two important plots representing the Whole Life Rail Model (WLRM), I.E. how RCF and wear interact to form an overall *damage index*. Point A is the fatigue threshold, between A and B only RCF is present, between B and C the wear rate is higher than the crack propagation rate hence the overall damage index decreases to zero at C, and above C wear dominates and RCF is not an issue.

2.2.2 Active railway vehicle suspension control

Active railway vehicle control methods have been successfully established, addressing both straight running and curving performance, and other performance criteria. Whilst improved vibration suppression can be achieved using active rather than passive suspension components, risks such as measurement error and actuator malfunction, as well as problems associated with high power requirements and low fault tolerances have prevented the wide-spread application of these solutions.

The articles of [14] and [15], written at the turn of the millennium, detail how the field of railway dynamics was progressing towards a control engineering rather than a mechanical engineering domain, as it had been or centuries previously. It showed how the tilting of carriages can benefit both passenger comfort, and curving performance, if implemented correctly. It also highlighted the point, however, that if tilting mechanisms over-used, or used *too perfectly* (i.e. if effectively passengers do not perceive any centripetal acceleration, or cant deficiency, whilst curving) the process backfires, and the passengers become more susceptible to motion sickness.

A control system for a two-axle railway vehicle with Independently Rotating Wheelsets (IRW) is presented in [16] and [17] , with inputs being that of yaw torque and the feedback element being the relative rotation speed of the wheels on the same axle. Active control systems that use feedback mechanisms such as angle of attack or wheel-rail deflection, are deemed too impractical and expensive. The simplistic control scheme brings down wheelset displacements under curving conditions, eliminates flange contact, even on low speed curves, and improves the passenger comfort. A relatively higher overshoot in wheelset lateral displacement is observed but the steady state displacement is almost 80% lower than that observed in the default. This would result in a significant reduction of surface wear.

The work of, [18], undertaken by the same authors as the previous two pieces of literature, develops an robust H_∞ control technique on a two-axle IRW vehicle designed to provide enhanced *curve following* performance as well as improve the ride quality. Natural, average variations in vehicle parameter values have been taken into account, along with *worst-case* creep and conicity combinations, and, although again lateral wheelset displacement overshoots have significantly increased, the steady state values have decreased by roughly 50%. A reduction of this magnitude would significantly reduce the longitudinal creepage, and hence T_γ. Furthermore, it is argued that although the torque demand would be very high, the average power would be low due to the actuator velocity.

The use of lateral pneumatic actuators connected to the vertical secondary suspension, with the aim of providing a centring system is analysed in [19]. Lateral carbody overshoots and settling times were found to be significantly reduced with the

use of this technology, and the lateral displacement of the carbody at the level of the secondary suspension also decreased. Another H_∞ control system is considered in [20], in the case of tilting mechanisms in a high-speed railway vehicle, whilst a skyhook damping strategy is employed in the lateral secondary suspension. The resulting tilt actuator, lateral actuator, and anti-roll bar enable the vehicle to meet all necessary performance requirements, most notably that sufficient ride quality can be guaranteed under straight running conditions, and in curved transitions, the lateral carbody acceleration overshoots are significantly reduced. Finally, active steering measurement systems are studied and developed in the work of [21]. From a control standpoint, the study explores and identifies a number of sensing opportunities, develops fault detection and isolation schemes, and explores cant deficiency estimation methods. It should be noted that the method by which *random* track irregularities are simulated in this thesis is inspired by the track input method developed in [21].

2.3 Inerter-based passive vibration suppression

2.3.1 The inerter

The inerter is in the process of revolutionising the discipline of passive, and to an extent active vibration suppression by vastly expanding the range of realisable suspension structures. After being officially introduced at the beginning of the millennium, and used in Formula One under the pseudonym J-damper, it currently has many industrial applications. This section details the general concept behind the inerter and explores the different types of inerter.

General concept

The electrical-mechanical force-current analogy, first introduced by Firestone [22], has long been known to be incomplete, as, whilst an inductor and resistor can be respectively mapped to a spring and damper using this analogy, a capacitor cannot be fully mapped to a mass; this is because one terminal of the mass is effectively grounded for it to be allowed to be accelerated due to Newton's Second Law, whereas a capacitor can be connected across two voltage lines. The inerter, a two-terminal passive mechanical device proposed by Smith in 2002 [23], completes this analogy by exhibiting the property that the reaction force it produces is directly proportional to the relative acceleration between its terminals. The aforementioned electrical-mechanical analogy also states that velocity difference is analogous to voltage, and therefore the mechanical inerter is analogous to the electrical capacitor using circuit theory; the ideal property of a capacitor is that the current flowing through it is proportional to the derivative of the voltage across it, and the ideal property of the inerter is that the forced exerted by it is proportional to the derivative of the velocity difference across its terminals.

The fundamental equation which captures the inerter's dynamics can be written as

$$F = b(\dot{v}_1 - \dot{v}_2), \tag{2.1}$$

where b is the device's inertance, measured in kg, $\dot{v}_1$ and $\dot{v}_2$ are the accelerations of each terminal, and F is the reaction force produced by the device. The benefits of the inerter's introduction to the field of both electro-mechanical circuit theory and vibration suppression are demonstrated in Smith's breakthrough study [23], and summarised below

- With the introduction of the inerter, any one-port positive-real impedance can be passively synthesised using classical electrical network synthesis theory. This widely increases the scope for vibration suppression as a far wider range of passive mechanical structures can be produced. Hence, mechanical networks combining inerters, springs and dampers can theoretically describe any positive-real transfer function [24].
- The inertance of a device need not correlate with its mass, or more specifically, the mass of the element of the device which is responsible for producing the inertance effect, such as the flywheels or moving fluid. This means that very high inertances, which are required for large dynamic systems such as in railway vehicles or buildings, can be produced, by the use of gearing in ball-screw inerters and differences in orifice size in fluid inerters for example.
- Unlike how a mass is introduced to a system, such as a Tuned Mass Damper (TMD), an inerter does not require a *virtual ground* to achieve the electro-mechanical force-current analogy.

Types of inerter

The first types of inerter to be introduced were based on flywheels, using their inherently significant inertia to provide acceleration resistance effects. These, shown respectively in Fig. 2.4 can take the form of a rack and pinion, [23, 25], and ball-screw.

Rack and pinion inerters, more so than ball-screw inerters (see Fig. 2.5), are prone to suffer detrimental effects due to friction and backlash within the gears, producing potentially unquantifiable system nonlinearities [25, 26]. These detrimental effects manifest themselves respectively as excessive gear mechanism wear, which inevitably reduces the device's Mean Time Before Failure (MTBF), and induced phase lag, which makes modelling of the realistic overall system more problematic. Ball screw inerters, where the inertance is determined by the pitch of the screw thread and the inertia of the flywheel are less prone to these effects, and it is shown in [27] that a device of 2 kg

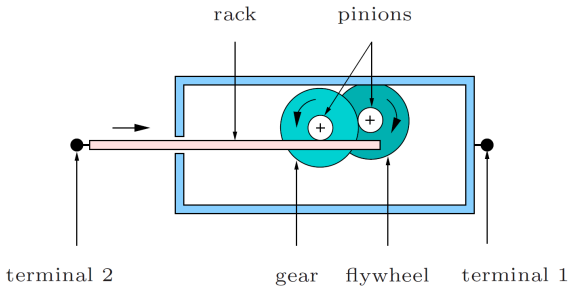

(a) Rack and pinion inerter.

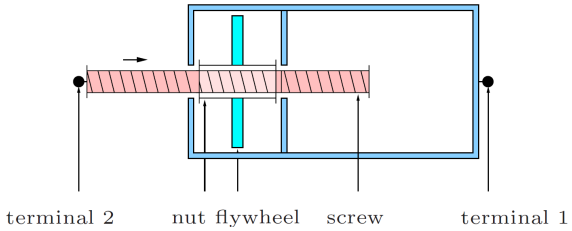

(b) Ball-screw inerter.

Fig. 2.4 Schematics depicting the two most common flywheel variants of the inerter device; reproduced from [25].

in mass, but with an inertance of 75 kg is commercially available (2017). The work of [28], which assesses the impact of ball-screw inerter nonlinearities on suspension design, nevertheless shows that backlash, friction, and elastic effects still occur. However, backlash can be significantly reduced, or potentially eliminated using one of the four methods describe in [29] during the manufacturing process.

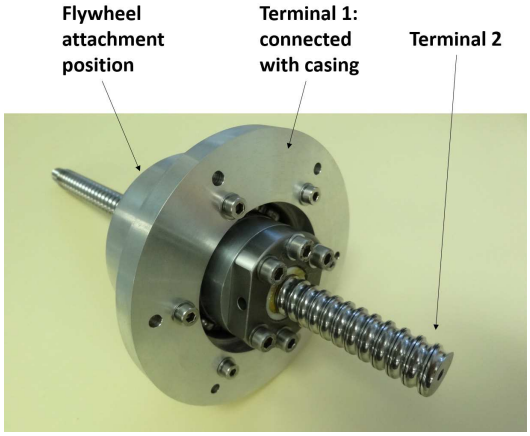

Fig. 2.5 A ball-screw inerter, built at the University of Bristol, with its outer casing removed to enable adequate visibility of the threaded rod.

It is clear from the above assessment that both ball-screw and rack and pinion inerters inherently struggle to function exactly as modelled, especially after experiencing significant amounts of cyclic wear. The presence of moving parts also causes maintenance costs to be very high, and hence the industrial applications of flywheel

based inerters are limited [30]. To this end, fluid based inerter devices have become more and more popular and attractive in recent years. They have the advantage of possessing a very limited number of moving parts, heavily reducing material wear and hence increasing the MTBF.

The work of [31] proposes the first style of fluid inerter, which makes use of a hydraulic motor. It takes the form of a piston cylinder, where one terminal of the inerter is the cylindrical body and the other the piston, and makes use of the pressure difference either side of the piston when the terminals are subject to an equal and opposite force. This pressure difference drives the hydraulic motor, providing inertance to the device. Experimental testing in [31] concluded that the device performed well and to a good degree of accuracy when compared with the theoretical model. Another effective type of fluid inerter, proposed in [32], makes use of fluid flowing in a helical channel, and the difference in its cross sectional area and the cross-sectional area of the main cylinder to provide the inertance. A schematic is shown in Fig. 2.6.

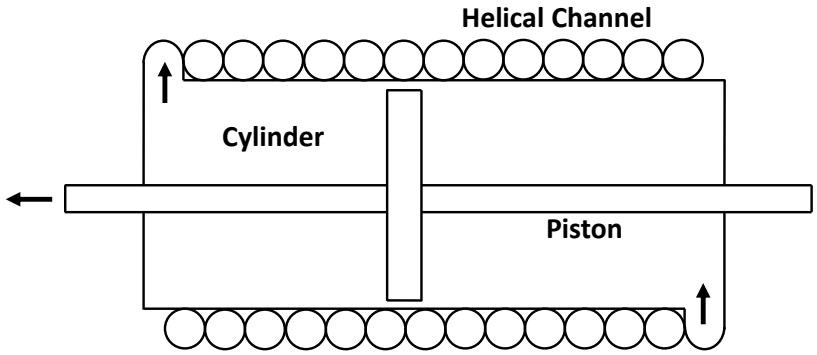

Fig. 2.6 A fluid inerter, made up of a piston, cylinder, and helical channel; reproduced from [32].

It is derived in [32] that the inertance is independent of the velocity of the fluid flowing through the channel, and is written as

$$b = m\frac{{A_1}^2}{{A_2}^2}, \tag{2.2}$$

where m is the mass of the fluid in the helical tubing, A_1 is the cross sectional area of the main cylinder, and A_2 is the cross-sectional area of the helical-tubing. It should be noted that A_2 has a large impact on m,

$$b = (\rho l A_2)\frac{{A_1}^2}{{A_2}^2} = \rho l\frac{{A_1}^2}{A_2}. \tag{2.3}$$

ρ is the density of the fluid, l the total *un-coiled* length of the helical tubing, and

$$m = \rho l A_2. \tag{2.4}$$

Nevertheless, according to Eq. (2.2), the inertance is proportional to the fourth power of the ratio of the two radii. Hence, it can be envisaged that large inertances can be produced with relatively moderate radial differences. The parasitic damping, which occurs in the above fluid inerter due to the viscous effects in the fluid, is modelled well by a damper in parallel with the inertance, and in exacerbated by a smaller helical tubing diameter.

Research presented in [30] proposes both a lumped parameter hydraulic model and the equivalent mechanical model for a fluid inerter similar to that shown in [32] (see Fig. 2.6). Also, a general theoretical model identification procedure is proposed, using linear velocity testing. The multiple models are validated against the tested prototype and a good agreement was observed.

2.3.2 Passive vibration suppression methodologies

With the introduction of the inerter in Section 2.3.1, it was shown that not only is the electro-mechanical force-current analogy complete, but that the range of passive absorbers that can be realised has expanded, resulting in far greater vibration suppression possibilities. The way in which the parameters of the springs, dampers and inerters are chosen depends on how the specific layout is proposed. It should be noted that *configuration* refers to the topological arrangement of springs, dampers and inerters along with parameter values, *beneficial* or *optimal configuration* refers to a configuration with optimised parameter values, and *layout*, or *network*, refers only to the specific topological arrangement. The design of optimal suspension (or vibration absorber) configurations can be undertaken in three ways: the *structure-based approach*, the *immittance-based approach*, and a recently introduced combination of these, the *structure-immittance approach*, all of which are briefly discussed in this section.

Structure-based approach

The structure-based approach can be thought of as the most simplistic of these three approaches. The topological arrangement of each candidate network is predetermined, and the element values (which are given realistic upper and lower boundary constraints) are optimised for a certain cost function. The decision on the topological arrangement for a given application is normally made based on previous research, or if the simulation time is sufficiently computationally efficient, a large number of layouts can be investigated. Before the introduction of the inerter, only spring, damper and mass elements were available for investigation. A popular layout, the Tuned Mass Damper (TMD), which consists of a mass connected to the host structure by a parallel

spring and damper, established itself as an effective building vibration absorber in tall buildings which are frequently subject to wind and earthquake induced vibration. Fig. 2.7 shows four common inerter-based suspension networks, with symbols k, c, and b denoting stiffness, damping and inertance parameter values respectively. It should be noted that the devices connect different mass terminals within the structure, and for the majority of optimisation cases, there exists a static, parallel stiffness element which has little potential to vary, such as a structural component of building. This will normally affect the dynamics of the overall system considerably.

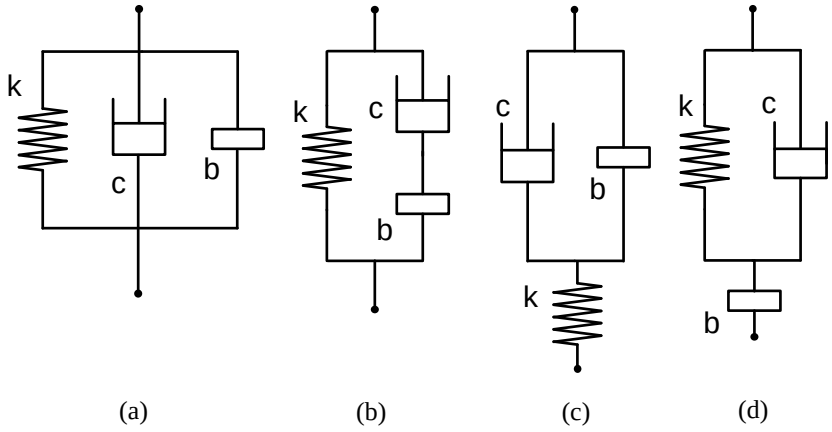

Fig. 2.7 Four common passive vibration absorber layouts.

- Layouts (a) and (b) respectively represent a parallel spring-inerter-damper, and a spring in parallel with a series inerter and damper topology. A leading example of their use in the literature is in the work of [33], where they were shown to give respective earthquake-based vibration reduction improvements of 55% and 58% when applied across the lower floor of a building.
- A Tuned Viscous Mass Damper (TVMD), shown in (c) was developed as a novel seismic control device in the research of [34]. In this analysis, an optimisation procedure which minimised the peak amplitude of the resonance curve was used to successfully reduce vibration. It was found however that for ground motions with long periods of vibration, the performance of the TVMD, compared with the original system, degraded slightly.
- Layout (d) is the only layout shown with a series inerter. Emerging from the TMD concept, this device, named the Tuned Inerter Damper (TID) was studied in [35] and shown to be effective at building vibration control, when the high achievable mass-ratios (between the inertance and the building mass) were exploited.

The main advantage of the structure-based approach is that individual component parameters are varied directly, and parameter constraints can be applied. Parameter

constraints arise for many reasons (e.g. cost, space, and simply attainability). However, the main disadvantage to this method is that many layouts, which have the potential to be beneficial configurations, are not considered.

Immittance-based approach

Fundamentally differing from the structure-based approach to vibration absorber design, the immittance-based approach synthesises optimised positive-real system immittance, or impedance, functions to networks using network-synthesis theory. The Laplace domain immittance of the optimisable suspension structure in question is typically written as

$$L(s) = \frac{\tilde{F}}{\tilde{u}}, \tag{2.5}$$

where F and u denote respectively the force produced by the device, and the relative velocity between the terminals, and $\tilde{F}$ represents the Laplace transform of F for example. The numerator and denominator coefficients of the immittance functions are optimised for system performance, then network synthesis theory, detailed in [36, 37], is used to create *equivalent* beneficial configurations.

The theorem introduced in [38] which states that any positive-real immittance function can be constructed in a network consisting of resistors, inductors, and capacitors can be extended from the electrical domain to the mechanical domain using the force-current analogy introduced in Section 2.3.1. The complexity of the immittance function is predetermined and depends on the order of the numerator and denominator. Functions of reduced complexity, where the numerator and denominators are of first or second order, are exploited for their benefits in terms of weight and space constraints in [39, 40]. Whilst these usually produce simpler configurations, with high computational efficiency, synthesised higher-order immittances have been proven to be more beneficial in terms of general theoretical system performance [41, 42]. Recent research in this topic which investigates bi-quadratic (second-order) absorbers is detailed in [43–45].

The benefits of this method, which manifest in the large number of explorable network layouts, need to be balanced with its drawbacks. The main downside to the immittance-based approach is that a large number of elements are sometimes required to synthesise certain positive real immittances. This is a presents a significant problem from a manufacturing perspective. Also, as alluded to previously, constraints on elements' parameter values are permitted.

Structure-immittance based approach

The structure-immittance technique combines the advantages of the two previous methods, whilst avoiding as much as is feasibly possible their negative aspects. First introduced in [46], the method allows the user to choose the number of each element that occur in the layout, with resulting transfer functions containing information on the network topology *and* element values; thus one can explore many different network topologies in a systematic manner. For example, choosing 1 spring, 1 inerter and 1 damper (1k1b1c), results in 8 possible network topologies. The approach uses a general procedure (based on series-parallel network theory, utilising many springs which can take optimisable values, or ∞ or 0 depending on their location) to form the *structural immittance* of the device. The red sections of Fig. 2.8(b) and (c) respectively show the four networks that can be created (with the 1k1b1c condition) with the damper and inerter in parallel, and then in series.

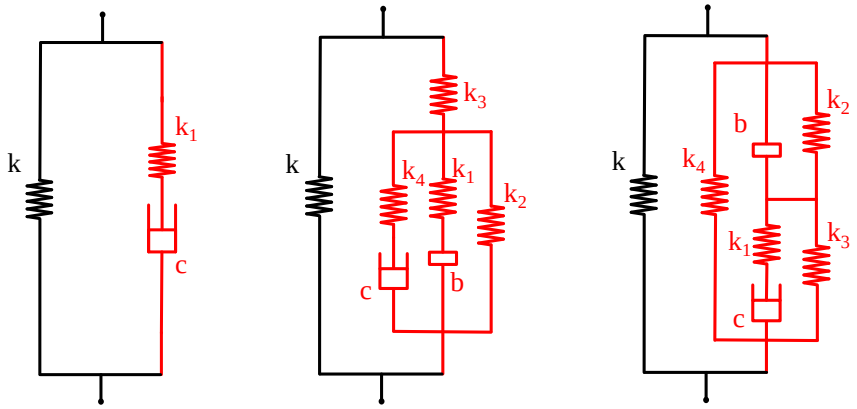

(a) Default network. **(b)** Generic network 1. **(c)** Generic network 2.

Fig. 2.8 The default suspension network, and the two generic networks (in red) which can be used to make up the eight layouts consisting of one inerter, one damper, and one spring. The black spring denotes a static spring, normally a structural element.

The expressions,

$$L(s)_{GN1} = \frac{bc(1/k_1 + 1/k_4)s^3 + bs^2 + cs + k_2}{b(1/k_1 + 1/k_3)s^3 + c(1/k_4 + 1/k_3)s^2 + s}, \tag{2.6}$$

$$L(s)_{GN2} = \frac{bcs^2 + b(k_3 + k_4)s + c(k_2 + k_4)}{bc(1/k_1)s^3 + bs^2 + cs + k_2 + k_3}, \tag{2.7}$$

denote these layouts' respective immittance (or admittance) functions used in the optimisations. The optimisations are set up in a manner such that all 8 available combinations are systematically explored. Note that *admittance* refers specifically to a

device's force to velocity transfer function, whilst *immittance* refers to the concept of admittance and impedance (reciprocals of one another).

The analysis of [46], which is not limited to the mechanical domain, goes on to apply the novel technique to the fields of building vibration suppression and vehicle suspension, finding that the structure-immittance approach can respectively better the structure-based approach and the use of a TMD by over 20%.

2.3.3 Applications of the inerter

Automotive

Although the concept of the inerter from an academic standpoint was public knowledge from 2002 [23], its first application was in fact of a secretive nature. In 2005, McLaren Mercedes introduced the inerter to their Formula One vehicle suspension under the pseudonym *J-damper* [47, 48]. They found that using a parallel spring-damper-inerter configuration could improve grip and handling performance, and other racing teams became perplexed as to how such fast times were being recorded. Kimi Raikkonen's victory at the Spanish Grand Prix is widely attributed to the inerter. In 2007, the true identity of the J-damper was rumbled during the infamous *spy scandal* between Renault and McLaren [49], however the connection between Formula one and the inerter was only made public by the *Autosport* Magazine articles [50] and [51]. The confidentially agreement between the University of Cambridge and McLaren was finally lifted in 2008 as the inerter was becoming commercially available, and the work of [52] defines the inerter as *The missing mechanical element*, whilst also providing a thorough analysis of its function and benefits.

Outside of Formula One, theoretical and experimental academic research work which rapidly developed the inerter's popularity continued in earnest from the early 2000s, initially in the field of automotive engineering. The work of [53], which investigates the use of numerous passive suspension struts, including inerters, in a generalised quarter-car and a full vehicle model, concludes that improvements of around 10% are achievable for measures such as ride, handling, and tyre normal load. Both single and multi-objective optimisation methods were implemented in this analysis, and moreover, the advance in phase, which is expected from inerters, is demonstrated experimentally using a full inerter prototype. This work is further consolidated in [41], where inerter-integrated suspensions in a quarter-car model are optimised by utilising characterisation of positive-real constraint using matrix inequalities. This allows higher order immittances to be optimised over, producing superior dynamic vehicle performance improvements. The work of [54], which develops an analytical global optimisation algorithm, proves that the outcomes of the multi-objective optimisations in [53] are indeed global minima.

Further multi-objective optimisation is performed in the research of [55] which details that suspension deflection is a main limitation for tyre grip and ride comfort performance criteria, when using a variety of inerter-based configurations. A mechatronic strut which includes a ball screw inerter and a permanent electromagnet, hence is analysed by both mechanical and electrical networks, is proposed for vehicle suspension in [40]. It is experimentally validated, with necessary nonlinearity modifications made, and is shown to be an effective vibration suppressor by utilising higher order system immittances. A stricter optimisation procedure (which used international standards of permitted acceleration levels) was used to optimise an inerter-based suspension in [56], and in [57] a series inerter layout in the secondary suspension suspension, resulted in a mild reduction in vehicle body acceleration, and tyre normal load.

The dynamic performance of motorcycles also has the potential to be improved by the inerter. Analysis undertaken in [58, 59] yields potential reductions in vibration amplitude at the two main primary lateral oscillatory modes: wobble and weave. This is a particular important line of research as motorcycles are prone to resonant forcing and wobble and weave modes can occur at a wide range of speeds. Research on the use of active and semi-active systems incorporating inerters is increasing, and results can be found in [60–63].

Aerospace

Not limited to automotive systems, the inerter has also proved to be popular in aerospace research. Problems such as wing flutter and landing gear shimmy can not only prove extremely dangerous, but also significantly compromise the sector financially from a fatigue perspective. It is shown in [64] that gust loads, which manifest as bending moments, in truss-braced wings can be moderately alleviated by use of an optimised TID within the truss structure. This research also suggests that the inclusion of an inerter enables the required damping value to reduce considerably, to a viable level. The impact of inerters on landing gear shimmy vibration was researched in [65], and it was concluded that whilst inerters can reduce settling time and natural frequency, their influence and benefits largely depend on the inertance range and the dimensions of the landing gear device. Insight was gained in [66], which expands on the work of [65], as to how inerters affected the shimmy suppression when applied to different landing gear models. The use of inerters in aircraft using systematic optimisation procedures is heavily researched in [67–70], which not only consider aircraft landing gear shimmy vibration, but also touchdown performance.

Civil

A rich set of literature exists for how the inerter can be applied to building vibration suppression; it is often thought of as an extension to the TMD concept. Initially known

as the Tuned Vibration Absorber (TVA), patented in 1911 as a *device for damping vibrations of bodies* [71], and further consolidated to include a parallel damper for system tuning by Den Hartog in [72], the TMD creates, with the use of a secondary mass connected to the host structure, an anti-resonance at the host structure's natural frequency, drastically reducing vibration amplitudes. TMD analysis can be found in many studies [73–76], and furthermore, the feasibility of nonlinear TVAs are assessed in [77–80].

The field of building vibration suppression has seen a rapid increase in inerter-related research in recent decades. Building on the results previously mentioned in [33], the work of [81] proposes a more complicated and higher order inertance-integrated suspension structure, further improving the building's earthquake performance. Also in this work, it is found that the performance of a prototype ball-screw inerter is far more consistent with theoretical modelling at lower frequencies. It is suggested that this is because of inerter nonlinearities such as backlash and friction; however, this is unlikely to be problematic when considering the low frequencies experienced in building vibration. Inertia like elements named inertial dampers and dynamic masses in [82] and [83] respectively have been proven to improve building vibration control, and the TMVD (previously introduced in [34]) again uses ball screw *inertia-like* properties to provide mass amplification. The TMVD concept was extended further in [84] to include more advantageous modal analysis, further improving the multi-DOF building's modal responses.

The introduction of a series inerter paved the way for the concept of the TID as an alternative to the conventional TMD. The work of [35] introduces the TID concept and builds on the conventional TMD tuning methods proposed by Den Hartog [72]. The analysis concluded not only that the most desirable location for positioning the TID was between the first and ground floors, but that the use of gearing in the inerter devices meant that high inertance vs storey mass ratios can be achieved, improving seismic performance, and relieving the need for very large masses (required for TMDs). A TID positioning between the first and ground floors reduces structural loads, when compared with a TMD placed at the top of the building, and as the structure acts as a damper at high frequencies, it is highly beneficial across a large frequency range. The concept of an electromagnetic TID (E-TID) is introduced in [85]. Obtaining similar performance benefits to the conventional TID, its power requirements are outweighed by the vibrational energy harvested, and hence there is scope for this extra energy to be used for the building's structural health monitoring. The Tuned-Mass-Damper-Inerter (TMDI), which is similar to a TID structure, but includes a mass as well as an inertance element, and nominally is placed in the upper stories of buildings, is studied at length in [86–90].

The incorporation of inerters to civil engineering systems other than buildings has also been researched, but to a lesser extent. In [91, 92], it is shown that a series inerter can reduce wind and wave induced loads in floating offshore wind turbine structures, and the work of [93] demonstrates that a general system's vibration isolation performance can be enhanced with the addition of an inerter in parallel with the rest of the suspension-like, or connecting structure. Cable systems also can benefit from inerters, as shown in [94], where it was shown that, for a finite-element taut cable model, inerter based absorbers provided increased vibration reduction over traditional viscous dampers for over multiple modes. The TID concept was applied to cable vibration suppression in [95], and, again, was shown to be a viable alternative to viscous dampers. The improvements were seen both in terms of the mid-span cable displacement, and the frequency response, when the cable was subject to earthquake loads. Finally, it is suggested in [96] that inerters should be incorporated into hybrid cable networks, as the use of TIDs increases the deformation of stay cable-bridge cross-ties, thus improving vibration dissipation. Mechatronic inerters were deemed to benefit optical tables in [95] where Disturbance Response Decoupling (DRD) techniques were utilised to effectively isolate ground disturbances with inerter-based passive suspensions.

2.3.4 The inerter in railway vehicles

A number of pieces of research to date have studied the application of inerter-based suspensions in railway vehicles, in a variety of different parts of the suspension, and with different performance criteria. This section provides an assessment of these studies.

The work of [97] assesses the extent to which the inerter can increase a vehicle's critical speed; which is defined as the maximum forward velocity such that all eigenvalues of the system matrix remain in the left-hand-plane. Placed first in the lateral suspension of a 12 DOF vehicle, either in parallel (S2) or in series (S3) with the lateral damper, it was found that including an inerter in fact made little difference to, or decreased the critical speed in the vast majority of cases (varying PYS and lateral damping). These suspect results could be due to the fact that the carbody was fixed during the analysis. Wang *et al.* go on to analyse a more realistic 16 DOF vehicle modelled in AutoSim^{TM}, and conclude that it is possible to increase the critical speed by multiple placements of a parallel inerter layout at a variety of suspension locations, with stiffness and damping parameters tuned. However, it should be noted that the potential critical speeds quoted are far faster than the fastest speed a train could hope to achieve, very high damping rates are required, and that no other system performances (carbody acceleration, passenger comfort, settling-time, curving performance and other legal requirements) are assessed.

It is shown in [42] that two simple inerter-based structures (identical to Figures 2.7(a) and (b)) can bring benefits to passenger comfort, but not dynamic wheel load. The same research also utilises the immittance-based method of suspension optimisation to synthesise higher order absorber immittances, thus achieving better performance. An assessment of inerter nonlinearities, including backlash, concludes that in reality a slightly poorer performance would occur, however inerters would still significantly benefit the system overall.

In [98], a parallel inerter layout in the vertical suspension of a 28 DOF Autosim railway vehicle model was identified to be beneficial to the vehicle's critical speed, settling time and passenger comfort. Further improvements were identified when simulations with a mechatronic inerter were performed, and the mechatronic network's properties were verified experimentally.

Another piece of research which uses inerters in conjunction with active mechatronic vibration control strategies [99] demonstrates that combining vertical inerter-based suspensions with a skyhook damping strategy, in a two-axle railway vehicle, results in an active force requirement reduction of 50% when an improvement in vertical passenger quality of 30% is stipulated.

The work of [100], which concerns the dynamics of a two-axle railway vehicle, aims to improve its vertical ride quality through optimised inerter based suspension implementation, without *over-increasing* suspension deflection when the vehicle for example encounters a track gradient. Random track input data is used, using filtered white noise, as well as a 2% gradient and acceleration limit, and it is concluded that the beneficial inertance-based suspension structure is depended on where on the carbody the vertical acceleration is measured. When using an inerter in parallel (alone) with a series damper and spring, the benefits are of a medium amount, at all carbody locations. However, when using an inerter, spring and damper all in series, the benefits manifest mainly at the leading and trailing position of the carbody. It is found that with the most beneficial configuration, the vertical displacement of the front of the carbody increases slightly from the default case, however the deflection is still well within legal limits.

The analysis of a two-axle railway vehicle in [101] investigates only curving performance, using the yaw stiffness as the cost function for the lateral suspension optimisations, whilst ensuring the least damping ratio and ride quality remain at least as good as for the default layout. It concludes that it is possible to allow the yaw stiffness to be reduced by 33% and 45% for lateral suspensions which contain respectively a single parallel inerter, and a parallel and series inerter. This would result in a reduction of forces at the contact patch forces, with inerter-based lateral suspension configurations keeping the ride quality as good as the default value.

A two-axle, single bogie, 7 DOF railway vehicle is considered in [102], and lateral and vertical ride quality is assessed using stochastic track inputs. It was concluded that passenger comfort improvements can be obtained by implementing the series damper-inerter structure into both the secondary and primary lateral suspensions.

The research presented in [103] concerns a two-axle railway vehicle model, and a thorough analysis is undertaken of the benefits which a variety of optimised inerter-based structures can achieve in the lateral and vertical suspensions. A horizontal plane model is first studied, and it is concluded that structures with single parallel ineters perform are more superior at reducing lateral RMS carbody acceleration than series inerter structures. Inerter end stiffness and damping effects are then taken into consideration, and although the improvements decrease slightly, the overall trends still exist. The vertical dynamics are found to be improved with inerter based layouts, however to a lesser extent.

Finally, a detailed review and summary of the benefits that the inerter can bring to both bogied and two-axle railway vehicles in terms of stability, passenger comfort and trackwear can be found in [104]. This section has shown that the inerter has great potential to improve railway vehicle performance, but the pieces of literature analysed also highlight how complicated railway vehicle dynamics situations can be, in terms of the number of performance criteria available (trade-offs) and enormous scope for extra modelling. Further research is required in the discipline of inerter-based multi-objective optimisation, or in general, an awareness of many other vehicle aspects such as testing for legal requirements, and the use of a wider range, and more realistic track input and contact conditions.

2.4 Research motivations

In Section 2.1, the classic trade-off between curving and straight running performance in railway vehicles was introduced. One of the underlying problems when designing vehicle suspensions is determining a PYS appropriate for enabling adequate vehicle stability without overly increasing contact patch forces. It was observed in Section 2.2 that although active railway vehicle suspension systems are inherently more superior than passive systems at both vibration suppression and stability improvement, the large amount of power which is required for the various actuators makes them expensive to run. Furthermore, risks such as actuator malfunction, measurement error and the low fault tolerances required make their wide spread application problematic. There will always exist a trade-off between high-cost (higher risk) active methods producing excellent performance, and lower cost (lower risk) passive methods producing poorer, or satisfactory, performance. However, it is anticipated that the inerter can bring great benefits to railway vehicle suspensions in a passive manner, and a large part of

this thesis is dedicated to determining the extent of these benefits. One of the major themes in this study is therefore to investigate how much more of an improvement the addition of inerters to vehicle suspensions can bring over the HALL-bush set-up. It is imperative that a significant improvement is obtained in this regard due to the huge infrastructure changes and financial considerations that will be required when the inerter is disseminated industrially.

The inerter was introduced as an extremely beneficial suspension element in Section 2.3.1, and the benefits demonstrated in a variety of engineering disciplines. Widening the scope for passive vibration suppression by allowing any positive-real mechanical impedance function to be synthesised, it is highly anticipated that optimised inertance-integrated suspensions can, just as in the automotive and civil industries, enable more superior system performance when it comes to railway vehicle suspension optimisation. This thesis therefore focuses on suspension networks which include all passive mechanical elements (springs, dampers *and* inerters). The three passive vibration suppression approaches (structure-based, immittance-based, and structure-immittance) are introduced in Section 2.3.2. This thesis makes use of the structure-based approach and, as much as is realistically possible when combining an optimisation tool (MATLAB®) with a piece of industrial software (VAMPIRE®), the structure-immittance approach.

After detailing how much positive research and development has taken place concerning the inerter device in a number of engineering disciplines in Section 2.3.3, the latter portion of this literature review (Section 2.3.4) identified the potential benefits that the inerter can bring to railway vehicles' straight-running and curving performances, concluding that investigations regarding how these two sets of criteria can be bettered at the same time are limited. Furthermore, there are no studies which combine an inerter-based lateral suspension with a HALL-bush longitudinal suspension, and to date, inertance-integrated suspensions have not been investigated in the railway vehicle modelling software, VAMPIRE®. No studies exist which use the PYS (inversely correlating with curving performance) as the cost function. This will form a significant portion of the latter part of this thesis.

Based on the above observations, this thesis has three main objectives:

- To investigate the extent to which inerter-based lateral suspensions can *concurrently* improve passenger comfort and curving performance of a two-axle vehicle.
- To accurately incorporate inerters into the modelling process of an industry standard railway vehicle modelling software, VAMPIRE®, as well as devising a method for determining the optimum parameters within the VAMPIRE® model when the program is inherently built for analysis rather than optimisation.

- To identify and investigate a range of inertance-integrated networks applied to the primary lateral suspension of a realistic four-axle railway vehicle. Optimisations will aim to reduce the PYS as much as realistically possible without sacrificing other performance criteria such as stability, passenger comfort and other performance requirements.

2.5 Thesis outline

Chapter 3 - Railway vehicle modelling techniques including the inerter

The first technical chapter of this thesis introduces the vehicle modelling and analysis techniques which will be employed throughout, as well as demonstrating how the inerter can be modelled in VAMPIRE®, with suitable numerical validation, and assessment of end-stiffness effects. Concepts such as equivalent conicity, as a measurement of the *overall* conicity of a particular track and wheel with nonlinear profiles, T_γ, as a measurement of the energy lost at the contact patch, and RMS carbody acceleration, quantifying the vehicle's passenger comfort, will be introduced. A two-axle railway vehicle modelled in MATLAB®, and a four axle vehicle modelled in VAMPIRE® are introduced, and the means by which straight running and curving performance measures are quantified for the former.

Chapter 4 - Two-axle model passenger comfort and trackwear enhancement

Having established the main vehicle modelling techniques in Chapter 3, Chapter 4 demonstrates the potential of using passive, inerter-based lateral suspensions to concurrently improve passenger comfort and reduce trackwear. A comparison is made, in terms of the Power Spectral Density (PSD) between different types of track input (real tracks with irregularities depending on the rated speed, and filtered white noise), and it is concluded that real track data is most suitable, and therefore will be used for the rest of the analysis in this thesis. An optimisation procedure which combines patternsearch and fminsearch (for fine tuning of parameters) and allows interchangeable Laplace domain suspension immmittance functions to be optimised over for reduced lateral carbody acceleration, is established. The results of which conclude that, with the default PYS, compared with the default spring-damper configuration in the primary lateral suspension, employing beneficial inerter-based configurations can improve passenger comfort by up to 43%. If the PYS is reduced such that the trackwear is improved, similar improvements in passenger comfort can still be achieved with lateral inerter-based suspensions; for example, an improvement of 33% can still be achieved with a 50% reduction in PYS. In addition to solely lateral suspension modification,

the extent to which a HALL-bush longitudinal suspension can be of benefit (with and without lateral suspension alterations) is assessed. This chapter concludes that when an inerter-based lateral suspension is used together with a longitudinal HALL-bush, the passenger comfort improvement rises to 40% (with a halved PYS). This relates to a 25% improvement when compared with a non-inerter lateral plus HALL-bush longitudinal set-up.

Chapter 5 - The location matrix method of railway vehicle simulation

Whilst the analysis of Chapter 4 is performed on a two-axle railway vehicle model in MATLAB, the aim of Chapter 5 is to enable the optimisation of a more complex and realistic railway vehicle modelled in VAMPIRE®. The location matrix method of dynamic system simulation, which allows the user to implement and optimise suspension devices at certain locations within large and complex dynamic systems, is derived and validated using a two-mass MATLAB® model. Including a Laplace to state-space time-domain transformation, this method allows can allow immittance-based, structure-based, and structure-immittance based optimisations, avoiding large transfer function matrix inversions, and algebraic loops due to inerters (which become problematic when SIMULINK® is used). The main technique which it utilises is the decomposition of the location matrix (which defines the coupling positions of the suspension device in question) into either real, or fictitious states, which are adjoined before the equations of motion are transformed to the time domain. The extent to which the method can be applied to the four-axle railway vehicle, defined by exported mass, stiffness and damping matrices, is then assessed.

Chapter 6 - Track friendliness improvement of a four-axle model

The final main chapter of this thesis focusses on the analysis of a realistic four-axle railway vehicle model in VAMPIRE®. More specifically, it investigates the extent to which the vehicle's PYS can be reduced without increasing Root Mean Square (RMS) lateral accelerations, by way of the optimisation of inertance-integrated lateral suspension layouts within the primary, or trailing-arm, bush. The vehicle's dynamics are captured over a range of velocities and wheel-rail equivalent conicities, to reliably simulate real-world running conditions, with the inputs being track irregularities (gauge, lateral and vertical) which arise from the standard rough track rated at 160 kph. As VAMPIRE® can solely be used for analysis and simulation, not optimisation, MATLAB® is used to call VAMPIRE® at each optimisation iteration. Based on these systematic optimisations, which make use of network-synthesis theory within VAMPIRE®, several beneficial inertance-integrated configurations are identified. Using linear conicity and linear creep laws (for computational efficiency), it is found that with

such beneficial configurations, the PYS can be reduced by up to 47% compared to a base-case vehicle, without significantly compromising RMS lateral carbody accelerations; and at the rated velocity, the passenger comfort in fact improves. A PYS reduction of this magnitude has the potential to result in a Network Rail Variable Usage Charge (VUC) saving of 26%. Vehicles with these beneficial suspension configurations are subsequently simulated with nonlinear wheel-rail contact data and using the square root creep law, and whilst it appears that using linear contact information overestimates the carbody accelerations, general trends still exist, and significant reductions and consequent VUC benefits are still apparent. Further simulations are carried out to investigate the optimised vehicles' performance in curve transitions and when subject to one-off peak lateral track irregularities, and peak counting assessments are performed.

Chapter 7 - Conclusions and future work

Overall conclusions of this thesis are drawn in Chapter 7, and a discussion is devoted to the future research and testing which is required for the inerter to become an established part of future railway vehicle suspensions.

Chapter 3

Railway vehicle modelling techniques including the inerter

In this chapter we:

- Establish the two-axle MATLAB® railway vehicle model, and the respective simulation methods used for both straight running and curving analysis.
- Derive how the RMS acceleration of the vehicle's carbody is used to assess passenger comfort, using both real track data, and a Random Track input (filtered white noise).
- Introduce and derive T_γ as a measure of trackwear under curving conditions, produce initial plots of how T_γ and wheelset displacement varies with PYS, and present T_γ's dependency on the PYS.
- Establish the modelling techniques used to simulate the VTISM four-axle railway vehicle in VAMPIRE®, and discuss the means by which VAMPIRE® is used as a simulation tool, and how interchangeable suspensions can be implemented.
- Validate the procedure by which the inerter is modelled in VAMPIRE® by comparing with a simple MATLAB® model including inerter end-stiffness.

3.1 Introduction

The first chapter in this thesis details the models and methods that will be employed throughout, as well as presenting preliminary tests on base case vehicle models, pre-optimisation. Important concepts such as equivalent conicity, VAMPIRE modelling, and trackwear and passenger comfort assessment techniques are introduced, as well as a simple case study to validate the process by which the inerter is modelled in VAMPIRE®.

The chapter begins by introducing a 6 DOF MATLAB® two-axle freight vehicle, which allows interchangeable suspension networks in both the longitudinal and lateral directions. When curving performance is assessed, the inputs are radius of curvature, and cant angle, and when passenger comfort (quantified by the RMS lateral carbody acceleration) is assessed, the inputs are either Random Track or real lateral track variations (rated at a certain speed). Initial assessments of curving performance with two values of PYS are performed and the transient accelerations analysed. In the next part of this section, the focus shifts towards the four-axle VAMPIRE VTISM model, now more typical of a passenger vehicle, with a far larger number of DOF, and a much more powerful set of analytical tools available. Schematics of the vehicle are shown and the concept of equivalent conicity is introduced as a way of defining the conicity of a curved, rather than conical, wheel-rail profile. Next, the process by which vehicles are simulated in VAMPIRE® is discussed, introducing all the necessary file types and what they denote. The concept of replacing interchangeable suspension networks with one another is introduced here, crucial for optimisation purposes, and the way in which MATLAB® optimisations can be performed on VAMPIRE® vehicles is briefly introduced. Lastly the inerter's implementation in VAMPIRE® is discussed in detail, and the means by which the flywheel structure is coded is shown. A short case study is undertaken which aims to validate the inerter's implementation in VAMPIRE®, using a simple two-mass MATLAB® model for comparison purposes.

The two-axle MATLAB® model forms the basis of Chapter 4 and the four-axle model in VAMPIRE® is used in the analysis of Chapters 5 and 6.

The models and methods introduced in this chapter formed the basis for the following publications:

- T. D. Lewis, J. Z. Jiang, S. A. Neild, C. Gong, and S. D. Iwnicki. Using an inerter-based suspension to improve both passenger comfort and trackwear in railway vehicles. *Vehicle System Dynamics: International Journal of Vehicle Mechanics and Mobility*, 2019.

- T. D. Lewis, J. Z. Jiang, S. A. Neild, C. Gong, and S. D. Iwnicki. Improving ride comfort and trackwear of two-axle railway vehicles using inerter-based lateral suspension layouts. *Proceedings of the 6th Conference; Noise and Vibration Emerging Methods (NOVEM)*, 2018.

- T. D. Lewis, Y. Li, G. J. Tucker, J. Z. Jiang, Y. Zhao, S. A. Neild, M. C. Smith, R. Goodall, N. Dinmore. Improving the track friendliness of a four-axle railway vehicle using an inertance-integrated lateral primary suspension. *Vehicle System Dynamics: International Journal of Vehicle Mechanics and Mobility*, 2019.

– T. D. Lewis, Y. Li, G. J. Tucker, J. Z. Jiang, S. A. Neild, M. C. Smith, R. Goodall, S. Iwnicki, N. Dinmore. Inertance-integrated primary suspension optimisation on an industrial railway vehicle model. *Proceedings of the 26th IAVSD International Symposium on Dynamics of Vehicles on Roads and Tracks (IAVSD)*, 2019.

The baseline four-axle VAMPIRE® model is a VTISM model (Vehicle-Track Interaction Strategic Model) [7] provided by Dr. Gareth Tucker at the University of Huddersfield, and the inerter's implementation technique in VAMPIRE® builds on the work of [105].

3.2 A MATLAB® two-axle railway vehicle model

A schematic of the two-axle vehicle model which is to be used in the analysis in Chapter 4 can be seen in Fig. 3.2. This 6 DOF model is similar to the model used previously in [101, 103], within which lateral (to the direction of travel) and yaw motion is considered. The vehicle body (carbody) is connected to the two solid-axle wheelsets via suspension layouts $L_{yi}(s)$ in the lateral direction and $L_{xj}(s)$ in the longitudinal (or travel) direction. In the analysis of Chapter 4, these suspension are subject to layout alterations and optimisation, however the default structures are shown here; respectively in Figs. 3.1(a) and (b).

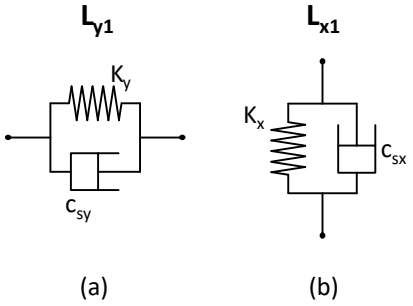

Fig. 3.1 The default $L_{y1}(s)$ lateral (a) and $L_{x1}(s)$ longitudinal (b) suspension layouts, whose locations within the two-axle railway vehicle are visible in Fig. 3.2.

Subscripts x and y here denote the longitudinal and lateral suspension respectively, and subscripts i and j denote respectively the specific lateral and longitudinal suspension layouts. The six states of the system are ordered as follows,

$$x = [y_{w1}, \theta_{w1}, y_{w2}, \theta_{w2}, y_v.\theta_v]^T, \tag{3.1}$$

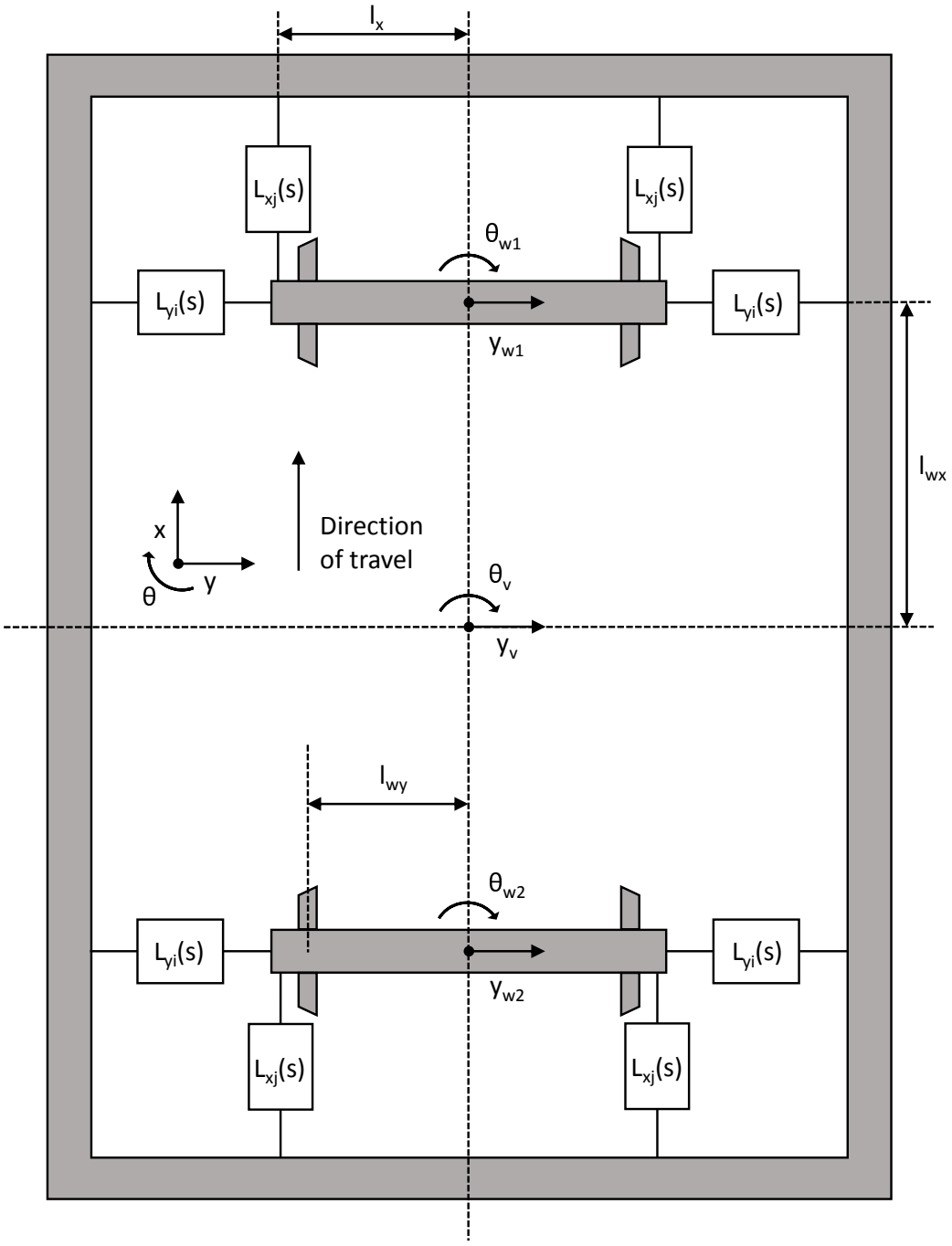

Fig. 3.2 The two-axle, six-DOF railway vehicle model with the four lateral (L_{xi}) and longitudinal (L_{xj}) suspension positions shown, important dimensions used in the equations of motion marked, and all DOF denoted.

The equations of motion governing each state of Eq. (3.1) are as follows:

$$m_w s^2 \tilde{y}_{w1} = 2sL_{yi}(s)(\tilde{y}_v - \tilde{y}_{w1}) - \frac{2f_{22}}{V} s\tilde{y}_{w1} + 2f_{22}\tilde{\theta}_{w1} + 2sL_{yi}(s)l_{wx}\tilde{\theta}_v + \frac{2\varepsilon(N - f_{23})}{l_{wy}r_0}\tilde{y}_{w1} + m_w\left(\frac{V^2}{R_1} - g\theta_{c1}\right), \quad (3.2)$$

$$I_w s^2 \tilde{\theta}_{w1} = \frac{2f_{11}l_{wy}^2}{V} s\tilde{\theta}_{w1} - \frac{2f_{11}\lambda l_{wy}}{r_0}\tilde{y}_{w1} + 2sL_{xj}(s)l_x^2(\tilde{\theta}_v - \tilde{\theta}_{w1}) - \frac{2f_{11}\lambda l_{wy}}{r_0}\tilde{y}_{t1} + \frac{2f_{11}L_{wy}^2 + K_x L_{wx}}{R_1}, \quad (3.3)$$

$$m_w s^2 \tilde{y}_{w2} = 2sL_{yi}(s)(\tilde{y}_v - \tilde{y}_{w2}) - \frac{2f_{22}}{V} s\tilde{y}_{w2} + 2f_{22}\tilde{\theta}_{w2} + 2L_{yi}(s)l_{wx}\tilde{\theta}_v + \frac{2\varepsilon(N - f_{23})}{l_{wy}r_0}\tilde{y}_{w2} + m_w\left(\frac{V^2}{R_2} - g\theta_{c2}\right), \quad (3.4)$$

$$I_w s^2 \tilde{\theta}_{w2} = \frac{2f_{11}l_{wy}^2}{V} s\tilde{\theta}_{w2} - \frac{2f_{11}\lambda l_{wy}}{r_0}\tilde{y}_{w2} + 2sL_{xj}(s)l_x^2(\tilde{\theta}_v - \tilde{\theta}_{w2}) - \frac{2f_{11}\lambda l_{wy}}{r_0}\tilde{y}_{t2} + \frac{2f_{11}L_{wy}^2 - K_x L_{wx}}{R_2}, \quad (3.5)$$

$$m_v s^2 \tilde{y}_v = 2sL_{yi}(s)(\tilde{y}_{w1} - \tilde{y}_v) + 2sL_{yi}(s)(\tilde{y}_{w2} - \tilde{y}_v) + \frac{m_v V}{2}\left(\frac{1}{R_1} + \frac{1}{R_2}\right) - \frac{m_v g}{2}(\theta_{c1} + \theta_{c2}), \quad (3.6)$$

$$I_v s^2 \tilde{\theta}_v = 2sL_{yi}(s)l_{wx}(\tilde{y}_{w1} - \tilde{y}_v) + 2sL_{yi}(s)l_{wx}(\tilde{y}_v - \tilde{y}_{w2}) + 2sL_{xj}(s)l_x^2(\tilde{\theta}_{w1} - \tilde{\theta}_v) + 2sL_{xj}(s)l_x^2(\tilde{\theta}_{w2} - \tilde{\theta}_v) - 4sL_{yi}(s)l_{wx}^2\tilde{\theta}_v. \quad (3.7)$$

In these equations, s denotes the Laplace variable and for example $\tilde{y}_{w1}$ represents the Laplace transform of $y_{w1}(t)$. All parameters are defined in Table 3.1, expressions for the creep coefficients f_{11}, f_{22} and f_{23} can be seen in Section 3.2.2, and the contact angle parameter which introduces gravitational stiffness and spin creepage terms into Eqs. (3.2 - 3.7) is evaluated as follows [106],

$$\varepsilon = a_c(\lambda - \lambda_0). \quad (3.8)$$

Symbol	Parameter	Unit	Value
V	Vehicle forward speed	ms^{-1}	$1-35$
V_{op}	Vehicle nominal operational velocity	ms^{-1}	31
m_w	Wheelset mass	kg	1.25×10^3
I_w	Wheelset yaw inertia	kgm^2	700
m_v	Carbody mass	kg	3×10^4
I_v	Carbody yaw inertia	kgm^2	5.58×10^5
l_x	Semi-lateral spacing between longitudinal suspension	m	1
l_{wx}	Half the wheelset spacing	m	4.5
l_{wy}	Half the vehicle gauge	m	0.7
λ	Wheel conicity	-	0.2
λ_0	Base cone profile	-	0.05
r_0	Nominal wheel radius	m	0.45
y_{t1}	Lateral track displacement at front wheelset	-	–
y_{t2}	Lateral track displacement at rear wheelset	-	–
R_1	Radius of curved track at front wheelset	m	1×10^3
R_2	Radius of curved track at rear wheelset	m	1×10^3
θ_{c1}	Cant angle of curved track at front wheelset	rad	$\pi/30$
θ_{c2}	Cant angle of curved track at rear wheelset	rad	$\pi/30$
g	Gravitational acceleration	ms^{-2}	9.81
K_y	Default lateral stiffness per axle box	Nm^{-1}	2.555×10^5
K_x	Default longitudinal stiffness per axle box	Nm^{-1}	1×10^6
c_{sy}	Default lateral damping per axle box	Nsm^{-1}	1.51×10^4
c_{sx}	Default longitudinal damping per axle box	Nsm^{-1}	4×10^3
A_l	Lateral track roughness factor	m	1.886×10^{-9}
v	Poisson's ratio of steel	-	0.3
E	Young's Modulus of steel	Pa	2×10^{11}
N	Nominal normal force at each contact patch	N	7.971×10^4
a_c	Contact angle constant	-	50.7
C_{11}	Longitudinal Kalker coefficient	-	1.65
C_{22}	Lateral Kalker coefficient	-	1.43
C_{23}	Spin Kalker coefficient	-	0.579
f_{11}	Longitudinal creep coefficient	N	1.291×10^7
f_{22}	Lateral creep coefficient	N	1.119×10^7
f_{23}	Spin creep coefficient	N	2.835×10^4

Table 3.1 Parameters relating to the modelling of the two-axle railway vehicle shown in Fig. 3.2, along with their symbols and units where applicable. The Kalker coefficients and contact angle constant are taken from [106], and the creep coefficients are calculated in Section 3.2.2.

The gravitational stiffness term takes into account the nonlinearity introduced by the increasing asymmetry in the normal loads with increased lateral displacements. The external forces acting on the model arise from the track's cant angle, θ_c, radius of curvature, R, and lateral displacement, y_t, from an average lateral datum which arises from irregularities due to heat distortion, wear, and manufacturing shortcomings. The internal forces come about from the longitudinal and lateral suspension configurations;

$L_{xj}(s)$ and $L_{yi}(s)$ respectively; along with gravitational stiffness due to the miss-match between each wheel's conicity and its base cone profile angle, and the creep forces at the wheel-rail contact points. To simplify the analysis, similar to previous studies [101, 103, 18, 97, 102] it is assumed that all contact patches are circular, the track is infinitely stiff, and nonlinear friction saturation is not included in the analysis.

The use of the contact angle parameter, ε, increases the accuracy of the model compared with [101, 103]. Equations (3.2 - 3.7) can be re-arranged to state-space form

$$s^2 x = A(s)x + Bu. \tag{3.9}$$

$A(s)$, the system matrix, captures the internal dynamics, and can be written after appropriate algebraic manipulation as

$$\mathrm{A(s)} = \begin{bmatrix} A_1 & \frac{2f_{22}}{m_w} & 0 & 0 & \frac{2sL_{yi}(s)}{m_w} & \frac{2sL_{yi}(s)l_{wx}}{m_w} \\ \frac{2f_{11}\lambda l_{wy}}{r_0 I_w} & A_2 & 0 & 0 & 0 & \frac{2sL_{xj}(s){l_x}^2}{I_w} \\ 0 & 0 & A_1 & \frac{2f_{22}}{m_w} & \frac{2sL_{yi}(s)}{m_w} & -\frac{2sL_{yi}(s)l_{wx}}{m_w} \\ 0 & 0 & -\frac{2f_{11}\lambda l_{wy}}{r_0 I_w} & A_2 & 0 & \frac{2sL_{xj}(s){l_x}^2}{I_w} \\ \frac{2sL_{yi}(s)}{m_v} & 0 & \frac{2sL_{yi}(s)}{m_v} & 0 & -\frac{4sL_{yi}(s)}{m_v} & 0 \\ \frac{2sL_{yi}(s)l_{wx}}{I_v} & \frac{2sL_{xj}(s){l_x}^2}{I_v} & -\frac{2sL_{yi}(s)l_{wx}}{I_v} & \frac{2sL_{xj}(s){l_x}^2}{I_v} & 0 & A_3 \end{bmatrix}, \tag{3.10}$$

with substitutions,

$$A_1 = -\frac{2sL_{yi}(s)}{m_w} - \frac{2sf_{22}}{Vm_w} + \frac{2\varepsilon}{l_{wy}m_w}\left(N - \frac{f_{23}}{r_0}\right), \tag{3.11}$$

$$A_2 = -\frac{2sL_{xj}(s){l_x}^2}{I_w} - \frac{2sf_{11}{l_{wy}}^2}{I_w V}, \tag{3.12}$$

$$A_3 = -\frac{4s(L_{xj}(s){l_x}^2 + L_{yi}(s){l_{wx}}^2)}{I_v}. \tag{3.13}$$

required, and all parameters detailed in Table 3.1.

The input matrix, u, consists of either a timeseries of lateral track displacements (either from real track data or filtered white noise; see Section 3.2.1) for the passenger comfort case, or ramped timeseries of cant angle and radius of curvature for the curving performance case (see Fig. 3.3). The size of matrix B, which captures the dynamics associated with external forcing, depends on the inputs involved in the analysis. Passenger comfort assessment is performed on a nominally straight track, but with some lateral irregularities, resulting in a B matrix of

$$B_s = \begin{bmatrix} 0 & 0 \\ \dfrac{-2f_{11}\lambda l_{wy}}{r_0 m_w} & 0 \\ 0 & 0 \\ 0 & \dfrac{-2f_{11}\lambda l_{wy}}{r_0 m_w} \\ 0 & 0 \\ 0 & 0 \end{bmatrix}, \tag{3.14}$$

where the columns relate respectively to the lateral track displacements $\tilde{y}_{t1}$ and $\tilde{y}_{t2}$. However, when assessing curving performance, it is assumed that these irregularities are negligible (similar to the analysis in [101, 103, 22]), as the steady-state lateral vehicle displacement is the primary concern. The inputs now become the track's cant angle and radius of curvature, leading to a B matrix of

$$B_c = \begin{bmatrix} V^2 & -g & 0 & 0 \\ \dfrac{2(f_{11}l_{wy}^2 + K_x L_{wx} l_x^2)}{Iw} & 0 & 0 & 0 \\ 0 & 0 & V^2 & -g \\ 0 & 0 & \dfrac{2(f_{11}l_{wy}^2 - K_x L_{wx} l_x^2)}{Iw} & 0 \\ V^2/2 & -g/2 & V^2/2 & -g/2 \\ \dfrac{-2K_x L_{wx} l_x^2}{Iv} & 0 & \dfrac{2K_x L_{wx} l_x^2}{Iv} & 0 \end{bmatrix}, \tag{3.15}$$

with the columns respectively relating to the inputs: R_1^{-1}, θ_{c1}, R_2^{-1} and θ_{c2}. The resulting transfer function

$$H_\omega = (s^2 I - A(s))^{-1} B, \tag{3.16}$$

in which I denotes the 6×6 identity matrix, can be obtained and employed in MATLAB® and SIMULINK® to calculate resulting displacements, velocities and accelerations of all six states.

3.2.1 Assessing passenger comfort

The Mean Comfort Standard Method, defined in EN 12299:2009 [107], is nominally used to assess a vehicle's passenger comfort. This method uses the 95th percentile of frequency weighted RMS carbody accelerations and is used as a standard when assessing passenger comfort on real vehicles with the use of accelerometers positioned on seats [108]. This thesis, however, focuses on the relative benefits that the inerter can bring to railway vehicles, and as a simplified model is being used, comparisons with other more realistic models becomes less of an issue, and therefore the RMS lateral carbody acceleration is used as a measure of passenger comfort. This is in line with previous studies [19, 18, 103, 102]. J_{5y} represents the passenger comfort cost function

$$J_{5y} = \sqrt{\int_0^\infty |A_c(t)|^2 \, dt}, \tag{3.17}$$

J represents RMS acceleration, subscript 5 the fifth state (carbody), and subscript y the lateral direction. $A_c(t)$ is a timeseries of the resulting lateral carbody acceleration when the model is subject to one of two different types of track input, defined as follows:

- *Real track data*: This comes in the form of lateral track displacement from a central datum for a 5 km length of track. These lateral track irregularities simulate defects relating to manufacturing faults and heat expansion and contraction variations. Lateral, vertical and gauge variations are available, however as this analysis assumes constant gauge, and is entirely in the horizontal plane, only lateral variations are used. All three track irregularity variations are used in the analysis of a four-axle vehicle in Chapter 6. Data for tracks with rated velocities of 110 kph and 160 kph are respectively defined in the rest of this thesis as Track110 and Track160, and with the knowledge of the vehicle's forward velocity, and hence the time delay between the front and rear wheelsets,

  $$T_d = \frac{2l_{wx}}{V}, \tag{3.18}$$

  timeseries of these tracks can be obtained and defined as the inputs $\tilde{y}_{t1}$ and $\tilde{y}_{t2}$ in the input matrix u in Eq. (3.9).

- *Random Track input*: The magnitude of the lateral track displacement is modelled in this case using filtered white noise. These irregularities have been simulated in

the frequency domain [103, 102], using techniques developed in [21]. The output of the velocity dependent single sided power spectrum

$$S_y(f_s) = \frac{A_l}{f_s^2}, \tag{3.19}$$

$$S_{\dot{y}} = 4\pi^2 A_l V^2, \tag{3.20}$$

where f_s is a spatial frequency in cycles/m and A_l the track roughness factor, is passed through the filter $H_1(s)$

$$H_1(s) = \frac{21.69s^2 + 105.6s + 14.42}{s^3 + 30.64s^2 + 24.07s} \tag{3.21}$$

and used as the system input. Parceval's Theorem, which states that the sum of the square of a function is equal to the sum of the square of its corresponding Fourier transform, is used to enable Eq. (3.17) to be written in the frequency domain

$$\int_0^\infty |A_c(t)|^2 \, dt = \frac{1}{2\pi} \int_0^\infty |A_c(jw)|^2 \, dw. \tag{3.22}$$

Equations

$${J_{5y}}^2 = \frac{1}{2\pi} \int_0^\infty \left| S_{\dot{y}} H_1(jw) G(jw)(1 - e^{-j\omega T_d}) \right|^2 dw \tag{3.23}$$

and

$$J_{5y} = \sqrt{\frac{\Delta\omega S_{\dot{y}}}{2\pi} \sum_0^{30\pi} \left| H_1(jw) G(jw)(1 - e^{-j\omega T_d}) \right|^2} \tag{3.24}$$

show how the resulting J_{5y} is calculated, with $G(jw)$ being defined as the transfer function with an input of the lateral track displacement at the front wheelset, and an output of the lateral carbody acceleration.

3.2.2 Assessing trackwear

The trackwear, or curving performance of the railway vehicle model is assessed by quantifying the energy lost at the contact point, T_γ. This industrially recognised parameter captures the detrimental effects on the wheels and rails produced by curving. As discussed in Section 3.2, the 6×4 B matrix, seen in Eq. (3.15), is used for curving

analysis, with the system inputs ${R_1}^{-1}$, θ_{c1}, ${R_2}^{-1}$ and θ_{c2}. These take the form of ramps in the time domain with a 1 second transition period when entering and leaving a curve (using the same input method described in [101]), and an appropriate time delay between wheelsets based on the vehicle speed and wheelset separation distance (see Fig. 3.3 and Eq. (3.18)). The following is a derivation of T_γ.

The longitudinal and lateral creepages, v_{x1l} and v_{y1l},

$$v_{x1l} = \frac{l_{wy}\dot{\theta_{w1}}}{V} + \frac{\lambda y_{w1}}{r_0} - \frac{l_{wy}}{R_1}, \tag{3.25}$$

$$v_{y1l} = \frac{\dot{y_{w1}}}{V} - \theta_{w1}, \tag{3.26}$$

are used to calculate the relative velocity between the wheel and rail, and the spin creepage, v_{z1l},

$$v_{z1l} = \frac{\varepsilon}{r_0 l_{wy}} y_{w1}, \tag{3.27}$$

arising from the thickness of the contact patch, includes the contact angle parameter, ε [106]. Note that subscripts 1, l, x and y represent respectively the wheelset number (front), the left wheel, and the lateral and longitudinal directions. The contact patch dimension product, defined as ab

$$ab = \left[\frac{1.5(1-\nu^2)Nr_0}{E}\right]^{2/3}, \tag{3.28}$$

is a function of the average normal force of the vehicle per wheel, N, Poisson's Ratio of steel, ν, and the nominal wheel radius, r_0. To perform the conversion from creepages to creep forces, creep force coefficients f_{11}, f_{22} and f_{23}

$$f_{11} = EC_{11}ab, \tag{3.29}$$

$$f_{22} = EC_{22}ab, \tag{3.30}$$

$$f_{23} = EC_{23}ab, \tag{3.31}$$

which depend respectively on the Kalker coefficients C_{11}, C_{22} and C_{23} [109], are determined. The longitudinal and lateral creep forces,

$$F_{x1l} = f_{11} v_{x1l}, \tag{3.32}$$

$$F_{y1l} = f_{22} v_{y1l} + f_{23} v_{z1l}, \tag{3.33}$$

respectively are then used to calculate T_γ

$$T_{\gamma 1l} = F_{x1l} v_{x1l} + F_{y1l} v_{y1l}, \tag{3.34}$$

for the front wheelset's left wheel [109, 1]. When presenting data in Chapter 4, the mean value of T_γ over all four wheels is used as a measure of trackwear; the values for the other wheels are determined using exactly the same approach. The value of T_γ depends on the square of both the lateral and longitudinal creepages. This analysis assumes clean, dry conditions with a coefficient of friction value of $\mu = 0.6$, and a linear relationship between creepage and creep force [109]. It should be noted that T_γ is not a true representation of wear. A British Rail wear model, discussed in [110, 111], itself a different function of T_γ for moderate, transitory, and severe wear, is often used to express the wear as an area loss measured in mm^2 per kilometre travelled. Using T_γ however is sufficiently detailed for the analysis presented in this thesis.

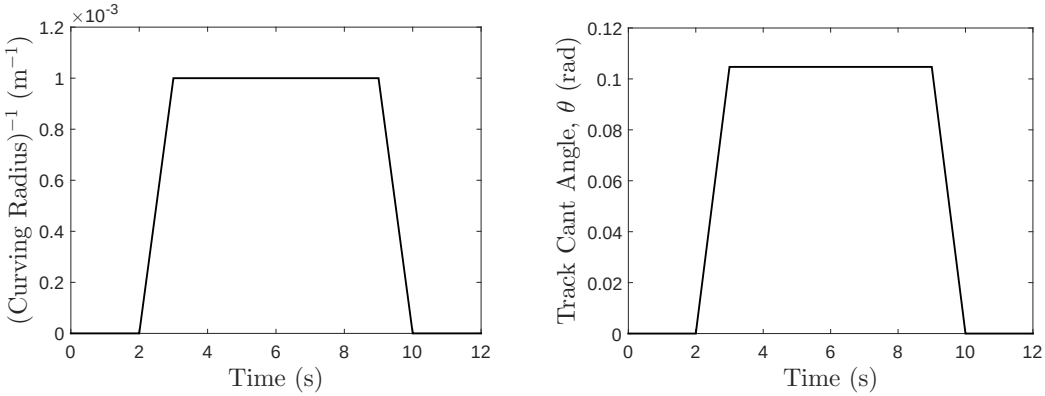

Fig. 3.3 Ramped inputs of the inverse of the tracks' curving radius (${R_1}^{-1}$), and the cant angle (θ_{c1}), both at wheelset 1. The same inputs occur at wheelset 2 but including the time delay, T_d.

Figures 3.4(a)-(f) display wheelset displacements, carbody accelerations, and T_γ values when the PYS is at its default value of $K_x = 1{\times}10^6$ Nm^{-1}, and $K_x = 3{\times}10^6$ Nm^{-1}, using the default, L_{y1} lateral suspension configuration (See Table 3.1 for parameter values). Note that K_x, the static longitudinal or yaw stiffness, is referred to as the Primary Yaw Stiffness (PYS) in Chapters 3 and 4 for continuity purposes when comparing with subsequent chapters in this thesis. The discrepancy between the front and rear wheelset lateral displacements in Figs. 3.4(a) and (b) arises from the

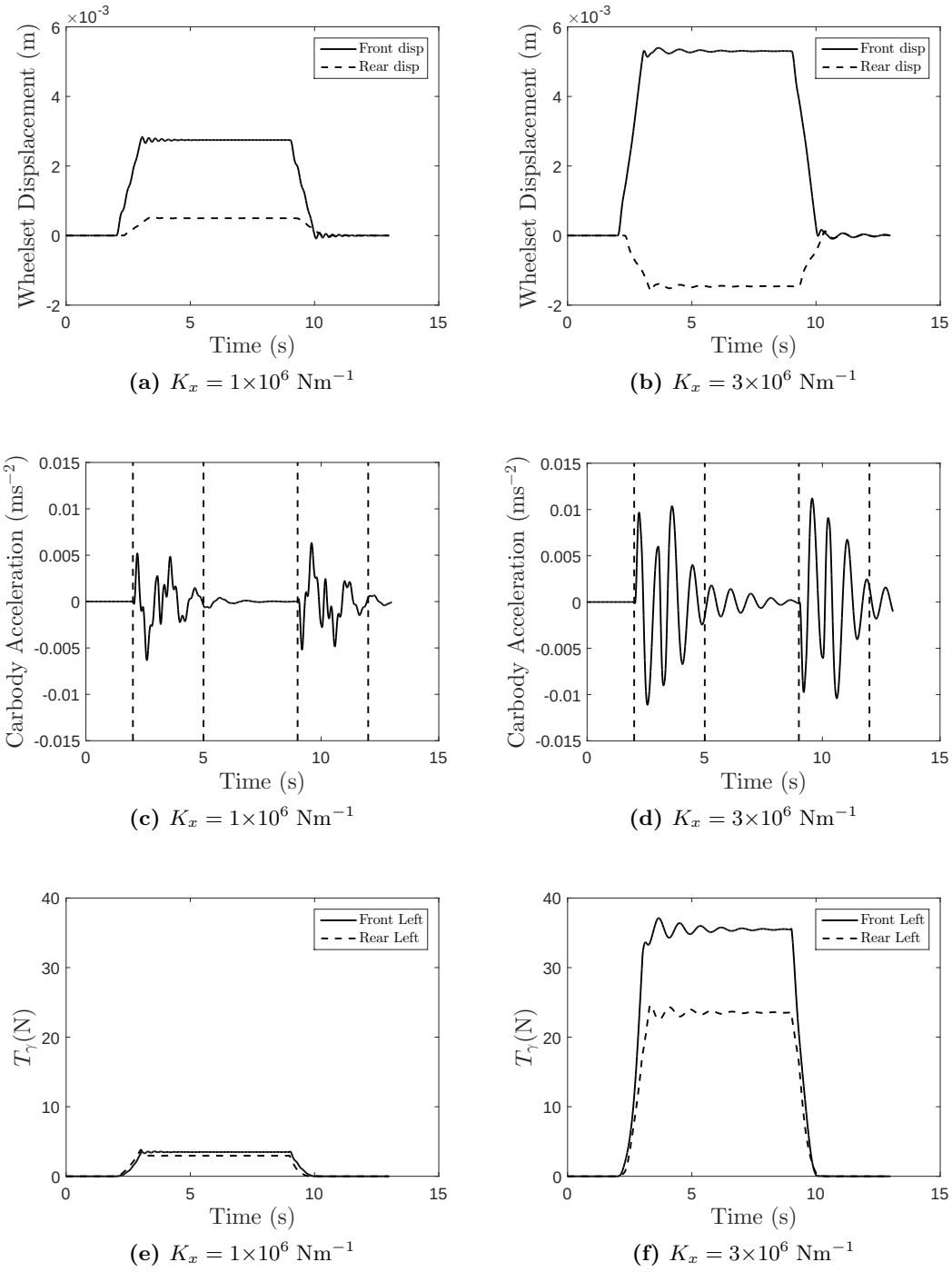

(a) $K_x = 1{\times}10^6$ Nm^{-1} **(b)** $K_x = 3{\times}10^6$ Nm^{-1}

(c) $K_x = 1{\times}10^6$ Nm^{-1} **(d)** $K_x = 3{\times}10^6$ Nm^{-1}

(e) $K_x = 1{\times}10^6$ Nm^{-1} **(f)** $K_x = 3{\times}10^6$ Nm^{-1}

Fig. 3.4 Front and rear wheelset displacement, carbody acceleration and T_γ vs time under curving conditions, using the default L_{y1} and L_{x1} lateral and longitudinal suspension configurations, and at two different PYS values. The simulation velocity remains at V_{op}.

radius of curvature and the PYS causing an equal and opposite net moment on the wheelsets [101, 103]. Assessing the transient carbody acceleration occurring in both of

the three second periods immediately after the start of each transition (see Figs 3.4(c) and (d)), it can be seen that the acceleration here is negligible when compared with the optimised accelerations found from the analysis in Chapter 4, Section 4.2.3. For example, the transient RMS acceleration of 0.0058 ms^{-2}, seen between the vertical dashed lines in Fig. 3.4(d), is 9.7% of the lowest acceleration found in Chapter 4, Section 4.2.3. This value rises to only 16.5% for the worst case transient acceleration scenario. The subsequent trackwear analysis therefore does not put any emphasis on acceleration induced by curving. Figs. 3.4(e) and (f) show that the wheelsets remain in equilibrium due to the higher wheel-rail contact forces on the front wheel, and note that T_γ at the front and rear right wheel is predicted to be identical to that of the front and rear left wheel respectively. This is due to the symmetric vehicle set-up and perfect conical nature of the wheels resulting in identical absolute lateral and longitudinal creepage magnitudes (see Eqs. (3.25, 3.26)).

This section has established the methods by which passenger comfort and curving performance are assessed, T_γ as the measure of trackwear, and it can be concluded that the assessment of trackwear produces intuitive results in terms of wheelset displacement and contact patch forces. The model and analysis techniques established here will be used in Chapter 4.

3.3 The four-axle passenger vehicle model in VAMPIRE®

This section details the VAMPIRE® four-axle vehicle model used in Chapters 5 and 6 of this thesis, including details on how the inerter is included. This model is representative of a typical multiple unit passenger vehicle with a maximum operating speed of 75 mph (33.5 ms^{-1}). In Chapter 6, candidate inertance-integrated layouts for the primary lateral suspension are proposed using the structure-immittance approach, and these are then optimised for the vehicle model. Note that the design method for inertance-integrated suspensions proposed here can be applied to other railway vehicle models.

3.3.1 Vehicle modelling

As introduced in Section 3.1, the analysis presented in Chapter 6 is based on the Vehicle Track Interaction Strategic Model (VTISM) [7] library vehicle: *BogiePassenger 39t 15yaw* (*39t* denotes a total carriage weight of 39 tonnes, and *15yaw* a total PYS of 15 MNm/rad). It is a four-axle model which is representative of a typical multiple unit passenger vehicle, operating up to 33.5 ms^{-1} and weighing 39 tonnes. Figure 3.5 shows a 3D view (from the VAMPIRE® software) of the make up one of the vehicle's bogies, with the components of interest (the primary vertical spring and trailing arm bush) highlighted. Note that the bogie body itself has been removed for clarity, and the overall structure is simplified.

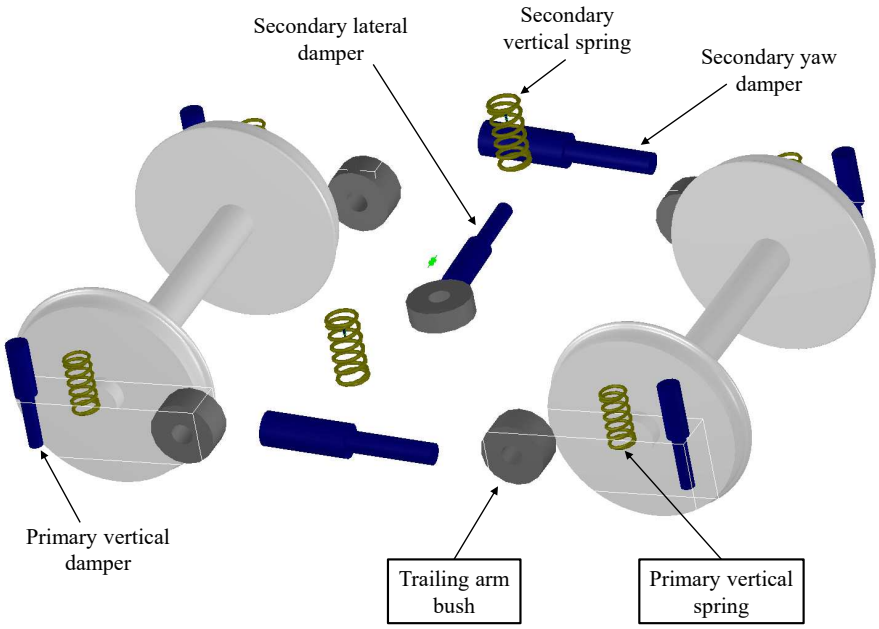

Fig. 3.5 A 3D view of one of the two *BogiePassenger 39t 15yaw* vehicle bogies, with various suspension components labelled. Note the boxes indicate the components that are of particular interest, and the bogie frame and corresponding connections have been removed to simplify viewing.

Figure 3.6 shows a horizontal plane schematic view of one bogie, detailing the make-up of the primary lateral and longitudinal suspensions. Note that the bogie frame, heavily simplified, is now depicted by the outer black box, and only the primary suspension components that act in the horizontal plane are shown. The red box marked ② in Fig. 3.6 shows the lateral contribution of the trailing arm bush, which will be subsequently referred to as the *primary lateral suspension*, and is the suspension which is optimised in Chapter 6. Its default layout is shown in Fig. 3.6. Table 3.2 lists the default suspension parameter values of the trailing arm bush, and the lateral and longitudinal shear components of the primary vertical spring. It can be seen from Fig. 3.6 that the PYS of each wheelset is made up of the radial stiffness of the trailing arm bush (k_{bx}) and the longitudinal shear stiffness of the primary vertical spring (K_{sx}). The PYS can therefore be expressed as,

$$\text{PYS} = 2a(k_{bx} + K_{sx}), \tag{3.35}$$

where a (=1 m) denotes the semi-lateral spacing between the trailing arm bushes. Based on the stiffnesses defined in Table 3.2, the total PYS is 15 MNm/rad; with 93% of this coming from k_{bx}. As the longitudinal shear stiffness arises from the primary vertical springs, this is considered fixed, hence in the optimisations of Chapter 6 the static longitudinal stiffness of the trailing arm bush (k_{bx}) will be the cost function to be reduced.

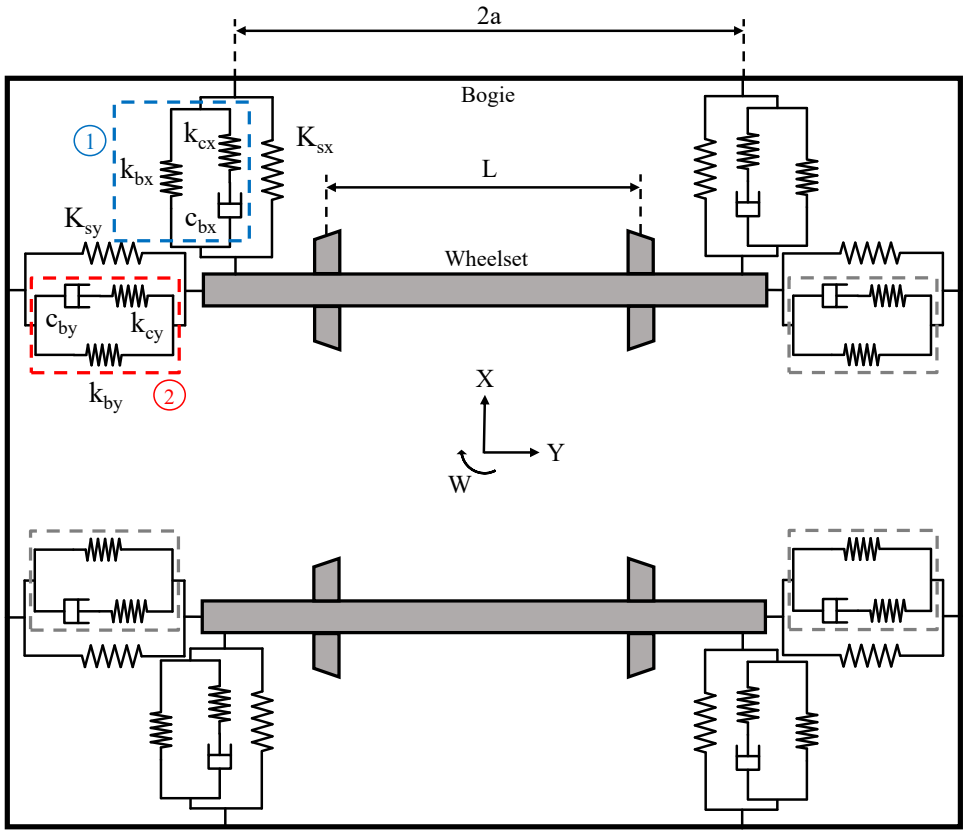

Fig. 3.6 A schematic detailing of one of the bogies in the VTISM four-axle vehicle model. Subscript s denotes the shear component of the primary vertical springs. Symbols ① and ② detail respectively the default longitudinal and lateral stiffness and damping components of the trailing arm bush. X denotes the longitudinal direction (direction of travel), Y the lateral direction, and W the yaw rotation.

Parameter	Symbol	Unit	Value
Trailing arm bush lateral static stiffness	k_{by}	MNm^{-1}	1.75
Trailing arm bush lateral damping	c_{by}	$kNsm^{-1}$	1.75
Trailing arm bush lateral damping end stiffness	k_{cy}	$kNsm^{-1}$	3.75
Primary spring lateral shear stiffness	K_{sy}	MNm^{-1}	0.50
Trailing arm bush longitudinal static stiffness	k_{bx}	MNm^{-1}	7.00
Trailing arm bush longitudinal damping	c_{bx}	$kNsm^{-1}$	7.00
Trailing arm bush longitudinal damping end stiffness	k_{cx}	MNm^{-1}	14.0
Primary spring longitudinal shear stiffness	K_{sx}	MNm^{-1}	0.50

Table 3.2 The default suspension parameter values of the 39-tonne *BogiePassenger 39t 15yaw* VTISM four-axle railway vehicle model. The overall PYS calculation is discussed in Section 3.3.1 and presented in Eq. (3.35).

3.3.2 Conicity and wheel-rail contact modelling

The concept of wheel-rail equivalent conicity and the methods by which contact patch creep forces are simulated are important when assessing a vehicle's dynamic behaviour. Conicity is a measure of the effective cone angle of the wheel profile with respect to the rail. This conicity, along with the wheel flange, allows the vehicle to steer around curves and resist derailment, and plays a key role when determining the vehicle's kinematic, or hunting, oscillation. The wavelength of this oscillation, the Klingel wavelength [112], is calculated from,

$$\Lambda = 2\pi\sqrt{\frac{r_0 L}{\lambda}}, \tag{3.36}$$

where r_0 is the nominal wheel radius, L is the lateral distance between the contact points (see Fig. 3.6), and λ is the wheel conicity.

The rolling-radius-difference (rrd, between the left and the right wheel) caused by the presence of wheel conicity causes this simple harmonic oscillation, which induces the vibration of numerous vehicle modes. A high conicity generally produces a short Klingel wavelength, higher carbody accelerations, and thus poorer passenger comfort. The shorter Klingel wavelength arising from a lower conicity, resulting in generally lower carbody accelerations, also means that flange contact is more likely. In reality, however, the wheel profile is curved, rather than perfectly conical, and the term equivalent conicity is used [113]. Equivalent conicity can be considered the *average* conicity of a wheelset, and is defined as the conicity of a perfectly conical wheelset which has the same Klingel wavelength as the wheelset in question.

To improve the computational efficiency of the optimisation presented in Chapter 6, linear, or constant, conicity is used in Section 6.2 to identify beneficial configurations, along with a linear creep law with the half-creep friction saturation simplification. In Section 6.3 however, measured nonlinear wheel-rail contact data is used along with fully nonlinear friction saturation with a coefficient of friction value of 0.32. It should be noted that the equivalent conicity of the measured wheel-rail contact data has been measured (or inferred from the rrd) at a 3 mm lateral offset, i.e. when the wheelset has moved 3 mm laterally from the centreline. In practice it is impossible to give a single value of equivalent conicity for a given wheel-rail pair, as equivalent conicity will vary with lateral offset. In the UK it is standard practice to give the equivalent conicity for a wheel-rail pair based on a lateral offset of 3 mm. The equivalent conicity may take a slightly different value when calculated from the rolling radius difference measured at a different lateral offset, but a 3 mm lateral offset produces the most representative overall wheel-rail equivalent conicity.

3.3.3 VAMPIRE® modelling techniques, including the inerter's implementation

This section provides a brief overview of the capabilities of the VAMPIRE® software, the methods used to model and run vehicle simulations within VAMPIRE®, and the means by which the inerter is added to the vehicle model, and an external validation case study.

An overview of the VAMPIRE® modelling and simulation process

VAMPIRE® is a widely used, multi-body railway vehicle dynamics modelling software, who's simulation capabilities are wide ranging. Any custom made railway vehicle may be built using the numerous file types detailed below, and many *built-in* pieces of analysis are available (e.g. assessment of straight running and curving performance with certain track files, peak counting acceleration analysis, and a variety of other assessment standards).

In Chapter 6 of this thesis, VAMPIRE® is used extensively to perform vehicle simulations, however the main problem encountered when attempting to improve passive suspension design is that VAMPIRE® *itself* is unable to perform optimisations on certain suspension parameters. It is for this reason that VAMPIRE® and MATLAB® are used in conjunction with one another in Chapter 6, with MATLAB® calling VAMPIRE® every optimisation iteration. The optimisation procedure is discussed in more detail in Chapter 6, Section 6.2.2. Below are a list of the four main files (editable in Notepad with strict syntax requirements and constraints) which are required to build and simulate a vehicle in VAMPIRE®.

- **VAC files**. These files can be thought of as being at the top of the VAMPIRE® simulation hierarchy. A VAC file (VAMPIRE® command file) details the overall task, and allows the user to alter any parameter values within the run or vehicle file with the *replace* command. This important aspect is crucial when performing optimisations, because at each optimisation iteration, the suspension parameters need to be updated via MATLAB®. Also, the conicity and speed can be varied at each iteration, allowing for a neater and more effective assessment of a number of conicity and speed situations.
- **RUN files**. A run file contains information regarding the system input (e.g. track type, speed, simulation step-size and time), the running conditions (e.g. linear or nonlinear wheel-rail contact law, conicity, friction) and finally the outputs that the user wishes to observe. These outputs range from displacements, velocities, and accelerations at any point on any DOF, to forces and T_γ values. The main outputs analysed in this thesis are carbody accelerations.

- **VEH files**. This type of file defines in detail the vehicle type, dimensions, and suspension configuration. Many of the components, and parameter values in the VTISM four-axle model used in this thesis are themselves parametrised and can be scaled with the vehicle's mass. The main elements that can be introduced are stiffness, damping, mass and bushing elements.
- **VAMPARAM files**. These VAMPIRE® parameter files can be included in the vehicle file, and are useful if multiple extra suspension structures need to be included. This is very much the case when considering the optimisation of the inertance-integrated trailing arm bush which is discussed in Section 3.3.3.

Including inerters in VAMPIRE® models

The means by which the inerter is included in VAMPIRE® vehicle models has been introduced in [105], and this thesis uses a similar method of implementation. The method makes use of a *theoretical* rack and pinion setup to realise the inerter concept, as shown in Fig. 3.7(a). Figure 3.7(b) shows the equivalent flywheel type inerter schematic, or connection, when modelled in VAMPIRE®, where the central mass is created with a pitch inertia value equal to the inertance required, and is grounded in all DOFs apart from that of pitch, so it will act as a free flywheel.

As the standard inerter equation cannot be inserted directly into VAMPIRE®, a stiffness link equation, which links the inerter flywheel to it's associated DOFs (equivalent to k_e in Fig. 3.7(b)) is used in the *vamparam* file to form the inerter connection:

$$\text{LINK} \qquad m_1 \text{ Y } 1.0 \qquad M_I \text{ P } -1.0 \qquad m_2 \text{ Y } -1.0 \tag{3.37}$$

Read in conjunction with Fig. 3.7(b), Eq. (3.37) exhibits the following physical meaning, with each line below relating to each set of three terms:

- A unit displacement of Mass 1 (m_1) in the left direction (Y) extends the spring by one unit (1.0).
- A unit pitch rotation (P) of the *flywheel* (M_I) compresses the spring by one unit (-1.0).
- A unit displacement of Mass 1 (m_2) in the left direction (Y) compresses the spring by one unit (-1.0).

This work-around for including the inerter in VAMPIRE® is necessary as the software cannot simply include the inerter's acceleration dependence equation, as it only has the ability to connect mass elements with spring and damping elements. It should be noted that the rotating DOF (pitch (P)) chosen here could have been any

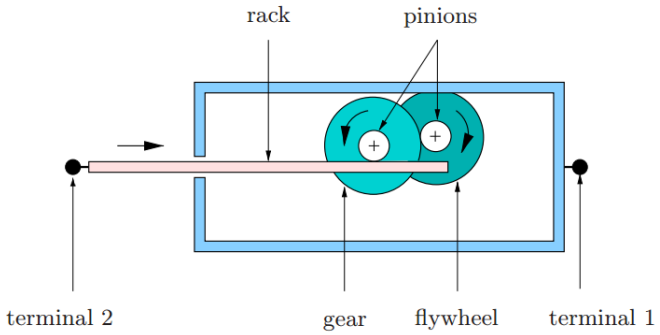

(a) Rack and pinion inerter [52].

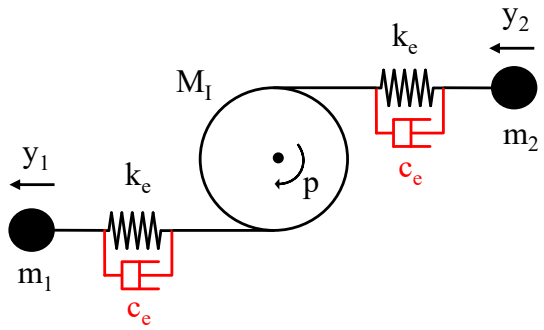

(b) The schematic of the inerter's implementation within VAMPIRE®.

Fig. 3.7 (a) A rack and pinion inerter device, reproduced from [52], along with (b) the equivalent schematic in VAMPIRE®, encompassing the stiffness and damping link equations.

one of roll (T), pitch (P) or yaw (W), as long as the lines of code responsible for the defining the *semi-fictitious* flywheel are consistent with one another.

Inerter validation case study

A simple two-mass system (see Fig. 3.8) is considered to validate the modelling of the inerter's implementation in VAMPIRE®, with the parameters used (roughly representative of those for a quarter-car railway vehicle model) summarised in Table 3.3. The input force, F_{ext}, which is step in nature, is applied at Mass 2 to excite the system.

The dynamics of an ideal inerter are captured in MATLAB® for comparison purposes. Using the inerter implementation method defined in Section 3.3.3, due to the inevitable need to simulate an inerter end-stiffness (k_e in Fig. 3.7(b)), high-frequency oscillations are observed in the system for both acceleration, velocity and displacement responses. These high-frequency oscillations are not present in the

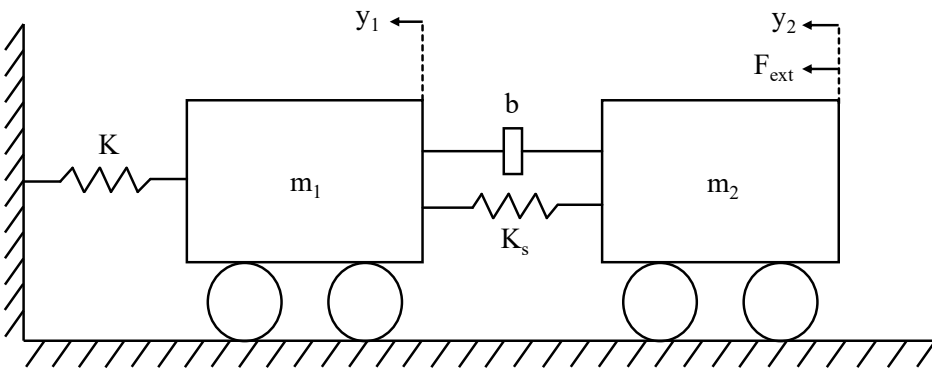

Fig. 3.8 The two-mass system used to study and validate the inerter's implementation in VAMPIRE®.

Parameter	Symbol	Unit	Value
Mass 1	m_1	Tonnes	1.25
Mass 2	m_2	Tonnes	15
Inertance	b	Tonnes	1
Stiffness mass 1 to ground	K	MNm^{-1}	0.35
Static stiffness	K_s	MNm^{-1}	2.5

Table 3.3 Parameter values of the two-mass system introduced in Fig. 3.8.

MATLAB® responses of the ideal inerter, as effectively the connections within it are infinity rigid.

To eliminate the erroneous high-frequency oscillations caused by the end-stiffness, an end-damping in parallel with the end stiffness (equivalent to c_e in Fig. 3.7(b)) is used. This end-damping is simulated using a damping link equation, which is written into VAMPIRE® in a similar manner to the stiffness link equation. The inerter property can now be successfully implemented in VAMPIRE®.

An example velocity response of the two-mass model is shown in Fig. 3.9 and details the ideal inerter response in MATLAB®, and VAMPIRE® responses using an inerter with and without end-damping. It can be seen that the VAMPIRE® response matches the ideal inerter response in VAMPIRE® when the end-damping component is introduced, yet when solely end-stiffness is used, high-frequency oscillations are induced. To further the validity of this analysis, when the end-stiffness is taken into account in the MATLAB® model the high-frequency oscillations encountered in VAMPIRE® are predicted to a high degree of accuracy.

It should be noted that for the complex VTISM four-axle railway vehicle model, the high-frequency oscillations caused by an end-stiffness have been mitigated due to the presence of many other dampers in the system. The damping link equation is

therefore not needed in this thesis, but it is mentioned to highlight that this effect should be, and has been, considered.

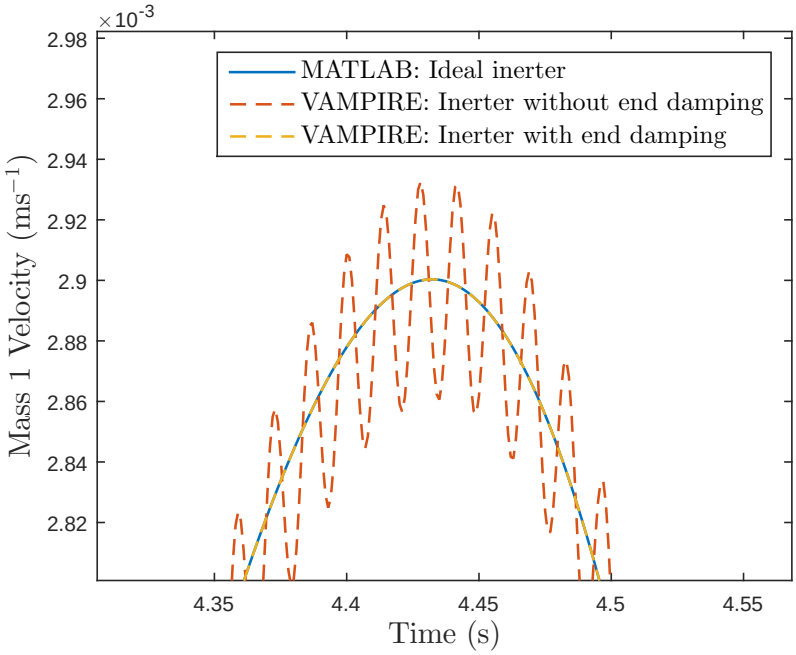

Fig. 3.9 Mass 1 velocity curves when a) MATLAB® is used to model an ideal inerter, b) VAMPIRE® is used with end end stiffness but no end damping, and c) when an end damping is introduced to VAMPIRE® with the use of a link equation.

3.4 Summary

This chapter has provided a framework of the models and methods that will be used in this thesis to analyse the inerter's application to railway vehicles. The first model which has been introduced is the 6 DOF, two-axle, MATLAB® railway vehicle model, typical of a freight vehicle wagon. The inputs to the system are ramped timeseries of track curvature and cant angle, and certain different types of lateral track input used to assess respectively straight running and curving performance. The methods by which these two performance indices are quantified are introduced and discussed, with both Random and standard (real) rated tracks being used to assess the vehicle's passenger comfort, and T_γ being used as the performance measure for trackwear. Initial assessments of the vehicle's curving performance with the default lateral suspension structure yield that transient carbody accelerations in the transition period are negligible in comparison to the carbody accelerations found in Chapter 4 when assessing straight running performance.

Also in this chapter, the four-axle VAMPIRE® vehicle model is introduced, and aspects such as the suspension layouts and equivalent conicity are discussed.

VAMPIRE® is briefly introduced as a widely-used multi-body dynamics modelling software, with many different file types and their applications to this project discussed. The process by which inerters are modelled in VAMPIRE® is defined and a case study is presented on how to mitigate the end-stiffness effects that the inerter inherently brings, when working in an environment that is predominately made up of mass and spring elements.

This thesis makes use of the models and techniques introduced in this chapter in the following ways:

- Chapter 4 uses the two-axle, MATLAB® model to assess how curving and straight running performance can be concurrently improved by the use of optimised inerter-based lateral suspensions.
- Chapter 5 uses exported mass, spring and damping matrices from the VTISM four-axle VAMPIRE® model to assess the applicability of the Laplace to time-domain *location matrix* modelling technique.
- Chapter 6 focuses solely on the four-axle VAMPIRE® model and uses MATLAB and VAMPIRE in conjunction to perform optimisations and nonlinear validation tests on the realistic vehicle.

Chapter 4

Two-axle model passenger comfort and trackwear enhancement

In this chapter we:

- Propose beneficial inerter-based lateral suspension layouts and analyse the differences between the straight running track inputs by means of a PSD analysis.
- Perform optimisations of these lateral suspensions for reduced RMS lateral carbody acceleration, hence improved passenger comfort.
- Analyse how the vehicle, running over tracks rated at two different speeds, performs at a range of velocities with the optimised lateral suspension configurations.
- Show that the trade-off between straight running and curving performance can be improved by the use of inerters in the lateral suspension; a PYS reduction is achievable whilst the carbody acceleration is maintained, or even reduced.
- Demonstrate that the use of an optimised longitudinal HALL-bush can further improve this concurrent passenger comfort and trackwear enhancement.
- Analyse how using a half-creep wheel-rail contact law varies the RMS carbody acceleration's dependency on the PYS.

4.1 Introduction

Whilst Chapter 3 presented the models and method that are employed throughout this thesis, Chapter 4 presents analysis and results relating to a two-axle railway vehicle model. As stated in Chapters 1 and 2, the overall aim of this project is to concurrently improve trackwear and ride comfort with the use of inerter-based lateral suspensions. Whilst inerters have been studied previously to an extent in railway vehicles [42, 97–104], no studies as of yet have analysed and attempted to concurrently

improve both the trade-off described above, or used a variety of different real-world track inputs.

To this end, this chapter serves as an initial assessment to determine the extent to which the passenger comfort vs trackwear trade-off can be diminished. A 6 DOF MATLAB® model is employed, with equations of motion set up to neatly allow the admittance functions of interchangeable suspension networks to be implemented. RMS lateral carbody acceleration is used as the measure of passenger comfort and T_γ for trackwear. It should be noted that throughout this thesis, and especially in this chapter, T_γ is used as the primary measure of the extent of RCF and wear. As we are working with moderate values of T_γ, RCF will dominate, but to simplify the analysis, a reduction in T_γ will be referred to a reduction or improvement in trackwear.

The structure of this chapter is as follows. Firstly, the candidate lateral suspensions and their transfer functions are introduced, and the different types of track data are analysed. Results of passenger comfort optimisations are detailed, and subsequently a *reality check* continuous velocity style assessment takes place. Finally, the extent to which the trade-off between trackwear and passenger comfort can be improved is detailed, both with and without an optimised longitudinal HALL-bush.

The results presented and discussed in this chapter were reported in the following publications:

- T. D. Lewis, J. Z. Jiang, S. A. Neild, C. Gong, and S. D. Iwnicki. Using an inerter-based suspension to improve both passenger comfort and trackwear in railway vehicles. *Vehicle System Dynamics: International Journal of Vehicle Mechanics and Mobility*, 2019.

- T. D. Lewis, J. Z. Jiang, S. A. Neild, C. Gong, and S. D. Iwnicki. Improving ride comfort and trackwear of two-axle railway vehicles using inerter-based lateral suspension layouts. *Proceedings of the 6th Conference; Noise and Vibration Emerging Methods (NOVEM)*, 2018.

4.2 Ride comfort enhancement using a two-axle model

The initial focus of this chapter is the optimisation of the lateral suspension for reduced RMS carbody acceleration, hence improved passenger comfort. The candidate suspension layouts are introduced first, as the structure-based approach to network-synthesis and optimisation will be used. Next, the differences in the track types will be discussed by assessing the differences in their lateral irregularity Power Spectral Densities (PSDs). Finally, optimisations for each layout lead on to continuous velocity assessments.

4.2.1 Suspension layouts

In [101] and [103], six different $L_{yi}(s)$ layouts were investigated as candidate lateral suspensions. These, and the two different $L_{xj}(s)$ layouts, are employed in the following analysis in the lateral and longitudinal suspensions respectively (see Fig. 4.1). K_y and K_x denote constant static stiffnesses, k_{sy} and k_{sx} optimisable spring stiffnesses, c_{sy} and c_{sx} optimisable damping coefficients, and b_{sy} and b_{syp} optimisable series and parallel inertance values respectively. The default values of K_y, K_x, c_{sy} and c_{sx} are shown in Table 3.1, the mechanical admittance functions of lateral seen layouts in Fig. 4.1 are shown in Eqs. (4.1 - 4.6), and the admittance functions of the default and HALL-bush longitudinal layouts (respectively L_{x1} and L_{x2}) are the same as in Eqs. (4.1, 4.3), but with appropriate variable substitutions made.

$$L_{y1}(s) = \frac{K_y}{s} + c_{sy} \tag{4.1}$$

$$L_{y2}(s) = \frac{K_y}{s} + c_{sy} + b_{syp}s \tag{4.2}$$

$$L_{y3}(s) = \frac{K_y}{s} + \left(\frac{s}{k_{sy}} + \frac{1}{c_{sy}}\right)^{-1} \tag{4.3}$$

$$L_{y4}(s) = \frac{K_y}{s} + \left(\frac{s}{k_{sy}} + \frac{1}{c_{sy}}\right)^{-1} + b_{syp}s \tag{4.4}$$

$$L_{y5}(s) = \frac{K_y}{s} + \left(\frac{s}{k_{sy}} + \frac{1}{c_{sy}} + \frac{1}{b_{sy}s}\right)^{-1} \tag{4.5}$$

$$L_{y6}(s) = \frac{K_y}{s} + \left(\frac{s}{k_{sy}} + \frac{1}{c_{sy}} + \frac{1}{b_{sy}s}\right)^{-1} + b_{syp}s \tag{4.6}$$

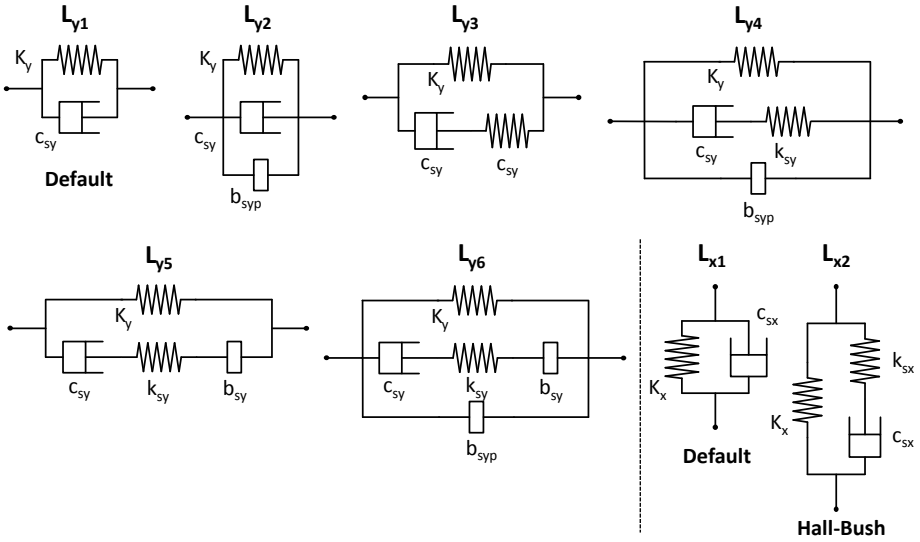

Fig. 4.1 The six lateral $L_{yi}(s)$ (investigated in [101] and [103]) and two $L_{xj}(s)$ (longitudinal) candidate layouts. L_{x2} denotes the HALL-bush structure which includes a static stiffness K_x and dynamic stiffness k_{sx}.

4.2.2 Track data analysis

Figures 4.2(a) and (b) show the PSDs of the lateral displacement of all three track inputs for a vehicle velocity of 31 ms^{-1}. The PSDs were produced using Fourier analysis of each of the track inputs. Note that the nominal vehicle velocity of 31 ms^{-1} (111.6 kph) roughly equates to the rated speed of Track110 (110 kph). The curves in Figures 4.2(a) and (b) have been scaled respectively so that frequencies above 8 Hz and 50 Hz are ignored. This scaling has been performed to assess how each track's frequency behaviour varies. Note that the frequency axis limits of 0 - 8 Hz remain constant, a low-pass filter has been used to reduce noise in all curves, and that the Random Track curves have been scaled down for ease of viewing.

It is clear that there is a peak at low frequencies then a decay towards higher frequencies for all three cases. However, in both weighting cases, for the Random Track there is far more of a focus of frequencies below 0.5 Hz and above 2.5 Hz, with significantly lower PSD magnitude for frequencies between these values when compared with Track110 and Track160. This discrepancy between the two tracks is noted, nevertheless it is decided that the analysis will continue to use both track types, as it is significantly more computationally efficient to use the Random Track rather than Track110 or Track160. The fact that this discrepancy in PSD magnitude occurs at around the first lateral rigid body mode (1 Hz) must be noted when assessing the Random Track results.

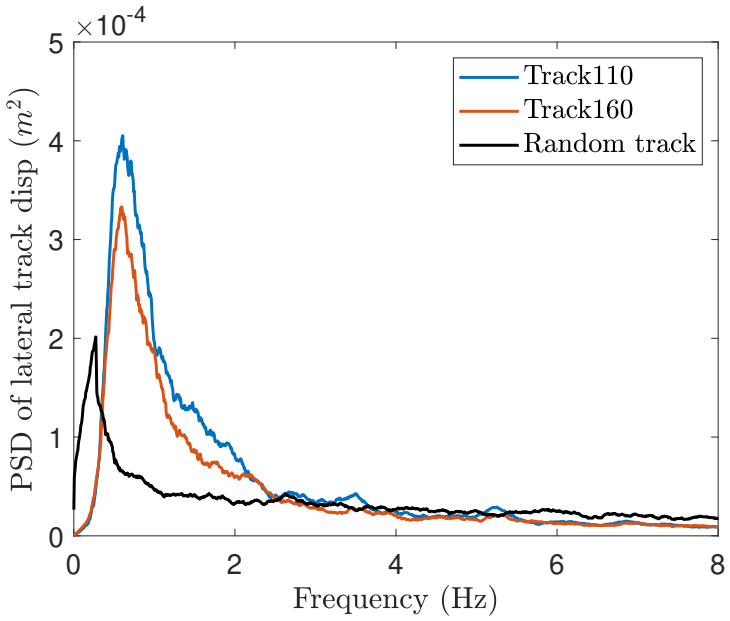

(a) Weighted 1 - 8 Hz

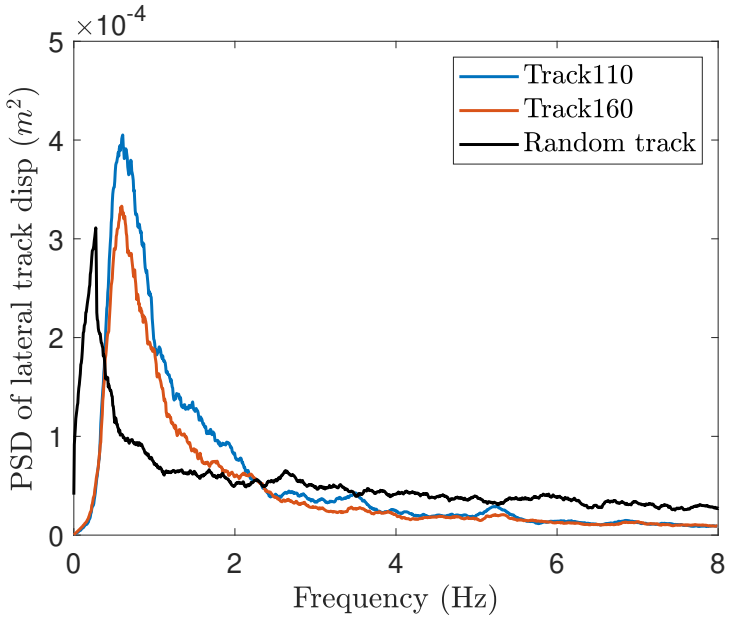

(b) Weighted 1 - 50 Hz

Fig. 4.2 PSD of lateral track displacement for the three track types, weighted respectively for the range 1 - 8 Hz, and 1 - 50 Hz, post noise reduction.

4.2.3 Optimisation results

Optimisations of parameters within each $L_{yi}(s)$ layout can now be performed with the aim of minimising J_{5y}, RMS carbody acceleration introduced in Chapter 3, Section 3.2.1. Note that no longitudinal suspension optimisation is performed at this stage. A SIMULINK® model with the Track110 and Track160 timeseries as inputs is used to calculate J_{5y}, and the static lateral stiffness, K_y is fixed at its nominal value given in Table 3.1, with each of the other $L_{yi}(s)$ network parameters being optimised over, with a non-negative constraint. When using the Random Track data as inputs for the optimisations, Eq. (3.24) from Chapter 3 is used to calculate the resulting RMS carbody acceleration. Note that a SIMULINK® model is not required for the Random Track input. The results for the Track110, Track160 and Random Track cases are shown in Tables 4.1 - 4.3 respectively, and summarised in Fig. 4.3. The default operational vehicle velocity, V_{op}, is used for all three track input cases. The default layout of the lateral suspension is that of L_{y1}, and therefore the first rows in Tables 4.1 - 4.3 represent baseline acceleration values, while the third column represents percentage improvements from these values. The optimisation procedure uses the Patternsearch function in MATLAB® and then subsequently the Fminsearch function to home in on more accurate parameter values.

As railway vehicles pass over tracks with many different rated speeds, a cost function, P, has been created to represent the dimensionless reduction in the average J_{5y} for both Track110 and Track160,

$$P = \frac{1}{2}\left(\frac{J_{5y,110}}{J_{5y,110,L_{y1}}} + \frac{J_{5y,160}}{J_{5y,160,L_{y1}}}\right). \tag{4.7}$$

The L_{y1} symbol here represents the acceleration corresponding to the default layout. The results for this case are shown in Tables 4.4 and 4.5, which respectively show each layout's acceleration reductions and corresponding optimised parameters values. When comparing Tables 4.1 and 4.2 with Table 4.4, it can be concluded that the J_{5y} values in Table 4.4 are extremely similar to those previously determined for the Track110 and Track160 cases. For this reason, the rest of the analysis in this chapter will focus on the raw J_{5y} values.

It is clear that configurations L_{y2}, L_{y4} and L_{y6} provide an increasingly improved J_{5y} reduction, which is most likely due to the presence of a single parallel inerter in each. Track160, having a higher related velocity than Track110, is comprised of less extensive lateral irregularities and hence produces a lower J_{5y}. This phenomenon is visible in Figure 4.3, and extrapolating, one can claim that the Random Track theoretically describes a track with a velocity rating above 160 kph. However, it can be concluded that whilst analysis using Random Track data results in reduced simulation time and the trends in the RMS acceleration reduction are in general the same as for

the real track data, there are significant differences in the their PSD curves, and there is ambiguity of the Random Track's *rated* velocity. Real track data is therefore used for the rest of the analysis in this chapter, and thesis.

From Tables 4.1 and 4.2 it can be seen that the series spring within configuration L_{y3} has no compliance, resulting in the RMS acceleration remaining at its default, L_{y1} value. A similar phenomenon occurs for configuration L_{y5} and the inclusion of a series inerter does little to reduce the RMS acceleration. This is due to the fact that the newly introduced break frequency remains high when compared with the carbody oscillation frequencies. Improvements in J_{5y} of 0% and 1.3% for configurations L_{y3} and L_{y5} respectively are contrasted with those for L_{y2}, L_{y4} and L_{y6}, who's respective values are far larger, at 8.2%, 31.4% and 45.7%. Track160, having a higher rated velocity than Track110, is comprised of less extensive lateral irregularities and hence produces a lower J_{5y} but with similar trends to Track160; see Fig. 4.3.

To provide some context to this analysis, the carbody lateral RMS acceleration values presented in Tables 4.1 - 4.3 are all below 0.2 ms^{-2}, therefore according to the continuous comfort indices proposed in [107], the ride comfort lies in the *very comfortable* region. Note that this assumes that the vertical RMS acceleration (J_{5z}) is also less than 0.2 ms^{-2} (J_{5y}, J_{5z} < 0.2 ms^{-2} = very comfortable; 0.2 ms^{-2} < J_{5y}, J_{5z} < 0.3 ms^{-2} = comfortable; 0.3 ms^{-2} < J_{5y}, J_{5z} < 0.4 ms^{-2} = medium; J_{5y}, J_{5z} > 0.4 ms^{-2} = less comfortable). The primary concern in the analysis, however, is the relative improvements in RMS J_{5y} rather than the absolute values.

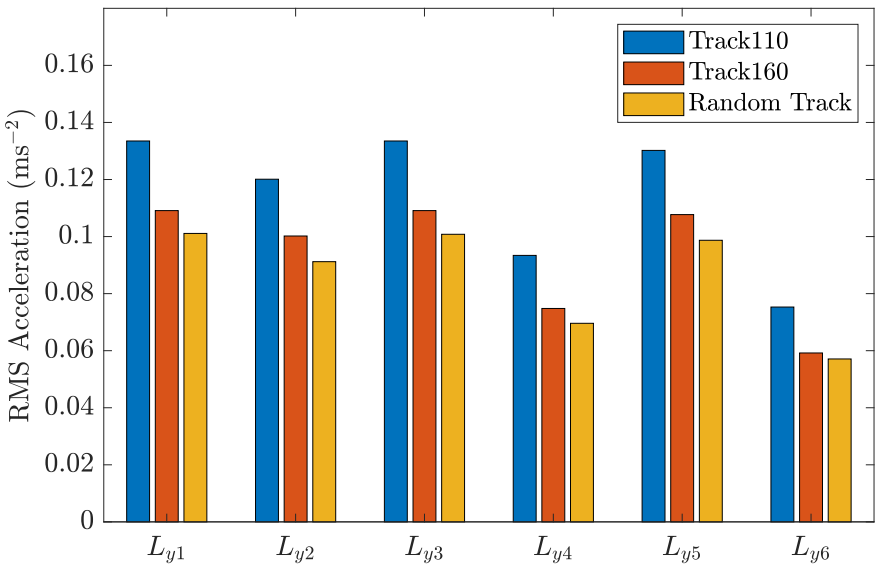

Fig. 4.3 A comparison chart representing the optimised RMS carbody acceleration values for Track110, Track160, and Random Track at a vehicle operation speed of V_{op}.

Lay-out	J_{5y} min (ms^{-2})	J_{5y} impr (%)	Parameter values k_{sy} (Nm^{-1}), c_{sy} (Nsm^{-1}), $b_{sy/syp}$ (kg)			
L_{y1}	0.1335	-		$c_{sy} = 1.51\times10^4$		
L_{y2}	0.1201	10.0		$c_{sy} = 1.37\times10^4$		$b_{syp} = 5.03\times10^2$
L_{y3}	0.1335	0.0	$k_{sy} = \infty$	$c_{sy} = 1.51\times10^4$		
L_{y4}	0.0934	30.0	$k_{sy} = 4.24\times10^5$	$c_{sy} = 3.82\times10^4$		$b_{syp} = 1.13\times10^3$
L_{y5}	0.1302	2.5	$k_{sy} = \infty$	$c_{sy} = 1.54\times10^4$	$b_{sy} = 8.93\times10^3$	
L_{y6}	0.0753	43.6	$k_{sy} = 3.40\times10^5$	$c_{sy} = 6.02\times10^4$	$b_{sy} = 7.70\times10^3$	$b_{syp} = 1.16\times10^3$

Table 4.1 Results of the two-axle railway vehicle (Fig. 3.2) optimisations, to reduce RMS carbody acceleration, showing J_{5y} improvements and optimum parameters, using a lateral track displacement input of Track110.

Lay-out	J_{5y} min (ms^{-2})	J_{5y} impr (%)	Parameter values k_{sy} (Nm^{-1}), c_{sy} (Nsm^{-1}), $b_{sy/syp}$ (kg)			
L_{y1}	0.1091	-		$c_{sy} = 1.51\times10^4$		
L_{y2}	0.1002	8.2		$c_{sy} = 1.42\times10^4$		$b_{syp} = 4.53\times10^2$
L_{y3}	0.1091	0.0	$k_{sy} = \infty$	$c_{sy} = 1.51\times10^4$		
L_{y4}	0.0748	31.4	$k_{sy} = 4.28\times10^5$	$c_{sy} = 4.20\times10^4$		$b_{syp} = 1.13\times10^3$
L_{y5}	0.1077	1.3	$k_{sy} = \infty$	$c_{sy} = 1.56\times10^4$	$b_{sy} = 1.27\times10^4$	
L_{y6}	0.0592	45.7	$k_{sy} = 2.92\times10^5$	$c_{sy} = 5.03\times10^4$	$b_{sy} = 6.42\times10^3$	$b_{syp} = 1.03\times10^3$

Table 4.2 Results of the two-axle railway vehicle (Fig. 3.2) optimisations, to reduce RMS carbody acceleration, showing J_{5y} improvements and optimum parameters, using a lateral track displacement input of Track160.

Lay-out	J_{5y} min (ms^{-2})	J_{5y} impr (%)	Parameter values k_{sy} (Nm^{-1}), c_{sy} (Nsm^{-1}), $b_{sy/syp}$ (kg)			
L_{y1}	0.1011	-		$c_{sy} = 1.44\times10^4$		
L_{y2}	0.0912	9.8		$c_{sy} = 1.32\times10^4$		$b_{syp} = 4.80\times10^2$
L_{y3}	0.1008	0.3	$k_{sy} = \infty$	$c_{sy} = 1.43\times10^4$		
L_{y4}	0.0696	31.2	$k_{sy} = 4.13\times10^5$	$c_{sy} = 4.08\times10^4$		$b_{syp} = 1.12\times10^3$
L_{y5}	0.0987	2.4	$k_{sy} = \infty$	$c_{sy} = 1.48\times10^4$	$b_{sy} = 9.84\times10^3$	
L_{y6}	0.0571	43.5	$k_{sy} = 2.92\times10^5$	$c_{sy} = 5.03\times10^4$	$b_{sy} = 6.50\times10^3$	$b_{syp} = 1.02\times10^3$

Table 4.3 Results of the two-axle railway vehicle (Fig. 3.2) optimisations, to reduce RMS carbody acceleration, showing J_{5y} improvements and optimum parameters, using the Random Track input.

Layout	P	$J_{5y,110}$ impr (ms^{-2})	$J_{5y,160}$ impr (ms^{-2})
L_{y1}	1.00	0.1335	0.1091
L_{y2}	0.91	0.1202	0.1002
L_{y3}	1.00	0.1335	0.1091
L_{y4}	0.69	0.0934	0.0748
L_{y5}	0.98	0.1303	0.1077
L_{y6}	0.55	0.0754	0.0593

Table 4.4 Optimisation results for reducing RMS carbody acceleration of the two-axle model (Fig. 3.2) using the real track data cost function, P (J_{5y} reductions).

Layout	Parameter values (Nm^{-1}, Nsm^{-1}, kg)			
L_{y1}		$c_{sy} = 1.51\times10^4$		
L_{y2}		$c_{sy} = 1.40\times10^4$		$b_{syp} = 4.77\times10^2$
L_{y3}	$k_{sy} = \infty$	$c_{sy} = 1.52\times10^4$		
L_{y4}	$k_{sy} = 4.20\times10^5$	$c_{sy} = 3.93\times10^4$		$b_{syp} = 1.13\times10^3$
L_{y5}	$k_{sy} = \infty$	$c_{sy} = 1.56\times10^4$	$b_{sy} = 1.06\times10^4$	
L_{y6}	$k_{sy} = 3.15\times10^5$	$c_{sy} = 5.41\times10^4$	$b_{sy} = 6.67\times10^3$	$b_{syp} = 1.06\times10^3$

Table 4.5 Optimisation results for reducing RMS carbody acceleration of the two-axle model (Fig. 3.2) using the real track data cost function, P (optimised parameter values).

4.2.4 Continuous velocity assessment

Having established three beneficial lateral suspension configurations at the vehicle's rated velocity of 31 ms^{-1}, and concluded that real track data is best suited for the rest of the analysis in this thesis, the following analysis determines the extent to which the carbody's acceleration changes over a range of vehicle speeds. To this end, Fig. 4.4 shows how the RMS carbody acceleration varies with an increase in vehicle velocity for the six lateral suspension configurations and for Track110 and Track160.

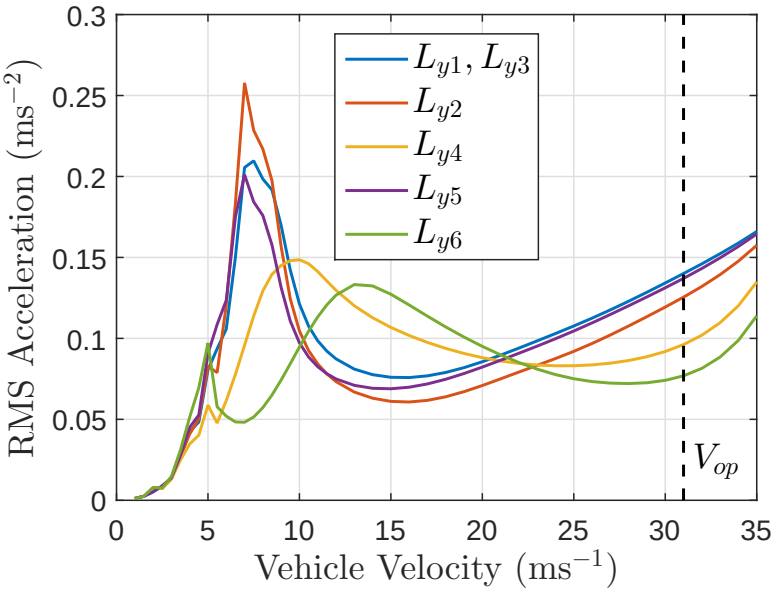

(a) Track110

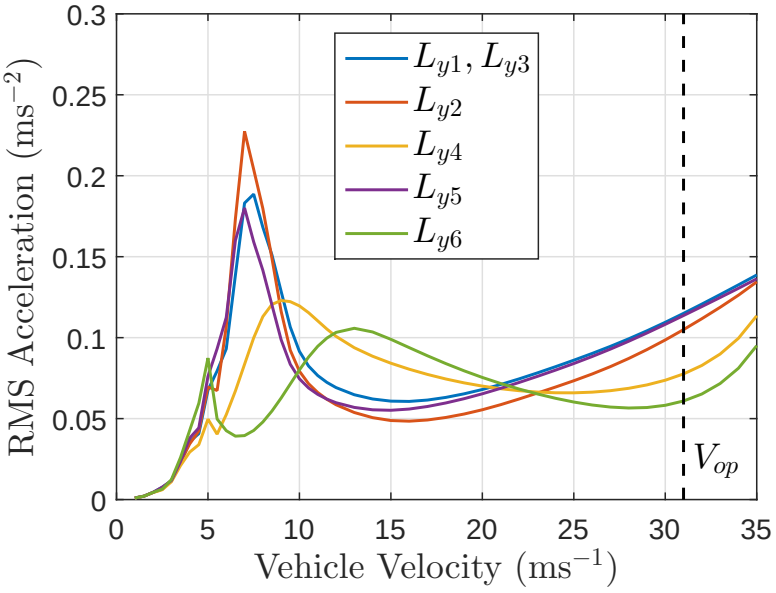

(b) Track160

Fig. 4.4 RMS carbody acceleration vs vehicle velocity for both sets of real track data, with the vehicle operation velocity, V_{op}, highlighted.

No further optimisations take places in this analysis, hence all the optimised suspension parameters (at V_{op}) are used to assess the performance at other speeds. This is because, in reality, besides active or semi-active nonlinear suspensions who's

parameters may be vehicle velocity dependent, parameters of passive suspensions such as the configurations suggested here remain constant over the entire range of speeds. The vertical dashed line indicates the optimisation and rated velocity, V_{op}, and the RMS accelerations at this speed correspond with the values shown in Fig. 4.3. As discussed in Section 4.2.3, layout L_{y3} optimises to that of L_{y1}; therefore only one *base case* line is plotted (in blue) in Figs. 4.4(a) and (b) for clarity.

Both plots follow the same general trend. There exists for L_{y1}, L_{y2} and L_{y5} a peak at around 7.5 ms^{-1}, a minima at roughly 15 ms^{-1} then a steady increase as the velocity increases further. Curves simulated using suspension's L_{y4} and L_{y6} however show maxima of lower magnitudes and shifted to higher velocities, yet at the optimisation velocity the RMS acceleration is significantly decreased (see Fig. 4.4). The different nature of these sets of curves suggests a fundamentally different frequency response for configurations L_{y4} and L_{y6}. For both plots, L_{y6} in general is the most optimum configuration. Only in the intermediate region between 12 ms^{-1} and 21 ms^{-1} is L_{y6} not only sub-optimum, but the most detrimental to the RMS acceleration, however in reality vehicles will spend little time at this velocity. It is worth mentioning that the L_{y4} and L_{y6} cases exhibit more rapid increases RMS acceleration for speeds above V_{op}, however as the vehicle is not designed to travel above this speed, this is not a concern. It is anticipated that for higher speed vehicles, as the optimisation velocity, V_{op}, will be higher, a similar trend of optimisation results at V_{op} will occur.

Confidence can be gained in this passenger comfort assessment and optimisation as the general trends observed are similar to that seen in the previous work of [102]. Note that each RMS acceleration on Figs. 4.4(a) and (b) is generated by a vehicle travelling over a 5 km length of track, therefore the analysis is steady state. In reality however as a vehicle accelerates forwards, it will not be subject to the full extent of lateral irregularities at each speed. The carbody acceleration vs vehicle velocity curves will therefore be semi-transient in nature, and may differ slightly from Fig. 4.4.

4.3 Trackwear and passenger comfort trade-off analysis

In Chapter 3, Figs. 3.4(e) and (f) help to demonstrate how T_γ grows nonlinearly with increasing PYS. This is due to its squared creepage terms which can be interpreted from Eqs. (3.33, 3.34) in Chapter 3, Section 3.2.2. T_γ is found to be highly dependent on the PYS, due to increasing K_x highly correlating with an increasing steady state curving displacement, and hence larger longitudinal creep forces. Note that in this analysis, the PYS is modelled as solely the static longitudinal stiffness, however in reality it is made up also of the longitudinal shear stiffness component of the primary shear springs.

Due to T_γ's high dependency on K_x, simply including more complicated and optimised inerter-based structures in the lateral suspension does not directly reduce T_γ, although in most cases the passenger comfort is significantly improved. This is captured in the trade-off plots shown in Figs. 4.5(a) and (b), which consider optimisations for increasing passenger comfort using a range of PYS values for both Track110 (Fig. 4.5(a)) and Track160 (Fig. 4.5(b)) inputs.

Each plot in Fig. 4.5 is generated as follows: firstly, optimisations for increasing passenger comfort take place using the baseline suspension, layout L_{y1} at a PYS (K_x) value of $1{\times}10^6$ Nm^{-1}. K_x is increased in steps of $0.5{\times}10^6$ Nm^{-1} to $4.5{\times}10^6$ Nm^{-1} to produce the black solid line. To aid comparison across the layouts, the points on each curve corresponding to a fixed K_x value are joined by dotted lines; these are very near horizontal, highlighting that the lateral suspension improvements do not impact on the trackwear. The lowest dotted line is for $K_x = 1{\times}10^6$ Nm^{-1} and the highest for $K_x = 4.5{\times}10^6$ Nm^{-1}, with increments of $0.5{\times}10^6$ Nm^{-1} in between. Note that for this set of optimisations, the damper in L_{x1}, c_{sx}, is fixed to its nominal value shown in Table 3.1. This is due to the performance being insensitive to its value within a large range, and also its variation forms a subset of the HALL-bush optimisation which is discussed later on in this section.

The solid black curve, representing the default lateral suspension (L_{y1}), shows the default trade-off between straight running and curving performance, as increasing K_x inherently increases T_γ yet allows the RMS acceleration to reduce, and vice versa. It is found that when the three beneficial configurations identified in Section 4.2.3 are employed, and the system re-optimised, this trade-off, although still in existence, is improved as the carbody accelerations are reduced for any given T_γ. Consider the Track110 case; it can be seen that for a given layout it is not possible to improve both T_γ and RMS acceleration. However through the use of a more complex layout this can be achieved; for example, at the point on the default L_{y1} curve in Fig. 4.5(a), where $K_x = 2{\times}10^6$ Nm^{-1}, indicated by the red circle, RMS acceleration = 0.112 ms^{-2} and $T_\gamma = 13$ N. If instead the L_{y6} layout is used, and the PYS reduced to $1{\times}10^6$ Nm^{-1} (see the green circle), values of 0.075 ms^{-2} and 3.2 N can be achieved, respectively providing improvements of 33% and 75%. Similar benefits can be seen with the other inerter-based layouts, and it can be concluded therefore that passenger comfort can be improved and trackwear reduced concurrently by employing inerter-based configurations in the lateral suspension, effectively permitting a reduction in PYS. Note the same trends are exhibited with the Track160 analysis, yet as expected with a track input consisting of less extensive lateral irregularities, the carbody accelerations are lower in magnitude.

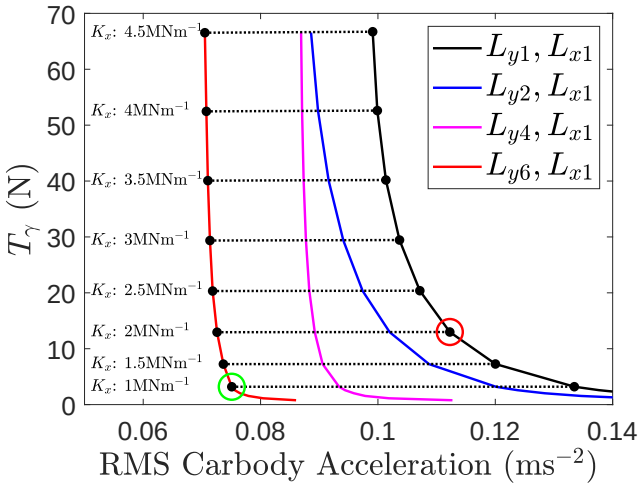

(a) Track110

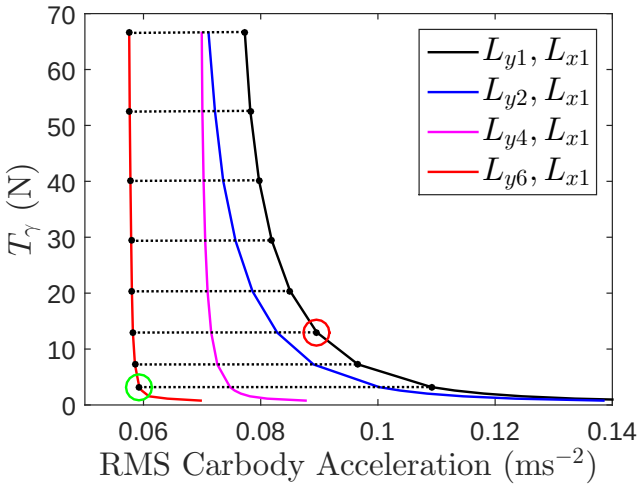

(b) Track160

Fig. 4.5 Trade-off plots showing T_γ vs optimised RMS carbody acceleration for values of K_x varying from 0.5×10^6 Nm^{-1} to 4.5×10^6 Nm^{-1}, with the L_{y1}, L_{y2}, L_{y4} and L_{y6} lateral suspension configurations, and the default L_{x1} longitudinal configuration (the coloured circles indicate example improvements for both trackwear and passenger comfort). K_x step-sizes of 0.1×10^6 Nm^{-1} below 1×10^6 Nm^{-1}, and 0.5×10^6 Nm^{-1} above 1×10^6 Nm^{-1} are used to create these curves, enabling a more comprehensive analysis of simulations with lower K_x values.

Whilst T_γ depends on both the longitudinal and lateral contact patch forces, as well as their respective creepages, it is useful to observe how the these forces vary individually with time under curving conditions, and how they are affected by both changes in the optimised lateral suspension and K_x. The following discussion is therefore devoted to the analysis of lateral and longitudinal forces during curving. It should be noted that longitudinal force is highly dependent on conicity, as well as PYS. However, in this section the conicity is kept constant at 0.2 to enable a full analysis of how each force varies with K_x and the lateral suspension configuration in question.

The plots seen in Fig. 4.6 show how the longitudinal and lateral creep forces at the front left and rear left wheel vary under curving conditions, which are described in Section 3.2.2. One can see the initial two second period of straight track (zero force) followed by a one second transition to curing (steady increase in force magnitude), six seconds of constant curvature (constant force with some overshoot and oscillatory behaviour), one second of re-transition and then a return to straight track. The solid black line denotes the default L_1 lateral suspension but with a K_x of $2{\times}10^6$ Nm^{-1} (lateral suspension optimised for reduced passenger comfort at $K_x = 2{\times}10^6$), the magenta line denotes the same lateral suspension but with a K_x reduced to $1{\times}10^6$ Nm^{-1} (*but* with the lateral suspension optimised for reduced passenger comfort at $K_x = 2{\times}10^6$ Nm^{-1}), and the dashed black line (almost identical to the magenta line) details a vehicle with lateral suspension L_4 and a K_x of $1{\times}10^6$ Nm^{-1} (lateral suspension optimised for reduced passenger comfort at $K_x = 1{\times}10^6$ Nm^{-1}). The above suspensions have been chosen to effectively re-define L_1 with $K_x = 2{\times}10^6$ Nm^{-1} as the default suspension (red circle in Fig. 4.5). It is useful to read these figures in conjunction with Fig. 4.5(a). Note that the axes of the plots have different scales.

It is clear from the outset that the general trend observed with these forces is broadly in the expected ballpark for a vehicle of this nature; namely that the longitudinal forces are greater in magnitude, and less oscillatory than the lateral forces. The longitudinal forces' dependency on K_x is highlighted by the fact that as K_x is halved, the longitudinal force roughly halves also. Also, as K_x halves, both forces become more oscillatory. This is expected as in general a vehicle's stability decreases with a reduced PYS due to the higher propensity for the wheelset to yaw. It is positive to observe that when the L_4 suspension is introduced, the forces produced are no more oscillatory and are effectively the same as the L_1 suspension. Section 4.2 shows that the vehicle with an L_4 suspension, when encountering a straight rough track and the associated frequencies of track disturbance, shows a reduction in RMS carbody acceleration. The fact that there is limited to no reduction in both longitudinal and lateral forces when comparing L_4 to L_1 in Fig. 4.6 is consequently deemed unproblematic.

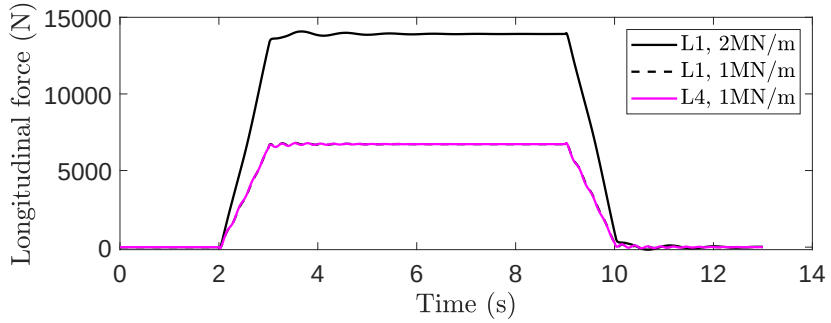

(a) Front wheelset, left wheel

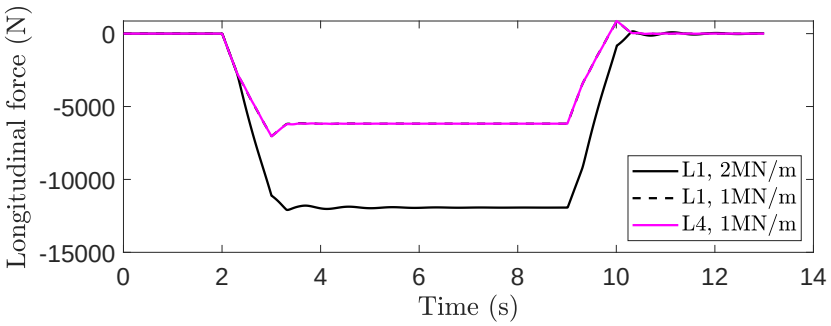

(b) Rear wheelset, left wheel

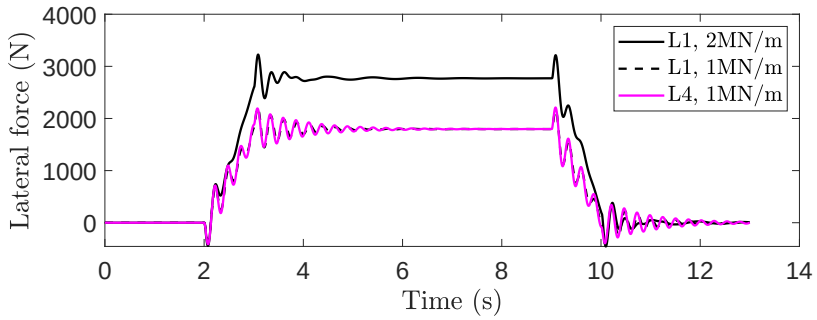

(c) Front wheelset, left wheel

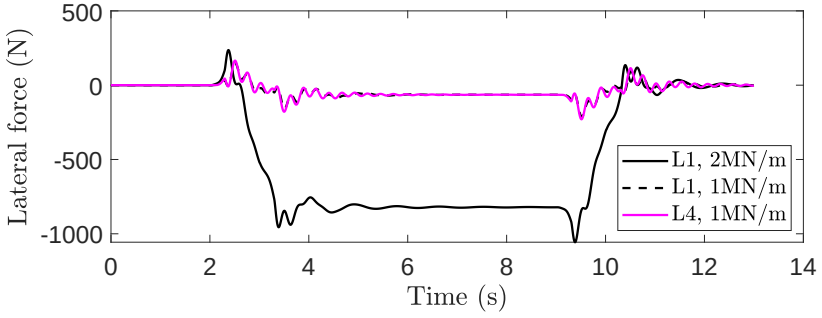

(d) Rear wheelset, left wheel

Fig. 4.6 These plots show the variation in the longitudinal and lateral forces at the front and rear wheelsets (left wheels) when the vehicle is subject to curving conditions (see Section 3.2.2). A vehicle with the default suspension optimised at a K_x of $2{\times}10^6$ (black), is compared to a vehicle with the same suspension parameters, but with a K_x now of $1{\times}10^6$ (black dashed), and an optimised L4 layout with again a K_x value of $1{\times}10^6$. Note how the axes' scales differ.

Returning to the trade-off between passenger comfort and trackwear, now consider including the HALL-bush device as the longitudinal suspension layout, L_{x2} in Fig. 4.1, rather than the default L_{x1} layout. The HALL-bush structure (previously discussed in Section 2.2.1) is widely used in the railway industry [9] and consists of a high stiffness dynamic spring (k_{sx}) in series with a damper, and the lower parallel static yaw stiffness (K_x), the PYS. This optimisable series stiffness allows for an improved passenger comfort over the conventional L_{x1} layout. This is shown in Fig. 4.7 for the case where the lateral suspension considered is L_{y1}. Note here that for the HALL-bush case, a more general approach is taken, with k_{sx} and c_{sx} being optimised in addition to the lateral suspension parameters. Here the solid black line is repeated, to aid comparison, and the dashed line shows the improvement in carbody acceleration achievable using the HALL-bush. Again, altering the PYS only affects the trackwear. As an example of the improvements that are observed here, re-evaluating the changes in trackwear and passenger comfort from the red to green circle in Fig. 4.7(a), improvements in passenger comfort and trackwear of 21% and 75% respectively are identified with the inclusion of the HALL-bush.

Finally, Fig. 4.8 extends the analysis including the longitudinal HALL-bush to lateral layouts L_{y2} and L_{y6}. Layout L_{y4} is not shown as its curve is found to converge quickly to that of L_{y2} with increasing values of K_x. A passenger comfort improvement of 40% can be achieved when compared to the default non HALL-bush and L_{y1} set-up (solid black line). Another important consideration is the extent to which inerter-based lateral suspension layouts plus an optimised HALL-bush improve passenger comfort over the use of just the HALL-bush structure and L_{y1}. Comparing the green circles in Figs. 4.7(a) and 4.8(a), a passenger comfort improvement of 25% is achievable in this case.

A summarising example of the benefits that inerter-based lateral suspensions can bring to a two-axle railway vehicle assessed on Track110 is detailed as follows: combined with a PYS, or K_x, reduction of 50% (from $2{\times}10^6$ Nm^{-1} to $1{\times}10^6$ Nm^{-1}, resulting in a T_γ improvement of 75%) the implementation of an L_{y2} lateral layout yields a passenger comfort improvement of 35% compared to the default L_{x1} layout, and 18% when compared with the optimum default lateral layout alongside a longitudinal HALL-bush setup. These percentage improvements can be increased to 40% and 25% respectively when the more complex L_{y6} lateral layout is used.

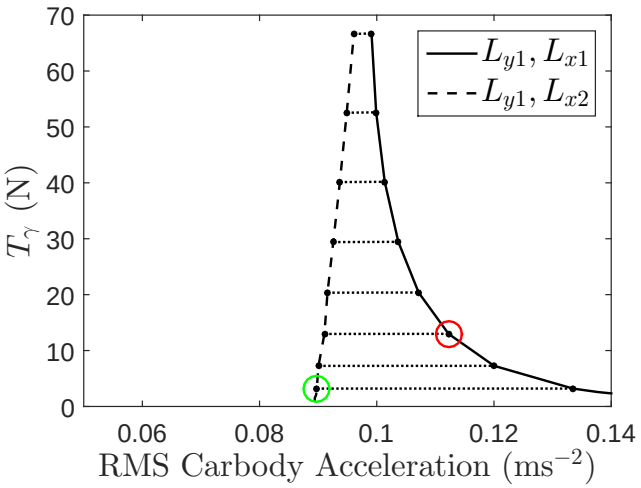

(a) Track110

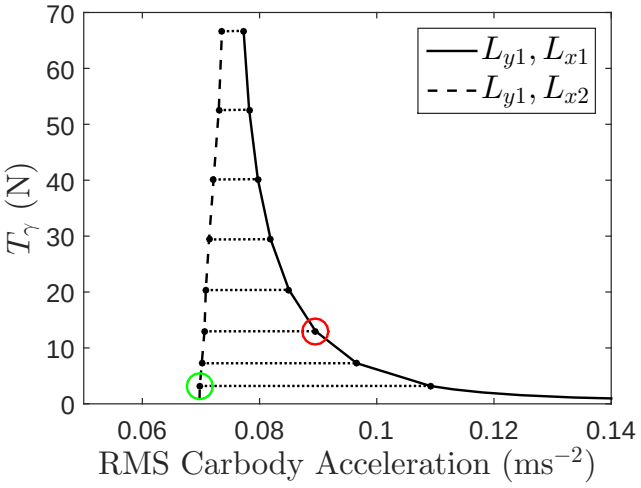

(b) Track160

Fig. 4.7 Trade-off plots showing T_γ vs optimised RMS carbody acceleration for values of K_x varying from $0.5{\times}10^6$ Nm^{-1} to $4.5{\times}10^6$ Nm^{-1}, with the optimised default L_{y1} lateral and both the default L_{x1} and HALL-bush L_{x2} longitudinal suspension configurations (the coloured circles indicate example improvements for both trackwear and passenger comfort). K_x step-sizes of $0.1{\times}10^6$ Nm^{-1} below $1{\times}10^6$ Nm^{-1}, and $0.5{\times}10^6$ Nm^{-1} above $1{\times}10^6$ Nm^{-1} are used to create these curves, enabling a more comprehensive analysis of simulations with lower K_x values.

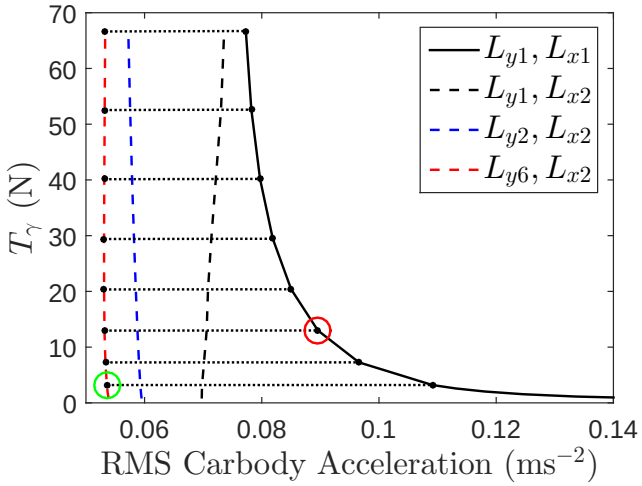

(a) Track110

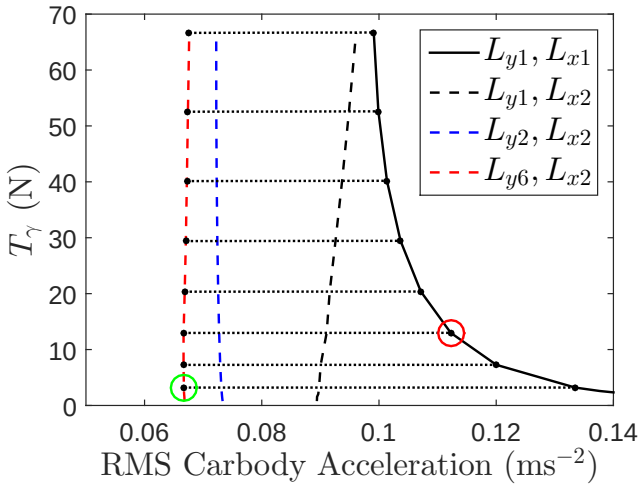

(b) Track160

Fig. 4.8 Trade-off plots showing T_γ vs optimised RMS carbody acceleration for values of K_x varying from 0.5×10^6 Nm^{-1} to 4.5×10^6 Nm^{-1}, comparing the fully optimised L_{y2} and L_{y6} configurations combined with L_{x2} combinations with the original optimised default L_{y1} and L_{x1} combination (the coloured circles indicate example trackwear and passenger comfort improvements). K_x step-sizes of 0.1×10^6 Nm^{-1} below 1×10^6 Nm^{-1}, and 0.5×10^6 Nm^{-1} above 1×10^6 Nm^{-1} are used to create these curves, enabling a more comprehensive analysis of simulations with lower K_x values.

4.3.1 Optimised suspension parameter values

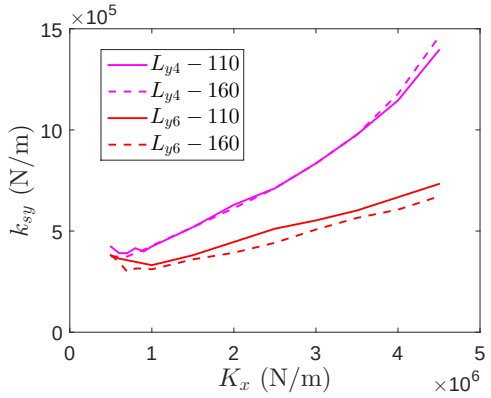

(a) Optimised lateral stiffness parameters vs K_x, *without* HALL-bush optimisations.

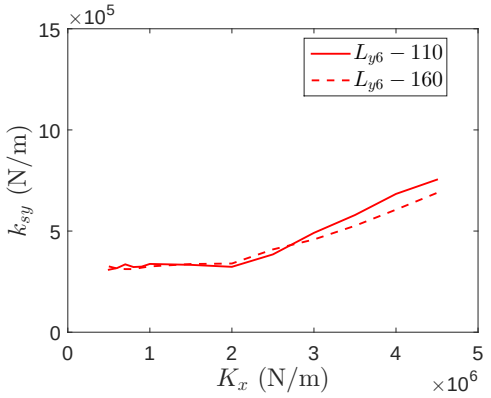

(b) Optimised lateral stiffness parameters vs K_x, *with* HALL-bush optimisations.

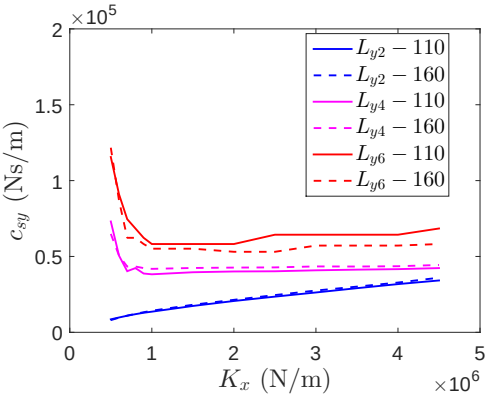

(c) Optimised lateral damping parameters vs K_x, *without* HALL-bush optimisations.

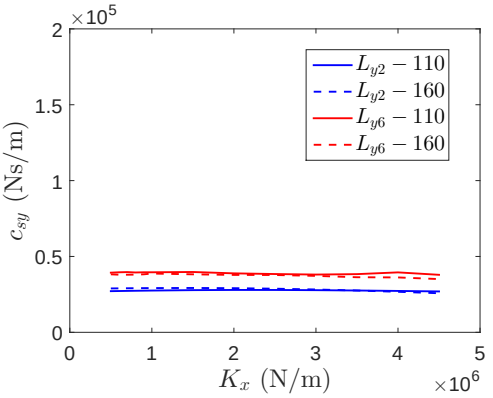

(d) Optimised lateral damping parameters vs K_x, *with* HALL-bush optimisations.

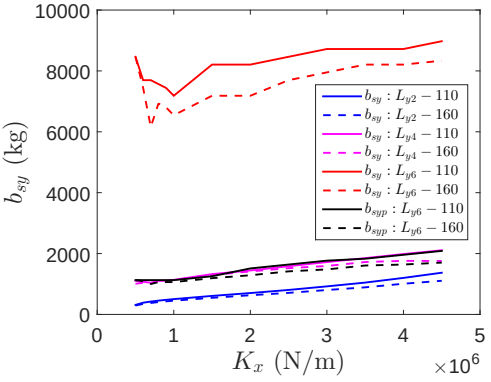

(e) Optimised lateral inertance parameters vs K_x, *without* HALL-bush optimisations.

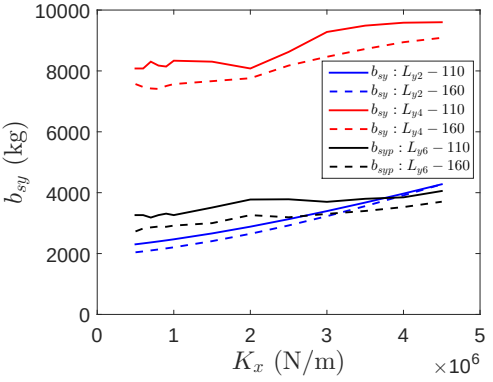

(f) Optimised lateral inertance parameters vs K_x, *with* HALL-bush optimisations.

Fig. 4.9 How optimised parameters of lateral suspension components vary with PYS, for varying suspension layouts, with and without a HALL-bush structure in the longitudinal suspension, and for inputs of both Track110 and Track160 (110 and 160 here). Note that when the default longitudinal suspension, L_{x1}, is used (see Fig. 4.1), c_{sx} is fixed at $4{\times}10^3$ Nsm^{-1}.

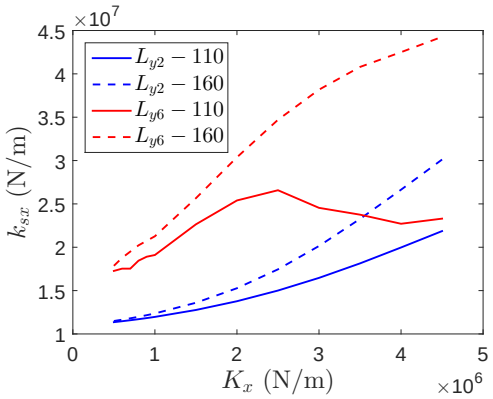

(a) Optimised HALL-bush dynamic stiffness values.

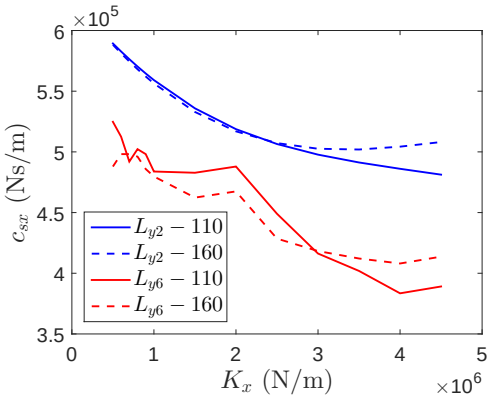

(b) Optimised HALL-bush damping values.

Fig. 4.10 How optimised parameters longitudinal HALL-bush suspension components vary with PYS, for varying suspension layouts for inputs of both Track110 and Track160.

Analysing how the optimum suspension parameter values vary with PYS has the potential to yield look-up plots where appropriate parameters may be chosen according to the amount of trackwear and passenger comfort permissible. To this end, plots of how the suspension parameter values vary with PYS can be found in Figs. 4.9 and 4.10. Note that the graphs each contain different numbers of curve, according to the layout complexity, and whether or not HALL-bush optimisations have taken place as well. The left column of graphs are *without* HALL-bush optimisations, and the right column of graphs are *with* HALL-bush optimisations (layout L_{y4} is ignored in the latter case, just in the same way as it was ignored in Fig. 4.8).

The non-smooth nature of these plots is most likely due to the patternsearch optimisation homing in on local minima for certain specific points. All Track110 curves follow similar patterns to their Track160 counterparts, and vice-versa, apart from one exception, the dynamic HALL-bush spring stiffness when combined with a L_{y6} longitudinal layout. It is also noticed that as the complexity of the lateral suspension layout increases, the more scattered each parameter curve becomes.

4.3.2 Sensitivity analysis using half-creep contact patch

Up to this point, we have assumed a coefficient of friction value of $\mu = 0.6$, and full-creep conditions. This can be thought of as a worst case scenario, and this section presents a sensitivity analysis on how using effectively a reduced coefficient of friction affects the passenger comfort vs ride comfort trade-off.

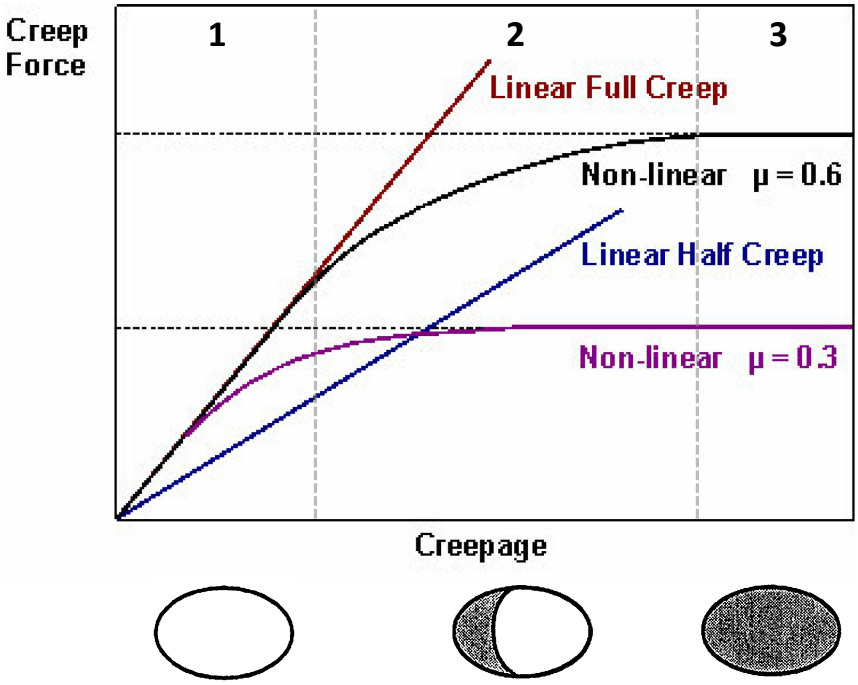

Fig. 4.11 A creep force vs creepage curve, at the wheel-rail contact patch, taken from the VAMPIRE® software handbook [106], detailing how linear approximations of nonlinear friction saturation manifest themselves. The elliptical contact patches for three creepage ranges, taken partially from [3], demonstrates how slip (shaded) and stick (white) progress with increased creepage.

Figure 4.11 shows the standard creep force vs creepage set of curves at the wheel-rail contact patch. The black and purple curves represent the true situation with friction saturation, for different values of coefficient of friction, and the the straight diagonal lines show how the creep force vs creepage relationship can be linearised. Taking $\mu = 0.6$ for example, the first segment (1) details the situation when there is no slip between the wheel and rail, in segment 2 there is partial slip and partial stick, and in segment 3 it can be observed that the creep force does not increase with increased creepage: full slip conditions, or total friction saturation. For small values of creepage, it is sufficient to utilise the initial gradient of the curves. This simplification is named linear full-creep.

It can be seen though that, for any coefficient of friction, and especially for decreasing values of coefficient of friction, when the creepage increases, the creep forces are increasingly over-estimated. It has been deemed necessary therefore, to perform a sensitivity analysis using linear half-creep. This can be thought of as using a lower coefficient of friction, however one must be cautious when referring to the coefficient of friction in this manner, as now, in the linear part of the curve, the creep forces will be underestimated. It is impossible to strike a perfect balance here when using linear creep laws.

Fig. 4.12 details the results of the sensitivity analysis, in which the default L_{y1} and the optimised L_{y2} vehicle (black and blue curves respectively in Fig. 4.5) are compared when modelled with full and half-creep laws. The horizontal dotted lines still represent identical K_x values, however it should be noted that they are not the same for the full and half-creep cases. In general, the same value of K_x produces a higher value of T_γ for the half-creep case than for the full-creep case.

These results should be read with caution as flange contact could well have been reached before some of the higher values of T_γ are achieved, however the overall conclusion is that the trade-off between passenger comfort is still successfully reduced with the use of inertance integrated suspensions when a half-creep contact law is used.

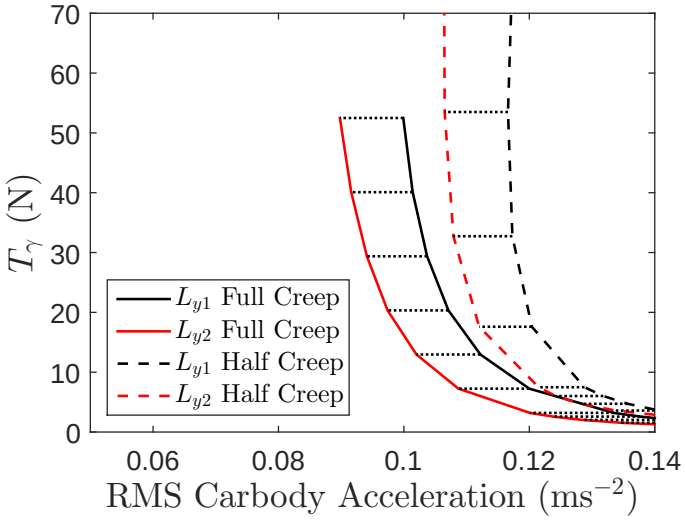

Fig. 4.12 Non HALL-bush trade-off plots showing T_γ vs optimised RMS carbody acceleration, for configurations L_{y1} and L_{y2}, comparing full-creep and half-creep linearised creepage vs creep law wheel-rail contact patch conditions. Note that the horizontal dotted lines, denoting constant values of K_x, no not line up with each other when comparing half-creep and full-creep conditions

4.4 Summary

Chapter 3's introduction of the two-axle MATLAB® vehicle model, and the techniques used to assess the overall vehicle performance, leads into the work presented in this Chapter. It is shown here that the incorporation and optimisation of inerter-based structures in the lateral suspension of railway vehicles can concurrently improve passenger comfort and decrease trackwear. It is also discovered that when these optimised lateral suspensions are used in conjunction with an optimised HALL-bush longitudinal suspension structure, the aforementioned concurrent improvement in both ride comfort and trackwear is further enhanced.

Using the two-axle MATLAB® freight vehicle model introduced in Chapter 3, which has a rated velocity of 31 ms^{-1}, five inerter-based layouts are introduced as candidate lateral suspensions. The different types of track data are assessed and it is found that the PSD of the Random Track is focused towards lower frequencies, thus Track160 and Track110 (real 5 km lengths of track rated at 160 kph and 110 kph) are used for the bulk of the analysis in this chapter. RMS lateral carbody acceleration reductions of up to 45% are found to be feasible with the most optimum, lateral inerter-based layouts, using patternsearch and fminsearch optimisation techniques, and a cost function of the carbody's RMS lateral acceleration. A continuous velocity assessment of the vehicle dynamics with all optimised devices yield that, on balance, the more complex layouts with a single parallel inerter provide the most benefit to straight running performance, although there is a wide variation in RMS acceleration over all layouts when the vehicle accelerates in the forwards direction.

Quantifying trackwear using the energy lost at the wheel-rail contact patch, T_γ, curving analysis concludes that although the use of inerters in the lateral suspension cannot directly reduce T_γ, it enables the PYS to be reduced whilst also reducing carbody accelerations under straight running conditions, which in turn allows for a reduction in T_γ. Reducing the PYS by 50% and implementing the most beneficial inerter-based layout in the lateral suspension yields a T_γ reduction of 75% and a passenger comfort improvement of 33%. Further analysis demonstrates that inerter-based configurations in the lateral suspension provide added benefits when an optimised HALL-bush configuration, is used as the longitudinal suspension. Combined with the longitudinal HALL-bush, the passenger comfort improvement rises to 40%. When comparing the most beneficial inerter-based layout to the default lateral layout, both combined with the HALL-bush structure in the longitudinal suspension, a passenger comfort improvement of 25% can be achieved. The vehicle improvements are presented in plots detailing the curving vs straight running performance *trade-off*, discussed in Section 2.1. One interesting point to note is that when the default HALL-bush is used in conjunction with the default lateral suspension structure, both straight running and curving performance improve with reduced PYS, rather than there being a trade-off

(see the semi-diagonal dotted black line in Figs. 4.7 and 4.8). This demonstrates that the HALL-bush is already an effective mechanism to combat this underlying performance predicament.

The results from this simplified model show highly promising performance benefits; however, as positive and encouraging as the results manifested from this chapter are, it should be noted that the MATLAB® model used here is a comparatively simple one in relation to those used in industry. The next step in the research detailed in this thesis, therefore, is the validation of these preliminary results. The work of Chapters 5 and 6 aims to validate the findings using the more sophisticated VAMPIRE® model detailed in Section 3.3. Chapter 5 explores the means by which a Laplace-based analytical solution technique can be applied to the mass stiffness and damping matrices of this VAMPIRE® model, and Chapter 6 combines MATLAB® and VAMPIRE® in co-simulation to perform more extensive optimisations and nonlinear validation.

Chapter 5

The location matrix method of railway vehicle simulation

In this chapter we:

- Derive the location matrix method of dynamic system simulation, which allows the integration of suspension networks with known admittance functions into certain locations of a general, complicated dynamic system.
- Enable a full Laplace domain - time domain equation of motion transformation, allowing immittance based optimisations to take place, avoiding the need to alter the base MCK equations of motion, and eliminating problems associated with large inversions of *transfer function matrices*, and algebraic loops associated with acceleration dependent inerter devices.
- Validate the method on a simple, lumped mass model, comparing with conventional time and frequency domain solutions.
- Apply the location matrix method to a more realistic VAMPIRE® railway vehicle model, and determine the extent to which this analysis is applicable.

5.1 Introduction

The results obtained from Chapter 4 significantly strengthen the case for the inerter's inclusion in railway vehicle suspensions, especially as benefits over solely an optimised HALL-bash have been identified. It was decided that the next step in this research, to strengthen the findings, should be to validate the claims of Chapter 4 on a more realistic and higher order vehicle model. The multi-body railway vehicle software, VAMPIRE®, discussed in Section 3.3.3, is a powerful simulation tool, however it is built for analysis not optimisation. With it being decided that the suspension optimisations had to be performed in MATLAB®, a method was sought that could incorporate the VAMPIRE® models into MATLAB®.

The decision was taken to tackle this problem by using mass, stiffness and damping matrices from the four-axle VAMPIRE® vehicle model, which is set up with it's default suspension, yet modelled without any lateral contribution from the trailing arm bush, and incorporate the inertance-integrated structures manually within the simulation process. It was discovered however that this technique is extremely hard to perform correctly as, from solely the matrices, it is problematic to correctly identify the coupling positions of each suspension layout and the coefficients which should be applied to each. Furthermore, the Laplace solution technique, which is highly desirable due to the interchangeable nature of the networks' admittance functions, requires extremely high order *matrix of transfer functions* inversions, which were found to be impossible in MATLAB® . This chapter introduces a solution method which aims to overcome the challenges described above.

This chapter is laid out as follows. To begin with, the location matrix simulation method is derived from a system's fundamental equation of motion. The derivation introduces fictitious states associated with the decomposition of the location matrix, with these states being re-adjoined towards the end and the overall system being transformed into time-domain, state-space form. The method is then validated using a two-mass model in MATLAB®, with all decomposition techniques providing a high degree of modelling accuracy. Finally, the extent to which this method can be applied to the four-axle VAMPIRE® railway vehicle, with simple lateral forcing inputs, and a perfectly straight track, is assessed.

The analysis undertaken in this section was reported in the following publication:

– T. D. Lewis, Y. Li, J. Z. Jiang, S. A. Neild, G. J. Tucker, S. Iwnicki, R. Goodall, M. C. Smith. Enabling the optimisation of the primary suspension with passive components for an industrial railway vehicle model. *Proceedings of the 28th International Conference on Noise and Vibration Engineering (ISMA)*, 2018.

The location matrix method detailed in this chapter was jointly derived by myself, Dr. Yuan Li from the University of Bristol, and Prof. Malcolm Smith from the University of Cambridge. Dr. Gareth Tucker from the University of Huddersfield provided the *base case* mass, stiffness and damping matrices of the VTISM four-axle vehicle ([7], and introduced in Chapter 3) used in Section 5.4, as VAMPIRE® was not available at the University of Bristol at the time.

5.2 Developing the location matrix method

This section details the derivation of a method conceived to transform the equations of motion of a generalised n-DOF dynamic system, including optimisable suspension networks, from Laplace to state-space time-domain form; namely the location matrix method of dynamic system modelling. This enables the introduction of arbitrary suspension devices to a general system, with the knowledge of their mechanical admittance functions, on which DOFs this the networks acts, and how they couple with one another. The technique serves to avoid problems associated with large Laplace matrix inversions and algebraic loops associated with inerters.

We begin by considering the equation of motion which governs a generalised dynamic system,

$$s^2 M_0 \underline{\tilde{x}} + s C_0 \underline{\tilde{x}} + K_0 \underline{\tilde{x}} = B \underline{\tilde{u}}, \tag{5.1}$$

where M_0, C_0 and K_0 denote respectively the mass, damping and stiffness matrices, $\underline{x}$ is the state matrix, and $\underline{u}$ is the input matrix, with input coefficients denoted by B. Recall that s is the Laplace variable, $\underline{\tilde{x}}$ is the Laplace transform of $\underline{x}$ and $\underline{\tilde{u}}$ the Laplace transform of $\underline{u}$. Introducing multiple copies of the same suspension network, with admittance $Y(s)$, Eq. (5.1) can be re-written as

$$s^2 M_0 \underline{\tilde{x}} + s C_0 \underline{\tilde{x}} + K_0 \underline{\tilde{x}} + s Y(s) L_m \underline{\tilde{x}} = B \underline{\tilde{u}}. \tag{5.2}$$

where L_m is the location matrix which identifies coupling locations and coefficients corresponding to the addition to the model of the $Y(s)$ suspension network (see Fig. 5.1 and Eq. (5.43) for an example of a very simple dynamic system plus the suspension network's location matrix). If there are m identical copies of the $Y(s)$ suspension network in various locations within the model, the symmetric location matrix, L_m, can be written in decomposition form

$$L_m = V V^T, \tag{5.3}$$

where $V \in \mathbb{R}^{\mathrm{n}\times\mathrm{m}}$. The i^{th} column of V, where $i = 1 \ldots m$, identifies the parameters and coupling positions which are required to correctly alter the equations of motion of the overall system when the i^{th} $Y(s)$ suspension network is included in the model. It hence follows that

$$s V_i^T \underline{\tilde{x}} = \Delta v_i, \tag{5.4}$$

where Δv_i is the relative change in velocity between the DOFs associated with the i^{th} device. The force to acceleration transfer function of the $Y(s)$ suspension network can be expressed as

$$Y'(s) = \frac{Y(s)}{s} = \frac{F_i}{\Delta a_i}, \tag{5.5}$$

in which F_i is the force exerted on the i^{th} device and Δa_i is the associated relative change in acceleration across the i^{th} device.

$Y'(s)$ must be positive-real [114]; I.E $|\psi - \phi| \leq 1$ where ψ and ϕ denote respectively the highest powers of s on the numerator and denominator of $Y'(s)$. $Y'(s)$ can be further expressed in the form

$$Y'(s) = \frac{\beta_0 s^p + \beta_1 s^{p-1} + \cdots + \beta_{p-1} s + \beta_p}{s^p + \alpha_1 s^{p-1} + \cdots + \alpha_{p-1} s + \alpha_p}. \tag{5.6}$$

The following equations show the result of the transformation of the now positive semi-definite function $Y'(s)$ into state-space form, using one example of the non-unique canonical decomposition technique.

$$Y'(s) = c_1(sI - A_1)^{-1} b_1 + d_1 \tag{5.7}$$

$$A_1 = \begin{bmatrix} 0 & 1 & 0 & \dots & 0 \\ 0 & 0 & 1 & \dots & 0 \\ \vdots & \vdots & \vdots & \ddots & \vdots \\ 0 & 0 & 0 & \dots & 1 \\ -\alpha_p & -\alpha_{p-1} & -\alpha_{p-2} & \dots & -\alpha_1 \end{bmatrix} \tag{5.8}$$

$$b_1 = \begin{bmatrix} 0_{p\times 1} \\ 1 \end{bmatrix} \tag{5.9}$$

$$c_1 = \begin{bmatrix} (\beta_p - \alpha_p\beta) & (\beta_{p-1} - \alpha_{p-1}\beta) & \dots & (\beta_2 - \alpha_2\beta) & (\beta_1 - \alpha_1\beta) \end{bmatrix} \tag{5.10}$$

$$d_1 = \beta_0 \tag{5.11}$$

It is possible to obtain L_m for large industrial systems using a reverse engineering approach and analysing a range of MCK (mass, damping and stiffness) matrices with differing suspension parameters. For example if one was to model, using an industrial piece of software, a system with and without certain suspension networks, or respectively with certain suspension networks then identically altered suspension networks, the difference in the exported stiffness matrices (or damping matrices) can be interpreted to form a location matrix. However, it is extremely difficult to interpret these location matrices and decompose L_m into the VV^T format, due to lack of algebraic information, the large numbers of DOF involved and hence a very complicated and varied coupling situation for each $Y(s)$ network. To this end, it is necessary to take a more mathematical approach to the decomposition of L_m.

It has been found that the decomposition of L_m is not unique and there exists more solutions in the form of UU^T. Equating VV^T and a discovered UU^T, it can be shown that

$$V = UQ, \tag{5.12}$$

where

$$Q = U^T V^{-T}, \tag{5.13}$$

$$QQ^T = I, \tag{5.14}$$

and hence

$$V_i^T = Q^T U_i^T. \tag{5.15}$$

Substituting $V = UQ$ into Eq. (5.4),

$$sQ^T U_i^T \underline{\tilde{x}} = \Delta v_i, \tag{5.16}$$

and multiplying by Q^{-T},

$$sU_i^T \underline{\tilde{x}} = \Delta v_{fi}, \tag{5.17}$$

a fictitious set of states is introduced, denoted by the subscript f. The following equations show how the now fictitious forces (F_{fi}) and accelerations (a_{fi}) relate to the physical system.

$$F_{fi} = QF_i. \tag{5.18}$$

Equation 5.5 can now be rewritten to include the fictitious forces and accelerations

$$Y'(s) = \frac{F_i}{\Delta a_i} = \frac{F_{fi}}{\Delta a_{fi}}. \tag{5.19}$$

The derivation of the state-space, time-domain simulation method begins with the decomposition

$$L_m = UU^T, \tag{5.20}$$

and hence adjoins fictitious states w_f, with the use of fictitious accelerations a_f. If the input to $Y'(s)$ for the i^{th} fictitious suspension network location is the change in relative fictitious accelerations of various system DOFs, ${U_i}^T \underline{x} s^2$, then r copies of the state Y' can be adjoined as follows, where ${F_{Y'}}_{fi}$ are the fictitious $Y'(s)$ suspension forces at the i^{th} fictitious suspension network location;

$$\underline{\dot{w}}_{f1} = A_1 \underline{w}_{f1} + b_1 {U_1}^T \underline{\tilde{x}} s^2, \tag{5.21}$$

$${F_{Y'}}_{f1} = c_1 \underline{w}_{f1} + d_1 {U_1}^T \underline{\tilde{x}} s^2, \tag{5.22}$$

to

$$\underline{\dot{w}}_{fr} = A_1 \underline{w}_{fr} + b_1 {U_r}^T \underline{\tilde{x}} s^2, \tag{5.23}$$

$${F_{Y'}}_{fr} = c_1 \underline{w}_{fr} + d_1 {U_r}^T \underline{\tilde{x}} s^2. \tag{5.24}$$

Let $\underline{z}$ be the forces provided by $Y(s)$

$$\underline{z} = Y(s) L_m \underline{\tilde{x}} s, \tag{5.25}$$

therefore

$$\underline{z} = Y'(s)L_m\underline{\tilde{x}}s^2. \tag{5.26}$$

Performing suitable substitutions,

$$\underline{z} = UY'(s)U^T\underline{\tilde{x}}s^2, \tag{5.27}$$

and

$$\underline{z} = (U_1Y'(s){U_1}^T + U_2Y'(s){U_2}^T + ... + U_rY'(s){U_r}^T)\underline{\tilde{x}}s^2. \tag{5.28}$$

$Y'(s){U_i}^T\underline{\tilde{x}}s^2$ describes the i^{th} set of fictitious $Y'(s)$ forces as defined in Eq. (5.24). Therefore, making further substitutions, Eq. (5.28) can be written as

$$\underline{z} = U_1(c_1\underline{w}_{f1} + d_1{U_1}^T\underline{\tilde{x}}s^2) + U_2(c_1\underline{w}_{f2} + d_1{U_2}^T\underline{\tilde{x}}s^2)....+ U_r(c_1\underline{w}_{fr} + d_1{U_r}^T\underline{\tilde{x}}s^2). \tag{5.29}$$

The original system equation of motion, Eq. (5.2), can now be modified to include $\underline{z}$, defining the suspension forces provided by the $Y(s)$ device,

$$M_0\underline{\tilde{x}}s^2 + C_0\underline{\tilde{x}}s + K_0\underline{\tilde{x}} + \underline{z} = B\underline{\tilde{u}}. \tag{5.30}$$

Multiplying by s, substituting in Eq. (5.29) for $\underline{z}$, and hence introducing the $Y'(s)$ states $\underline{\dot{w}}_{f1}, \ldots, \underline{\dot{w}}_{fr}$,

$$M_0\underline{\tilde{x}}s^3 + C_0\underline{\tilde{x}}s^2 + K_0\underline{\tilde{x}}s + \sum_{i=1}^{r} U_i(c_1\underline{\dot{w}}_{fi} + d_1U_i^T\underline{\tilde{x}}s^3) = B\underline{\tilde{u}}s, \tag{5.31}$$

Substituting for $\underline{\dot{w}}_{fi}$ using Eq. (5.23), a new system equation of motion can be formed

$$M_0\underline{\tilde{x}}s^3 + C_0\underline{\tilde{x}}s^2 + K_0\underline{\tilde{x}}s + \sum_{i=1}^{r} U_i(c_1(A_1\underline{w}_{fi} + b_1{U_i}^T\underline{\tilde{x}}s^2) + d_1U_i^T\underline{\tilde{x}}s^3) = B\underline{\tilde{u}}s. \tag{5.32}$$

Grouping powers of s, and performing the following reverse substitutions

$$M_0' = M_0 + \sum_{i=1}^{r} U_id_1U_i^T, \tag{5.33}$$

$$C_0' = C_0 + \sum_{i=1}^{r} U_i c_1 b_1 U_i^T, \tag{5.34}$$

a generalised and simplified equation of motion can be formed

$$M_0' \underline{\tilde{x}} s^3 + C_0' \underline{\tilde{x}} s^2 + K_0 \underline{\tilde{x}} s + \sum_{i=1}^{r} U_i (c_1 A_1 \underline{\dot{w}}_{fi}) = B \underline{\tilde{u}} s. \tag{5.35}$$

The entire system can now be written in the time domain, in state-space form, with the fictitious states $\underline{w}_{fi}$ adjoined as follows.

$$\frac{d}{dt} \begin{bmatrix} \underline{\ddot{x}} \\ \underline{\dot{x}} \\ \underline{x} \\ \underline{w}_{fi} \\ \vdots \\ \underline{w}_{fr} \end{bmatrix} = A_{ss} \begin{bmatrix} \underline{\ddot{x}} \\ \underline{\dot{x}} \\ \underline{x} \\ \underline{w}_{fi} \\ \vdots \\ \underline{w}_{fr} \end{bmatrix} + B_{ss} \underline{\dot{u}}, \tag{5.36}$$

with the overall system and input coefficient matrices being defined respectively as

$$A_{ss} = \begin{bmatrix} -{M_0'}^{-1} C_0' & -{M_0'}^{-1} K_0 & 0 & -{M_0'}^{-1} U_1 c_1 A_1 & \dots & -{M_0'}^{-1} U_r c_1 A_1 \\ I & 0 & 0 & 0 & \dots & 0 \\ 0 & I & 0 & 0 & \dots & 0 \\ b_1 {U_1}^T & 0 & 0 & A_1 & \dots & 0 \\ \vdots & \vdots & \vdots & \vdots & \ddots & 0 \\ b_1 {U_r}^T & 0 & 0 & 0 & 0 & A_1 \end{bmatrix}, \tag{5.37}$$

$$B_{ss} = \begin{bmatrix} {M_0'}^{-1} B \\ 0_{(2n+r)\times 1} \end{bmatrix}. \tag{5.38}$$

A more visually coherent representation of Eq. (5.36) is described below, where the deletion of the state $\underline{x}$ results in the deletion of the third row and column of A_{ss}, forming A_{ss}', (a similar manipulation to B_{ss} occurs) and Eq. (5.36) is integrated with respect to time.

$$\dot{X} = A_{ss}{}'X + B_{ss}{}'\underline{u} \tag{5.39}$$

$$X = \begin{bmatrix} \underline{\dot{x}} & \underline{x} & \int \underline{w}_{fi} & \dots & \int \underline{w}_{fr} \end{bmatrix}' \tag{5.40}$$

$$A_{ss}{}' = \begin{bmatrix} -M_0'^{-1}C_0' & -M_0'^{-1}K_0 & -M_0'^{-1}U_1c_1A_1 & \dots & -M_0'^{-1}U_rc_1A_1 \\ I & 0 & 0 & \dots & 0 \\ b_1{U_1}^T & 0 & A_1 & \dots & 0 \\ \vdots & \vdots & \vdots & \ddots & 0 \\ b_1{U_r}^T & 0 & 0 & 0 & A_1 \end{bmatrix} \tag{5.41}$$

$$B_{ss}{}' = \begin{bmatrix} M_0'^{-1}B \\ 0_{(n+r)\times 1} \end{bmatrix} \tag{5.42}$$

In summary, this derivation has transformed a system's general Laplace equation of motion (Eq. (5.2)) which includes a set of m identical suspension networks, with admittance $Y(s)$, into time-domain, state-space form (Eq. (5.40)). The core purpose of building up this method is to enable the optimisation of parameters within inerter-based suspensions added to large and complicated dynamic systems, where only the numerical MCK matrices are available. Without this method, it is extremely tedious or almost impossible to analyse the system and interpret various variations of MCK matrices (when outputted with different $Y(s)$ parameter values) such that the equations of motion can be *interpreted* with any sort of accuracy. The Laplace to state-space time-domain transformation also eliminates the algebraic loops which occur when inerters are implemented straight into the equations of motion, as well as the complex matrix inversions required which demands much computational power, using a Laplace domain solution technique similar to the one used in of Section 3.2, Eq. (3.16).

5.3 Validation of the location matrix method using a low-order model in MATLAB®

Before testing this method on an industrial railway vehicle model, it is necessary to validate it using a simpler system. The system chosen is a standard, frictionless, two-mass oscillator, shown in Fig. 5.1, and contains a direct $Y(s)$ connection between the two masses. Figure 5.2 shows the six candidate optimisable $Y(s)$ networks, the same as the proposed lateral suspensions seen in Fig. 4.1, for consistency. Table 5.1 denotes the values of all parameters used.

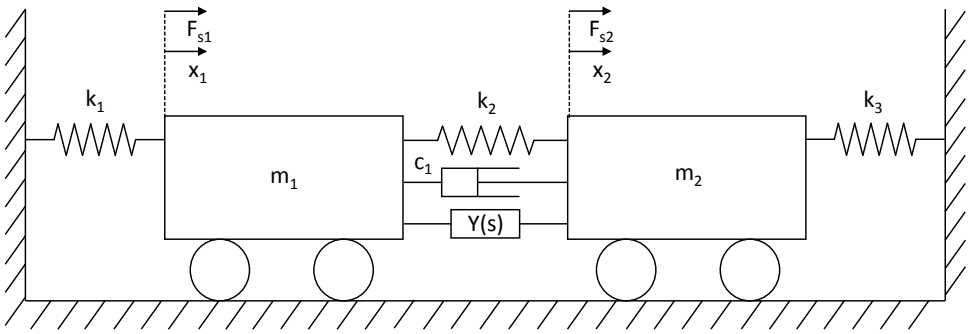

Fig. 5.1 The two-mass oscillator used to test the location matrix theory in MATLAB®.

Parameter	Value	Unit
m_1	1250	kg
m_2	3000	kg
k_1	8×10^5	Nm^{-1}
k_2	9×10^5	Nm^{-1}
k_3	6.8×10^5	Nm^{-1}
c_1	6.3×10^4	Nsm^{-1}
k_y	2.55×10^5	Nm^{-1}
k_s	2.99×10^5	Nm^{-1}
c_s	5.20×10^4	Nsm^{-1}
b_s	6.67×10^3	kg
b_{s2}	4×10^3	kg

Table 5.1 The values of the masses and components of Fig. 5.1, along with the fixed values of the $Y(s)$ network components from Fig. 5.2.

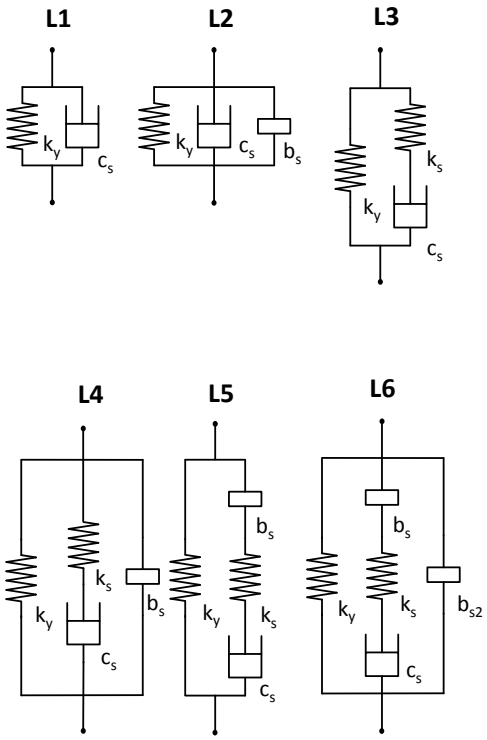

Fig. 5.2 The $Y(s)$ networks which can be implemented ino the model set out in Fig. 5.1.

The initial validation uses the true location matrix, which can be intuited from the very simple nature of the system setup seen in Fig. 5.1,

$$L_m = \begin{bmatrix} 1 & -1 \\ -1 & 1 \end{bmatrix}, \tag{5.43}$$

The validation begins by comparing the responses of mass 1 to input forces F_{s1} and F_{s2} on masses 1 and 2 respectively, using the L1 version of $Y(s)$, calculated three ways:

- **Tfsys A**. The standard formation of the Laplace equations of motion, which incorporate the stiffness, damping and inertance terms of $Y(s)$ (increasing powers of s) into the system matrix manually. Solved in the Laplace domain.
- **Tfsys Lm**. A slight variation of Tfsys A in which a location matrix is used in conjunction with the base mass, damping and stiffness matrices of the system. Solved in the Laplace domain.

- **YsLm SS**. The fully automated location matrix method, using the L_m decomposition, which include fictitious states, laid out in Section 5.2. Laplace to time-domain transform is performed in this method.

The arbitrarily introduced forces, F_{s1} and F_{s2}, can be either harmonic or step in nature, as detailed in Fig. 5.3.

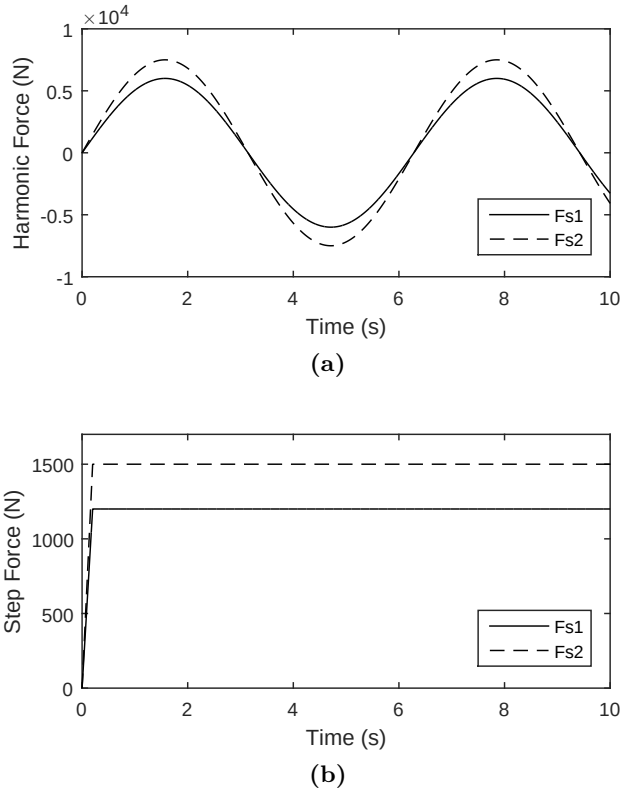

Fig. 5.3 The input forces at mass 1 (F_{s1}) and mass 2 (F_{s2}), for the harmonic and step input cases respectively.

Figures 5.4(a) and (b) show the responses of mass 1 to sinusoidal and step forcing respectively, using the three different simulations introduced above. In both cases all three curves match extremely well, and therefore increasing confidence can be gained in the location matrix method analysis technique.

The next step in the validation procedure is to test a number of different location matrices and different $Y(s)$ layouts. As the location matrices have to be symmetric, we shall begin, returning to the notation used in Section 5.2, with two V matrices

$$V_1 = \begin{bmatrix} 1 \\ -1 \end{bmatrix}, \tag{5.44}$$

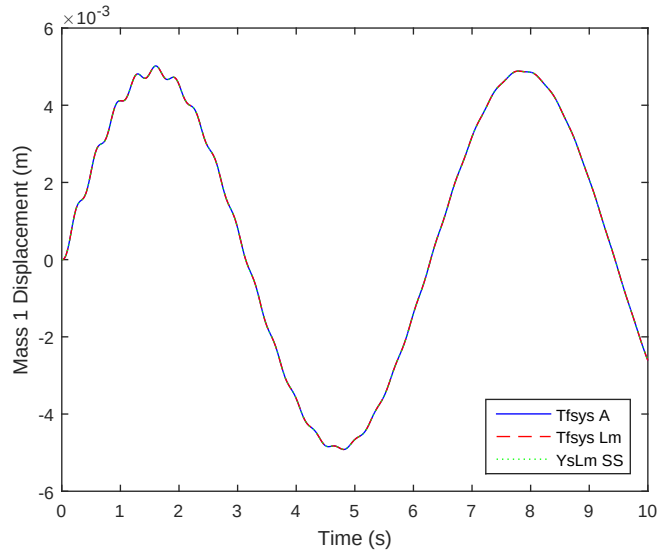

(a)

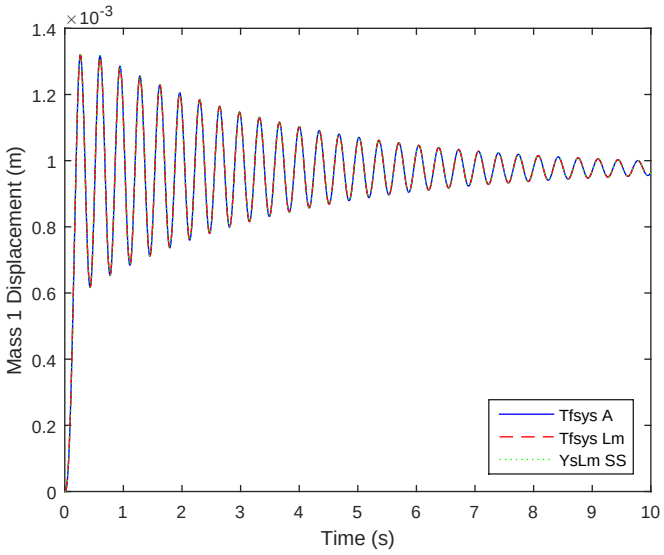

(b)

Fig. 5.4 A comparison between the three methods of simulating the simple dynamic system of Fig. 5.1, with the original location matrix, in response to the harmonic input (a), and the step input (b) at mass 1, using an L1 $Y(s)$ layout.

$$V_2 = \begin{bmatrix} 1 & 1 & 5 \\ -1 & -34.6 & 0 \end{bmatrix} \tag{5.45}$$

which form the two location matrices, via VV^T

$$L_{m1} = \begin{bmatrix} 1 & -1 \\ -1 & 1 \end{bmatrix}, \tag{5.46}$$

$$L_{m2} = \begin{bmatrix} 27 & -35.6 \\ -35.6 & 1198.16 \end{bmatrix}. \tag{5.47}$$

This test assumes we are simulating a situation where we can infer the location matrix from a large and complex system, however we cannot infer the corresponding V decomposition. L_{m1} corresponds with the exact system as defined in Fig. 5.1. L_{m2} should be thought of as still a location matrix for the Fig. 5.1 model, however one which implies that certain parameters in $Y(s)$ have been altered, and that is extremely hard to decompose. The main point to note here is that we concerned as to what system is *effectively* being modelled by the inclusion of L_{m2}; we are testing the theoretical decomposition and location matrix simulation techniques here.

Two decompositions into UU^T can be performed, each in two ways:

- Single Value Decomposition (SVD). This produces a diagonal matrix κ, and unitary matrices U_s and V_s, such that

$$U_s V_s = I, \tag{5.48}$$

and

$$U_s \kappa V_s = L_{mi}. \tag{5.49}$$

It follows that

$$U = U_s \sqrt{\kappa}. \tag{5.50}$$

- Eigenvalue Decomposition. This decomposition results in

$$L_{mi} = U_e \Sigma U_e', \tag{5.51}$$

hence

$$L_{mi} = (U_e \sqrt{\Sigma})(\sqrt{\Sigma} U_e'), \tag{5.52}$$

where U_e is a matrix of the system's eigenvectors and the diagonal matrix Σ contains the system's eigenvalues. This is very similar to the SVD, and the resulting U matrix is defined as

$$U = U_e\sqrt{\Sigma}. \tag{5.53}$$

Test case	$\Delta_{Lm_{svd}}$	$\Delta_{Lm_{eig}}$
Test 1	8.04×10^{-16}	0
Test 2	5.86×10^{-14}	7.11×10^{-15}

Table 5.2 Discrepancies between the norm of the location matrices formed by VV^T and UU^T in both test cases. Δ_{Lm} relates to the type of decomposition technique, and the test number relates to the test cases shown in Eqs. (5.44 - 5.45).

Table 5.2 shows the difference in the Euclidean Norm of the UU^T location matrix for each of the decomposition techniques ($\Delta_{Lm_{svd}}$ and $\Delta_{Lm_{eig}}$ for SVD and Eigenvalue decomposition respectively), for each test case, and the original VV^T location matrix. The minute differences observed assert the fact that both decomposition techniques yield the same results. The Eigenvalue decomposition will be used for the rest of the analysis in this chapter as it is slightly more simplistic in nature. The equations

$$U_{2_{svd}} = \begin{bmatrix} -0.9922 & 5.1005 \\ 34.6141 & 0.1462 \end{bmatrix}, \tag{5.54}$$

$$U_{2_{eig}} = \begin{bmatrix} -5.1005 & -0.9922 \\ -0.1462 & 34.6141 \end{bmatrix}, \tag{5.55}$$

$$L_{m2_{svd}} \approx L_{m2_{eig}} \approx L_{m2_{True}} = \begin{bmatrix} 27 & -35.6 \\ -35.6 & 1198.16 \end{bmatrix}, \tag{5.56}$$

show the U matrices for the Test 2 case, now introducing the fictitious states, and the identical nature of the resulting location matrix. Simulation of the two-mass system, with identical inputs, is then performed using the location matrix method, with the original inputs, for each U decomposition case, and a variety of $Y(s)$ cases. The resulting responses for every $Y(s)$ and decomposition case (original V, U_{svd}, and U_{eig}) are found to be identical. Figures 5.5(a) and (b) show the results for Test 2, simulated respectively with a sinusoidal and step input. These positive results further consolidate the validity of the location matrix method, and confidence is gained in

using simulation methods which introduce fictitious states, and therefore inconceivable dynamic systems.

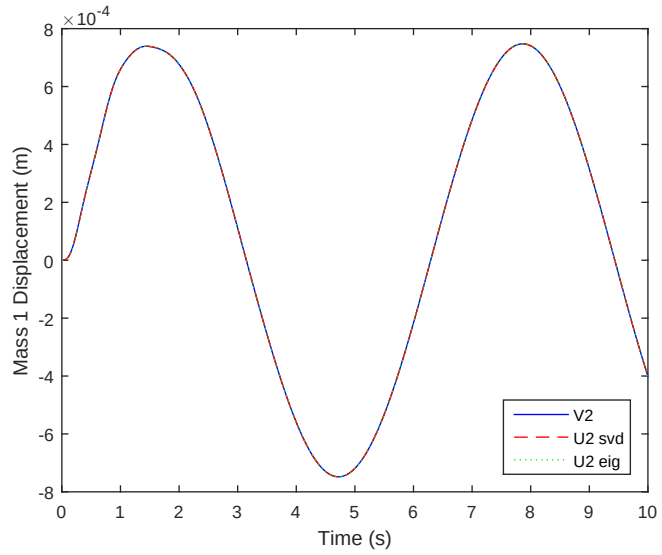

(a)

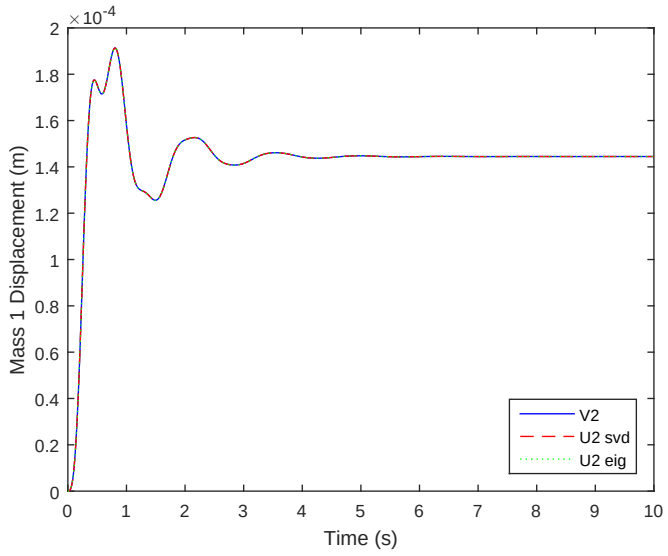

(b)

Fig. 5.5 A comparison between the three location matrix methods, for test case 2 (see Eqs. (5.45 - 5.55)), of simulating the simple dynamic system of Fig. 5.1 in response to the harmonic input (a), and the step input (b) at mass 1, using an L6 $Y(s)$ layout.

5.4 Application to railway vehicle suspension optimisation

The location matrix method detailed in Sections 5.2 and 5.3 has been used with VAMPIRE® to simulate a four-axle railway vehicle [115], with the aim of optimising its lateral suspension and improving its curving performance and passenger comfort. The vehicle used is the four-axle VTISM model which was introduced in Chapter 3, Section 3.3. Passenger comfort is quantified by the RMS lateral carbody acceleration, when the vehicle is subject to a 5 km stretch of lateral track disturbance, taken from a real track, much like the analysis techniques defined in Chapter 3, Section 3.2.1.

Before applying the location matrix method to a full vehicle model, optimising suspension parameters, one must first validate the method on the four-axle model. To simplify the analysis, and target and determine any discrepancies which may occur, a simpler input of lateral forcing at the front wheelset in used (rather than Track160 displacement inputs, which consists of 5km of lateral irregularities).

Applying Eq. (5.2) to the railway vehicle, M_0, C_0 and K_0 are respectively the mass, damping and stiffness matrices exported from VAMPIRE® for the hypothetical base model with no primary lateral suspension at all, which amongst other things contain information regarding the wheel-rail contact patch forces. The primary lateral suspension elements are therefore included in the $Y(s)$ part of Eq. (5.2). B includes wheel-rail contact force information when the input $\underline{u}$ matrix consists of real track disturbance data, and is simply unity when $\underline{u}$ is a forcing input. For the forcing input case, $\underline{u}$ is a positive lateral force on the centre of mass of the front wheelset for the first second, an equal and opposite force for the 6th second, and zero at all other times.

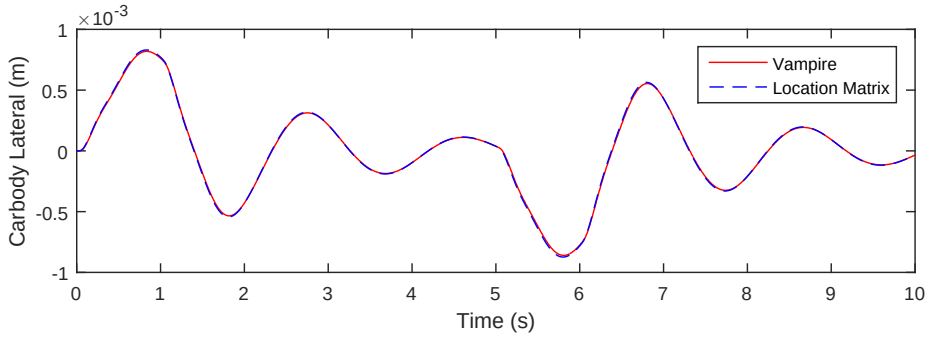

Fig. 5.6 A comparison between the inherent VAMPIRE® and finalised location matrix methods of simulation of a four-axle VAMPIRE® vehicle model, showing the carbody lateral movement with a lateral forcing input of 10 kN.

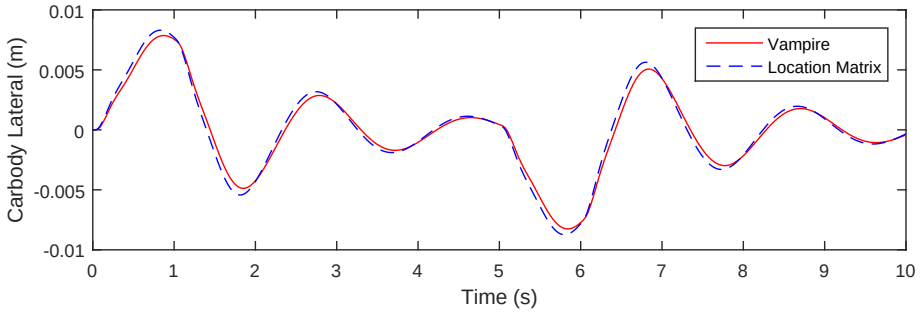

Fig. 5.7 A comparison between the inherent VAMPIRE® and finalised location matrix methods of simulation of a four-axle VAMPIRE® vehicle model, showing the carbody lateral movement with a lateral forcing input of 100 kN.

Figures 5.6 and 5.7 show how the VAMPIRE® and location matrix simulations compare for lateral step force magnitudes of respectively 10 kN and 100 kN, specifically focussing on the carbody's lateral motion, and using an L1 bush layout with default parameter values. It is clear that a closer match occurs at the lower forcing input, and at the higher forcing input the location matrix method predicts slightly higher amplitudes of oscillation. It should be noted that at a lateral force of 10 kN, many different $Y(s)$ suspension layouts with and without inerters have been tested with the location matrix method and the comparisons with VAMPIRE® are correct to a very high degree of accuracy. The transient analysis within VAMPIRE® has been linearised to the extent that there is there is no friction saturation at the contact patch, meaning that a linear contact model is used, however it is impossible to linearise the M_0, C_0 and K_0 matrices completely as the normal force of the vehicle on the track (perpendicular to the wheel's profile) is not distributed equally or consistently when the vehicle is displaced or exhibits hunting motion, resulting in the creep force parameters within the system matrix (Eq. (5.37)) varying during the simulation. This cannot be accounted for using the location matrix method in its current form as values within the base exported matrices cannot vary, and therefore the time varying normal force is the key factor changing the exported matrices from VAMPIRE®.

Figure 5.8 demonstrates the extent to which the normal force at the front right wheel contact patch varies during the simulation. When the lateral track displacement is used as the input, and when the stability of the vehicle is assessed using a standard stability track (where the vehicle is excited and then the oscillations are left to diminish) comparisons between the VAMPIRE® and location matrix methods of calculation yield different results in terms of respectively the RMS lateral acceleration of the carbody, and the steady state displacement of the wheelset.

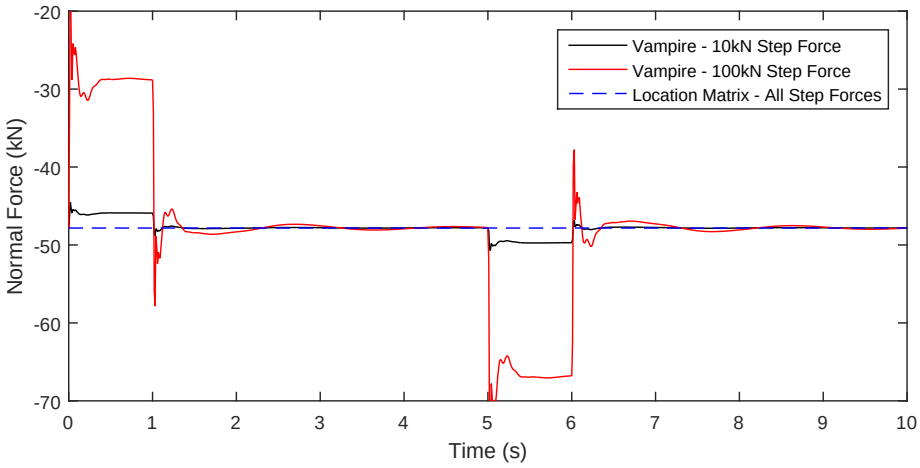

Fig. 5.8 Contact patch normal force variations at the front left wheel-rail contact patch of the four-axle railway vehicle when subject to the lateral wheelset 1 step input simulation. Note the vertical (z) direction is defined as positive downwards, therefore these forces can be thought of as reaction forces, and the normal force is *normal* to the contact patch plane, not necessarily in the upwards direction.

Although one cannot be certain that the time varying normal force is the only phenomenon which results in a change in the overall system matrix, it can be concluded that although the location matrix method can be used to provide preliminary optimisations for a lateral suspension device on a constant normal force and linear contact four-axle railway vehicle model, further investigations are required for a full nonlinear analysis. These further investigations are reported in Chapter 6, where VAMPIRE® and MATLAB® interact in a way which enables the optimisation of suspensions where the simulations take place in VAMPIRE®, rather than using linearised exported MCK matrices in MATLAB®. The location matrix method, nevertheless, is a neat technique of incorporating arbitrary suspensions into much more complicated dynamic systems.

5.5 Summary

Whilst the analysis and optimisations of Chapter 4 were performed on a two-axle railway vehicle model in MATLAB®, the aim of this chapter is to enable the optimisation of a more complex and realistic railway vehicle when exported from an industrial piece of software (VAMPIRE®) in MCK matrix form.

To this end, the research presented in this chapter has introduced, derived and validated a method for simulating dynamic systems by which interchangeable suspension elements can be incorporated at certain locations via their admittance functions in the Laplace domain, whilst the base mass, stiffness and damping matrices are used

unchanged. This Laplace to state-space location matrix method has the potential to allow large scale dynamic systems exported from industrial software to be analysed, and chosen suspension networks with known admittance functions to be optimised for a range of cost functions. This method is applicable when one wishes to optimise suspension parameters that are not already introduced to industrial dynamic systems, and these systems are highly complex and the equations of motion are near on impossible to decipher. Each optimisation iteration, it allows an input of the admittance function of a proposed suspension network, however the simulation occurs in time-domain state space-form, avoiding large and challenging matrix inversions and algebraic loops created by introducing inerters.

In this project, the challenges described above were extensive when attempting to simulate, in a similar manner to the method described in Section 3.2, the VAMPIRE® four-axle vehicle model. The large numbers of DOF involved made the transfer functions within the matrices of an extremely high order, making inversions impossible in MATLAB® . This aspect was the main motivation for developing the location matrix simulation method.

The method builds on the fact that the location matrix (which defines the coupling positioning of additional suspension networks along with scaling factors) of an additional suspension device can be decomposed into decomposition matrices. When it is not feasible or impossible to correctly infer these matrices from the large dynamic system, eigenvalue decompositions or SVDs take place. Combining these with the non-unique canonical decomposition of the force to acceleration transfer function of the suspension device in question, extra, fictitious, states are introduced to the dynamics, and are present in the final state-space time-domain set of equations.

The method has been successfully validated using a simple two-mass MATLAB model, and for a range of inerter and non-inerter based suspension networks, to an extremely high degree of accuracy. Both decomposition techniques yield correct results and both sinusoidal and step forcing inputs have been tested. When applied to the VTISM four-axle railway introduced in Chapter 3, a much higher order model, the system responses to small to medium forcing inputs are correct. However, as the inputs and resulting displacements become higher, the system becomes more and more nonlinear due to the presence of asymmetric normal forcing at the wheel-rail contact patch. The changes in base stiffness and damping matrices become significant and can no longer be ignored, therefore the location matrix method becomes less effective at simulating responses. This method has potential to produce preliminary optimisations for linearised railway vehicle models, however to perform a robust and nonlinear analysis and optimisation of the realistic passenger vehicle model, it is inevitable that the VAMPIRE® simulations will have to be performed at each iteration.

To solve the problem of VAMPIRE® being unable to perform optimisations, and the fact that certain inherent vehicle nonlinearities need to be accounted for to perform a full optimisation and vehicle assessment, the content of Chapter 6 pursues an approach which combines both MATLAB® 's optimisations capabilities, as well as the necessary simulation and analysis techniques only available in VAMPIRE®.

Chapter 6

Track friendliness improvement of a four-axle model

In this chapter we:

- Perform primary lateral suspension optimisations on the four-axle VAMPIRE model introduced in Chapter 3, with the aim of minimising the PYS, whilst maintaining permissible levels of passenger comfort.
- Use MATLAB® and VAMPIRE® in co-simulation during the optimisation, alongside the structure-immittance approach, to determine beneficial inertance-integrated networks, using a range of vehicle velocities and wheel-rail conicities.
- Detail results of simulations using the optimised vehicles with nonlinear wheel-rail contact data and the square-root creep law.
- Perform standard industrial tests on the optimised vehicles, again with nonlinear wheel-rail contact data, to determine whether any unwanted dynamic behaviour is introduced by such suspensions.

6.1 Introduction

Whilst Chapter 5 provided a method which enables linear vehicle optimisations, the inherent nonlinearities within railway vehicles, even under linear contact conditions, mean that other methods of analysis were sought to pursue the validation of the use of inerters within the scope of railway vehicles. The analysis and results presented in this chapter, the core *validation and further testing* chapter in this thesis, not only show how VAMPIRE® and MATLAB® can combine to respectively simulate and optimise railway vehicles and their suspension elements, but detail that when nonlinear simulations and industry standard tests are performed on the optimised vehicles, no significant performance detriments are observed, all tests are passed, and in the most

critical speed and conicity case, both straight running *and* curving performance benefits are obtainable.

A chronological overview of the content of this chapter is as follows. To begin with, the generic suspension networks to be considered are introduced, and the extent to which the structure-immittance approach to network-synthesis can be used in VAMPIRE® is assessed. The optimisation procedure is then detailed, along with how VAMPIRE® and MATLAB® interact with one another, before preliminary optimisations take place on the default rubber bush. Four beneficial inertance-integrated suspension networks are then determined through the systematic optimisation of the lateral portion of the trailing arm bush, with a widened parameter space (which comes with tailored fluid-passageway devices), using a linear contact law for computational efficiency. Lastly, validation tests using nonlinear wheel and track profiles, and the square-root creep law, are then performed on the optimised vehicles, along with industry standard tests which determine whether or not the addition of inerters causes detrimental effects in any area.

The results presented and discussed in this chapter were reported in the following publications:

- T. D. Lewis, Y. Li, G. J. Tucker, J. Z. Jiang, Y. Zhao, S. A. Neild, M. C. Smith, R. Goodall, N. Dinmore. Improving the track friendliness of a four-axle railway vehicle using an inertance-integrated lateral primary suspension. *Vehicle System Dynamics: International Journal of Vehicle Mechanics and Mobility*, 2019.
- T. D. Lewis, Y. Li, G. J. Tucker, J. Z. Jiang, S. A. Neild, M. C. Smith, R. Goodall, S. Iwnicki, N. Dinmore. Inertance-integrated primary suspension optimisation on an industrial railway vehicle model. *Proceedings of the 26th IAVSD International Symposium on Dynamics of Vehicles on Roads and Tracks (IAVSD)*, 2019.

The VAMPIRE® simulations for the VUC analysis of Section 6.3.2, and the additional vehicle assessments of Section 6.3.3 were performed by Dr. Gareth Tucker at the University of Huddersfield, and processed and analysed by myself at Bristol.

6.2 Identifying beneficial primary suspension configurations for PYS reduction

This section introduces an optimisation procedure using VAMPIRE® simulations and MATLAB optimisation commands with the aim of reducing the multi-stage VAMPIRE® vehicle's PYS by optimising the primary lateral suspension without worsening passenger comfort. As discussed in Section 2.1, decreasing the PYS increases the propensity of the wheelset to yaw, which decreases the forces at the contact patch.

This, in turn, decreases T_γ, which decreases the VUC (see Chapter 6.3.2). As with previous chapters, the focus on the primary lateral suspension is because this approach has been found to be found to beneficial in previous studies. Firstly, the default rubber bush will be optimised for comparison purposes, followed by a variety of inertance-integrated devices. Three beneficial inertance-integrated layouts are identified and the corresponding performance benefits are demonstrated.

6.2.1 Candidate inertance-integrated layouts using the structure immittance approach

In this work, the conventional (default) layout as seen in Fig. 6.1(a) is labelled S1 and will be optimised first. Candidate inertance-integrated layouts for the primary lateral suspensions (② in Fig. 3.6) will be proposed using the structure-immittance approach [116]. This approach allows generic suspension structures, which can cover all potential networks with a pre-determined complexity, to be established in VAMPIRE® and explored in a systematic manner during the optimisations. The constraints on element values can also be easily applied in the optimal design process.

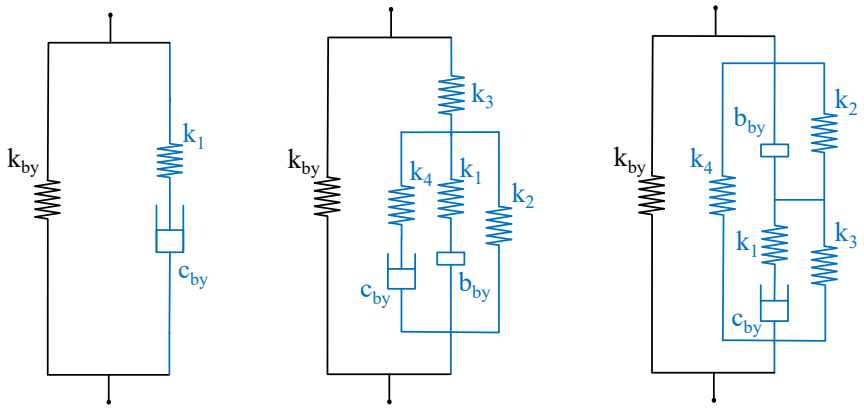

(a) S1 **(b)** Generic network 1 (GN1). **(c)** Generic network 2 (GN2).

Fig. 6.1 The default S1 suspension network, and the two generic networks which can be used to make up the eight layouts consisting of one inerter, one damper, and one spring, using the structure-immittance approach

For simplicity of design, layouts consisting of one spring, one damper, and one inerter ($1_k1_c1_b$) will be considered here. Following the formulation procedure detailed in [116], two generic layouts which cover all eight ($1_k1_c1_b$) layouts are shown in Figures 6.1(b) and (c). These two generic layouts are implemented in VAMPIRE® (with inerters being introduced in accordance with Section 3.3.3) in parallel with a fixed lateral static stiffness (k_{by}) replacing the conventional primary lateral suspension. When optimising each of the generic layouts, the parameter values of the inerters, dampers and springs are varied with the condition that only one spring is present in

the optimised layout and the others must take a value of zero or infinity depending on their position. Note that, if manufacturing constraints allow it, layouts with an increased complexity can also be established and investigated following the procedure developed in [116].

6.2.2 Optimisation cost function, constraints, and procedure

To maintain a satisfactory level of passenger comfort when reducing the vehicle's PYS, performance constraints on the passenger comfort are considered in the optimisation. For this study, the passenger comfort is quantified as the average value of the carbody's Root Mean Squared (RMS) acceleration, as measured at floor level above the centre of each bogie. Three linear wheel conicity (0.1, 0.3 and 0.5) and three forward vehicle speed (11.2 ms^{-1}, 22.4 ms^{-1} and 33.5 ms^{-1}) cases, forming a total of nine conicity and speed combinations, are investigated to ensure a thorough analysis of the vehicle's performance. This is done because the vehicle speed inherently varies as it accelerates and decelerates, and its conicity varies over its lifespan, which can be a number of decades. For computational efficiency, the optimisations performed in Section 6.2 use a linear creepage vs creep force dependency, plus linear conicity (I.E. constant conicity for any value of wheelset displacement). The validation in Section 6.3 utilises the square root creep law along with real wheel-rail contact information.

The vehicle used in this study has a rated velocity of 33.5 ms^{-1}, and its dynamics are assessed using the VAMPIRE® library track file Track160. This track, introduced in Chapter 3, Section 3.2.1 is a 5 km track that is representative of a standard, straight, GB track with a line speed of 160 kph. In this analysis, all track geometries are used as inputs; i.e. irregularities in curvature, cant, lateral and vertical alignment, and gauge variations, as opposed to only the lateral variations considered in Chapter 3, Section 3.2.1. At the two highest velocity and conicity combinations (conicity 0.3 and 0.5 at 33.5 ms^{-1}) the maximum permitted RMS acceleration is constrained to 100% of the default values. However, a relaxed constraint of 110% of the default RMS values is used for the seven other cases, as these are assumed to be less critical in the control of instabilities.

Bushing type	k_{by} (MNm^{-1}) fixed	k_{iy} (MNm^{-1})	c_{by} ($kNsm^{-1}$)	b_{by} (kg)	PYS (%) of default
Rubber bush	1.752	1 - 5	1 - 5	-	0.001 - 100
Inertance-integrated device	1.752	1 - 10	1 - 50	1 - 7000	0.001 - 100

Table 6.1 The proposed parameter space of rubber bushes, and inertance-integrated lateral suspension devices to be optimised.

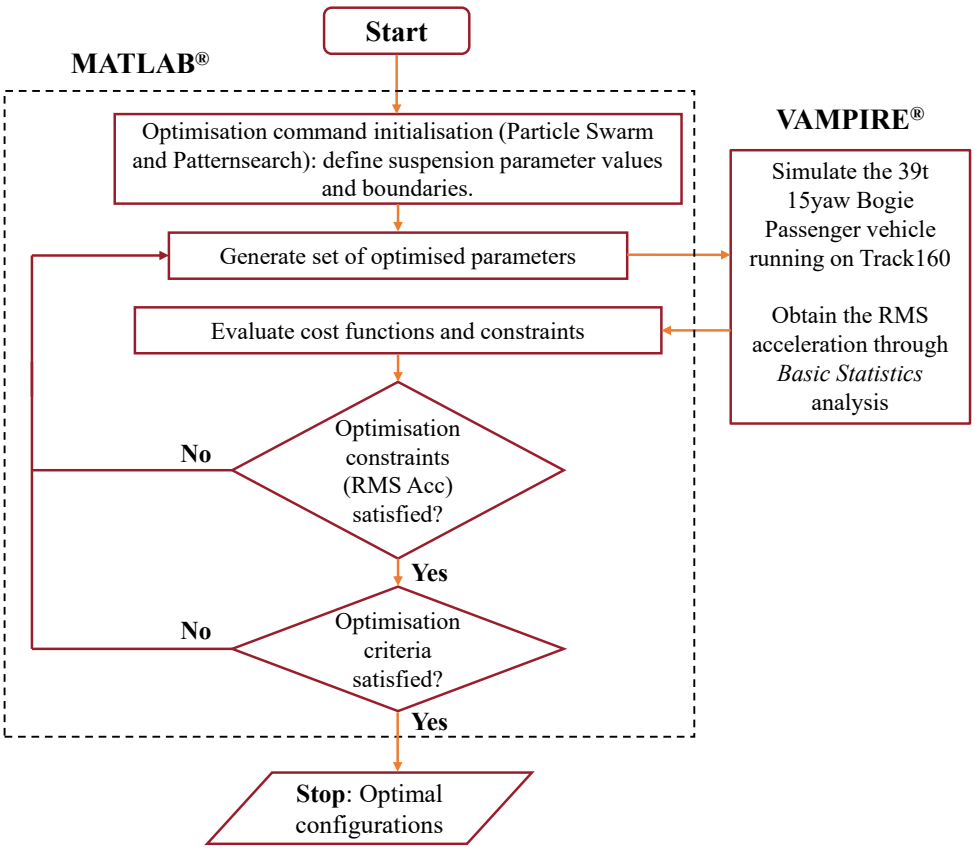

Fig. 6.2 A flow-chart showing how MATLAB® and VAMPIRE® interact within the optimisation process.

The parameters of the primary lateral suspension elements are allowed to be optimised but will be constrained within certain ranges, as shown in Table 6.1. The conventional primary lateral suspension comprises a rubber bush [7] (see Fig. 6.1(a)), which has a limited range of achievable stiffness and damping values. This will be optimised first to demonstrate the maximum benefits that a rubber bush can achieve. Inertance-integrated layouts introduced in Section 6.2.1 will then be optimised. A wider parameter space for these layouts will be assumed considering various realisation possibilities (e.g. hydraulic bushing devices with orifice induced damping, devices using ball-screw and lever arm based inertance). For example, if considering a helical-tube fluid inerter device [30, 117], the inertance is given by

$$b = m\left(\frac{A_1}{A_2}\right)^2 = m\left(\frac{r_1}{r_2}\right)^4, \tag{6.1}$$

where b denotes inertance, m is the mass of the fluid in the tube, and respectively A_1 and r_1 the area and radius of the piston, and A_2 and r_2 the area and radius of the helical tubing. A similar analysis was alluded to in Chapter 2, Section 2.3.1. It can be

calculated that a r_1 to r_2 ratio of 10 can achieve 7000 kg of inertance with 0.7 kg of fluid in the tube. Note that to form a fair comparison and maintain the vehicle's static lateral behaviour, the static stiffness, k_{by}, remains fixed at a value of 1.752 MNm^{-1} throughout the optimisation process.

Figure 6.2 displays a flow-chart detailing the interaction between MATLAB® and VAMPIRE within the optimisation procedure. MATLAB® is used to perform the optimisations (using Genetic Algorithms such as Patternsearch and Particle Swarm Optimisation (PSO)) and calls VAMPIRE® to perform a defined simulation for each iteration. For each iteration, the cost function, K_{bx}, and the parameter values of the primary suspension in question are allowed to vary as the optimisation inputs change. Each VAMPIRE® run consists of the vehicle being subject to Track160, using a simulation time-step of 0.0001s.

6.2.3 Optimisation results detailing beneficial suspension configurations

The optimisation results have been summarised in Table 6.2, where the variation and reduction of the total PYS is based on the optimised k_{bx}. The first two lines of Table 6.2 (S1 default and S1$_a$) show that the PYS can only be reduced by 2% with an optimum rubber bush, using the parameters space detailed in Table 6.1, and the values of RMS acceleration for the default S1 and optimised rubber bush are almost identical. This suggests that the default values for the primary lateral suspension used in the *BogiePassenger 39t 15yaw* model are very similar to the optimal ones when considering only rubber bushes. To form a fair comparison, the next set of optimisation results show that when the default S1 bush is optimised with the widened parameter space (shown in Table 6.1), the PYS is allowed to be reduced by 21% (See S1$_b$ in Table 6.2), as the series stiffness and damping components increase in value.

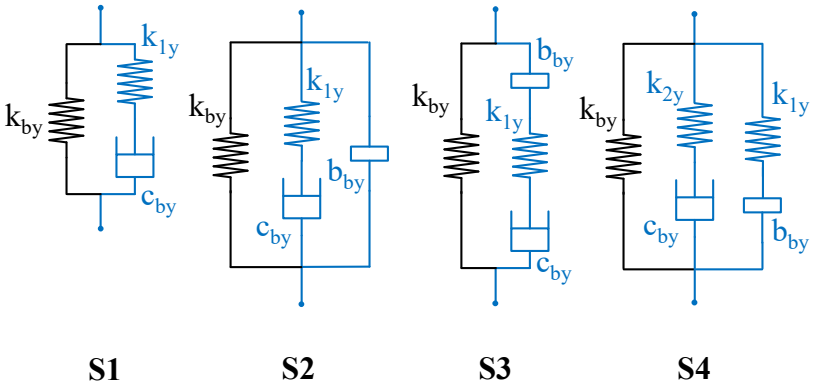

Fig. 6.3 The default bushing layout along with the three identified beneficial inertance-integrated networks.

Using the candidate layouts proposed by the structure-immittance approach (see Section 6.2.1), several inertance-integrated configurations have been identified, as shown in Fig. 6.3: S2-S4. Optimisation results detailed in Table 6.2 yield significant PYS reductions of 47%, 41% and 47% respectively for layouts S2, S3 and S4. Note that for S4, a damping compliance k_{2y} has been included to make the modelling more realistic, as in reality all dampers have a certain amount of end-stiffness. The method by which the reduction in PYS shown in Table 6.2 manifests in monetary savings is shown is Section 6.3.2.

Layout	k_{1y} (MNm^{-1})	k_{2y} (MNm^{-1})	c_{by} (kNsm^{-1})	b_{by} (kg)	PYS (abs) MNmrad^{-1}	PYS (%) of default
Default	3.50	-	1.75	-	15.00	100
$S1_a$	3.38	-	1.93	-	14.72	98
$S1_b$	10.00	-	50.00	-	11.92	79
S2	4.17	-	38.45	3905.63	7.99	53
S3	9.09	-	50.00	6829.94	8.83	59
S4	9.24	10.00	50.00	2550.00	7.99	53

Table 6.2 Optimisation results for reducing the PYS of the four-axle VTISM model (Fig. 3.6); showing PYS reductions, and optimised parameter values when using inertance-integrated layouts, as well as the default and optimised S1 rubber bush.

Figure 6.4 details the RMS carbody acceleration values with the five optimised solutions for different conicities and velocities set out in Table 6.2. The horizontal dashed lines represent the default RMS acceleration value for each velocity and conicity combination, whilst the dotted lines show the relaxed 110% constraint defined in Section 6.2.2. Firstly, it can be seen that at conicity 0.5 and 33.5 ms^{-1}, configurations S2, S3 and S4 provide significant reductions in carbody RMS acceleration (of respectively 18.5%, 5.2%, and 13.8%) whilst permitting the PYS to be decreased. Note that these results are based on simulations carried out using simplified, linear contact models.

Layout	Conicity 0.1 Velocity (ms^{-1})			Conicity 0.3 Velocity (ms^{-1})			Conicity 0.5 Velocity (ms^{-1})			PYS (%) of S1
(% diff)	11.2	22.4	33.5	11.2	22.4	33.5	11.2	22.4	33.5	default
$S1_a$	-	-	-	-	-	-	-	-	-	98
$S1_b$	0.00	**-3.47**	**-0.94**	0.00	**-3.98**	**-2.80**	**-0.64**	**-5.53**	**-4.43**	79
S2	8.47	7.43	5.63	10.00	5.98	**-6.16**	7.69	5.14	**-18.49**	53
S3	5.08	2.97	1.56	6.00	**-1.20**	**-0.28**	1.92	**-5.14**	**-5.21**	59
S4	8.47	5.94	5.00	8.67	4.78	**-0.56**	5.13	4.3	**-13.80**	53

Table 6.3 Percentage reductions (−) or increases (+) in RMS carbody accelerations for all beneficial configurations (concerning the optimisation of the four-axle model (Fig. 3.6 for reduced PYS) when compared to the default suspension ($S1_a$), when linear contact modelling is used, for each conicity and velocity combination.

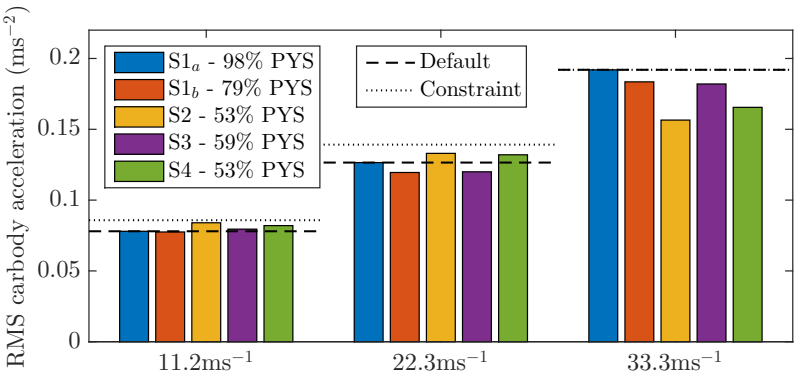

(a) Conicity 0.5.

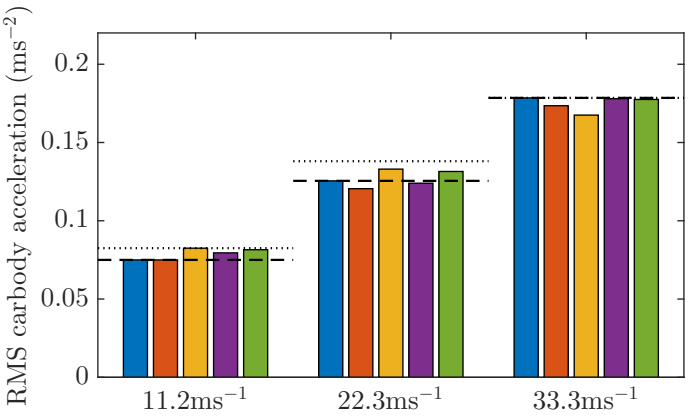

(b) Conicity 0.3.

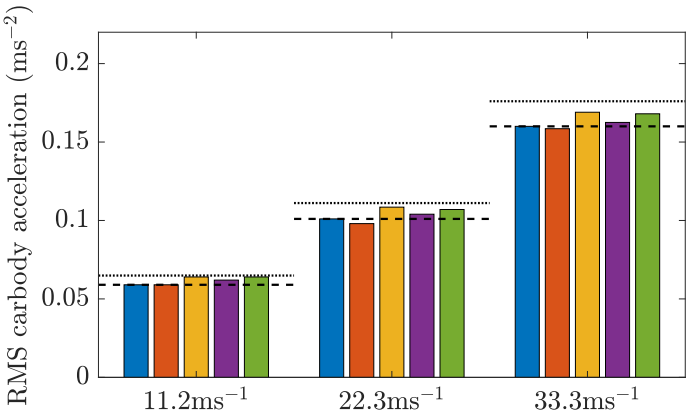

(c) Conicity 0.1.

Fig. 6.4 Optimisation results showing how RMS carbody acceleration varies with vehicle velocity and linear conicity, for configurations defined in Table 6.2 and Fig. 6.3. The horizontal dashed lines represent the default RMS acceleration value for each velocity and conicity combination, whilst the dotted lines show the relaxed 110% constraint introduced in Section 6.2.2.

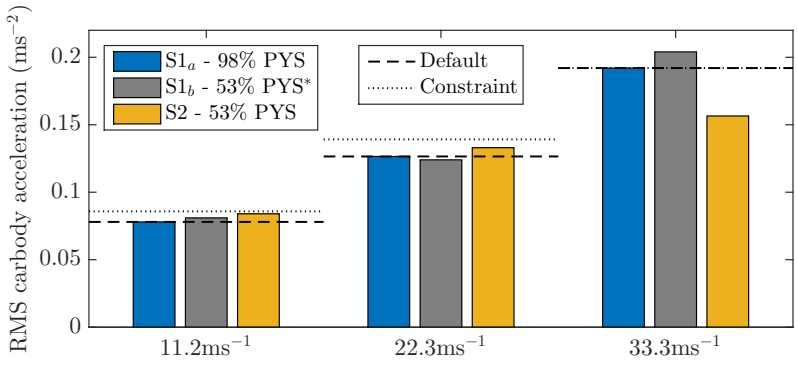

(a) Conicity 0.5.

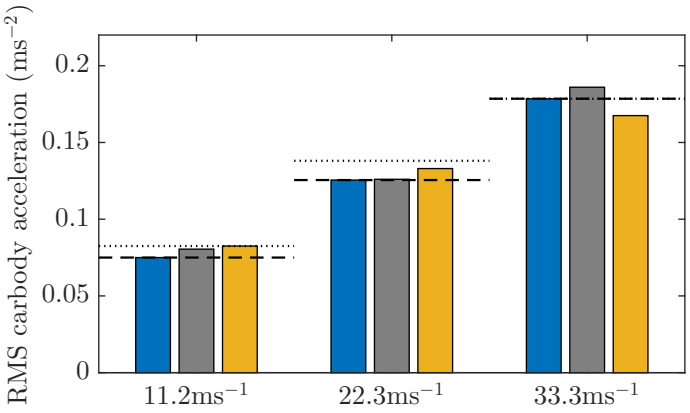

(b) Conicity 0.3.

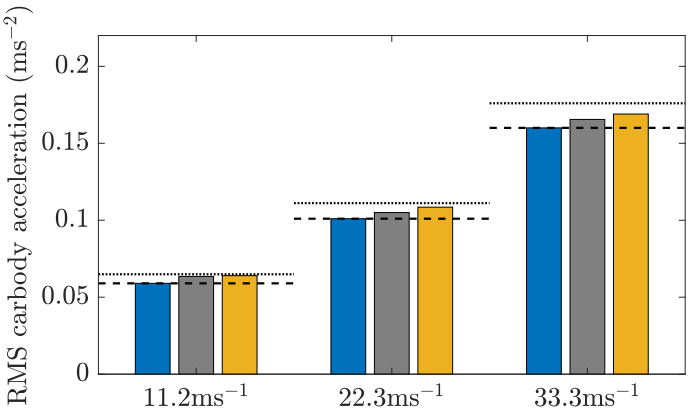

(c) Conicity 0.1.

Fig. 6.5 Optimisation results showing RMS carbody acceleration values for configuration S1$_b$ with a PYS of 53% rather than 79% to demonstrate the effect of a reduced PYS on a layout without an inerter. For reference, S1$_a$ and the inerter-based S2 data are reproduced from Fig. 6.4. The horizontal dashed lines represent the default RMS acceleration value for each velocity and conicity combination, whilst the dotted lines show the relaxed 110% constraint introduced in Section 6.2.2.

At the two lower speeds in Fig. 6.4, S3 and S4 perform nominally better than S2, and at conicity 0.1, all configurations are far less susceptible to changes in vehicle speed, in terms of deviating from their relative RMS acceleration performance. The percentage differences between the RMS values for $S1_b$, S2, S3 and S4, and $S1_a$ (acting as the default) can be seen in Table 6.3, with the improvements (-) in bold font. To understand the effect of a reduced PYS on the system without an inerter, Fig. 6.5 shows the S_{1b} layout with 53% PYS (i.e. the same PYS value that is used with the S2 layout). It can be seen that for the two cases with conicity 0.3 and 0.5 (at 33.5 ms^{-1}) the inertance-integrated configuration S2 is far superior compared with the lower speed and conicity cases. This suggests that the inclusion of an inerter in the suspension allows the PYS to be reduced whilst improving or maintaining the passenger comfort.

6.3 Assessing beneficial inertance-integrated suspensions

The optimisation detailed in Section 6.2 uses simplified, linear conicity contact models and Track160 for the sake of computational efficiency. It should be noted though, that unlike completely linear analysis undertaken in Chapter 5 using exported mass, stiffness, and damping matrices, here the analysis is nonlinear in the sense that the normal contact force, amongst other parameters, varies at every time-step; just the contact law and wheel-rail conicity is linear. The performance of the linearly optimised devices is now considered using more realistic wheel-rail contact models. Here a nonlinear contact model based on measured wheel-rail pairs with equivalent conicities of 0.1, 0.3, and 0.5, and nonlinear creep vs creep force friction saturation is included in the model. Benefits in Network Rail Vehicle Usage Charge (VUC) that a reduced PYS brings are calculated, and the effects of the modified suspension design on vehicle behaviour in curve transitions and in response to one-off peak lateral irregularities are investigated. Note that no further optimisation takes place in this section, and flange contact is not reached in any of the simulations. It is anticipated that flange contact would be detrimental to both track and wheel wear as well as passenger comfort.

6.3.1 Acceleration analysis using nonlinear wheel-rail contact data

In this section, measured worn wheels from a the research project detailed in [118] are used in the VAMPIRE® simulations to assess the performance advantages obtained by the use of inertance-integrated structures. The equivalent conicity (discussed at length in Section 3.3.2) of these wheel-rail pairs is calculated based on a 3 mm lateral offset, now using a nonlinear rrd graph. Figure 6.6 shows the RMS accelerations with all the beneficial solutions shown in Table 6.2 when the nonlinear contact model is used. The horizontal dashed lines represent the RMS values obtained with the $S1_a$ configurations for each velocity and equivalent conicity case. The percentage changes when compared with $S1_a$ can be seen in Table 6.4, with the improvements ($-$) in bold font. Note that in Table 6.4, the changes are calculated relative to the $S1_a$ case.

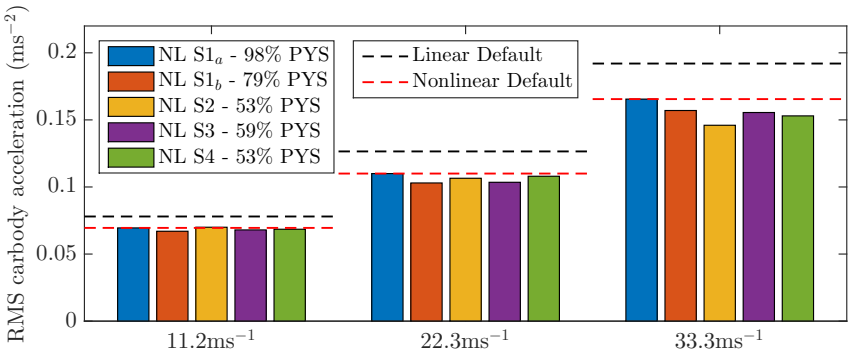

(a) Equivalent Conicity 0.5.

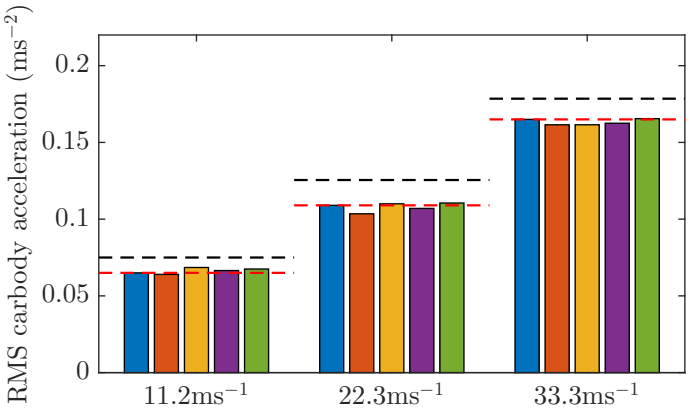

(b) Equivalent Conicity 0.3.

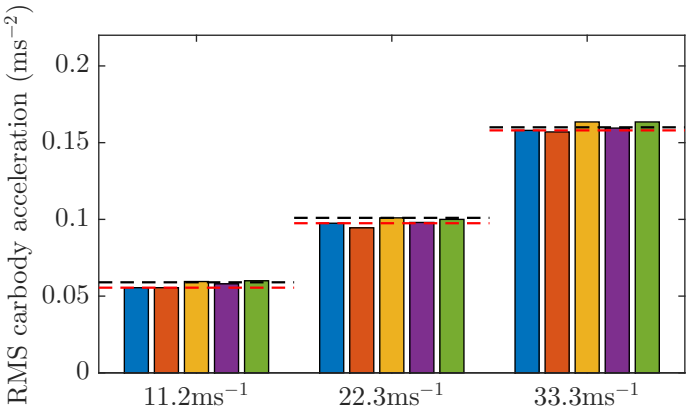

(c) Equivalent Conicity 0.1.

Fig. 6.6 Showing the RMS carbody acceleration vs vehicle velocity variation for vehicles simulated with optimal primary suspensions, now using measured wheel-rail contact data rather than linear conicity. Note that no constraints exist here (as no further optimisation has taken place), only linear and nonlinear default RMS accelerations corresponding to each velocity and equivalent conicity case.

From Tables 6.3 and 6.4 it can be observed that at 33.5 ms^{-1} and the highest equivalent conicity (0.5) cases, the RMS accelerations are still reduced significantly for the nonlinear case, but the reductions in percentage terms are smaller than in the corresponding linear cases. This is because the optimisation did not include nonlinear contact modelling. In addition, it is positive to see that for lower conicity and velocity cases there are no large increases in RMS acceleration (of over 10%) in Table 6.4. Table 6.5 shows the percentage difference in the RMS carbody acceleration for each standalone case (conicity, velocity and configuration type) when comparing the nonlinear contact model simulations with the linear ones. It can be seen that for every case, the linear contact model over-predicts carbody acceleration, and furthermore, this over-prediction in general is exacerbated as the conicity (or equivalent conicity) increases. This phenomenon occurs due to the fact that the equivalent conicity of the measured wheel-pairs, is measured at a lateral offset of 3 mm, and between 0 - 3 mm lateral offset, the gradient of the rolling radius difference graph will most likely be flatter. Note that the raw values of the RMS carbody acceleration are reported in Tables 6.6 and 6.7 for respectively the optimisations using linear contact modelling, and the nonlinear contact modelling validation checks.

Layout	Eq. Conicity 0.1 Velocity (ms^{-1})			Eq. Conicity 0.3 Velocity (ms^{-1})			Eq. Conicity 0.5 Velocity (ms^{-1})			PYS (%) of S1
(% Δ)	11.2	22.4	33.5	11.2	22.4	33.5	11.2	22.4	33.5	default
$S1_a$	-	-	-	-	-	-	-	-	-	98
$S1_b$	0.00	**-3.08**	**-0.63**	**-1.54**	**-5.05**	**-2.12**	**-3.60**	**-6.36**	**-5.14**	79
S2	7.21	4.66	3.48	6.20	0.92	**-2.42**	0.72	**-3.62**	**-11.78**	53
S3	4.50	1.55	0.95	3.10	**-1.83**	**-1.81**	**-2.16**	**-6.33**	**-6.04**	59
S4	8.11	3.63	3.48	4.65	1.38	0.00	**-1.44**	**-2.26**	**-7.55**	53

Table 6.4 Percentage reductions (−) or increases (+) in RMS carbody acceleration (concerning the four-axle model Fig. 3.6 for reduced PYS) for S2, S3, and S4 when compared to the default suspension ($S1_a$), when measured wheel-rail pairs, and nonlinear contact modelling is used, for each conicity and velocity combination.

(% Δ)	Eq. Conicity 0.1 Velocity (ms^{-1})			Eq. Conicity 0.3 Velocity (ms^{-1})			Eq. Conicity 0.5 Velocity (ms^{-1})			PYS (%) of S1
	11.2	22.4	33.5	11.2	22.4	33.5	11.2	22.4	33.5	default
$S1_a$	**-5.93**	**-4.46**	**-1.25**	**-14.00**	**-13.15**	**-7.28**	**-10.90**	**-12.65**	**-13.80**	98
$S1_b$	**-5.93**	**-3.08**	**-0.95**	**-14.67**	**-14.11**	**-6.92**	**-13.55**	**-13.81**	**-14.44**	79
S2	**-7.03**	**-6.91**	**-3.25**	**-16.97**	**-17.29**	**-3.58**	**-16.67**	**-19.92**	**-6.71**	53
S3	**-6.45**	**-5.77**	**-1.85**	**-16.35**	**-13.71**	**-8.71**	**-14.47**	**-13.75**	**-14.56**	59
S4	**-6.25**	**-6.54**	**-2.68**	**-17.18**	**-15.97**	**-6.76**	**-16.46**	**-18.18**	**-7.55**	53

Table 6.5 Percentage reductions in RMS carbody acceleration (when optimising the the four-axle model Fig. 3.6 for reduced PYS) considering the nonlinear simulation results relative to the linear simulations for each conicity, velocity, and layout case.

	Eq. Conicity 0.1			Eq. Conicity 0.3			Eq. Conicity 0.5		
Velocity (ms^{-1})	11.2	22.4	33.5	11.2	22.4	33.5	11.2	22.4	33.5
$S1_a$	0.059	0.101	0.160	0.075	0.126	0.179	0.078	0.127	0.192
S2	0.064	0.109	0.169	0.083	0.133	0.168	0.084	0.133	0.157
S3	0.062	0.104	0.163	0.080	0.124	0.178	0.080	0.120	0.182
S4	0.064	0.107	0.168	0.082	0.132	0.178	0.082	0.132	0.166

Table 6.6 RMS carbody acceleration values for each velocity, conicity, and suspension configuration case as a result of the linearised optimisations for reduced PYS performed in Section 6.2, which concern the four-axle model (Fig. 3.6).

	Eq. Conicity 0.1			Eq. Conicity 0.3			Eq. Conicity 0.5		
Velocity (ms^{-1})	11.2	22.4	33.5	11.2	22.4	33.5	11.2	22.4	33.5
$S1_a$	0.056	0.097	0.158	0.065	0.109	0.166	0.070	0.111	0.166
S2	0.060	0.101	0.164	0.069	0.110	0.162	0.070	0.107	0.146
S3	0.058	0.098	0.160	0.067	0.107	0.163	0.068	0.104	0.156
S4	0.060	0.100	0.164	0.068	0.111	0.166	0.069	0.108	0.153

Table 6.7 RMS carbody acceleration values for each velocity, conicity, and suspension configuration case when the optimised vehicle's performances are re-evaluated using nonlinear wheel-rail contact data.

Figure 6.7 shows how the RMS acceleration varies with a continuous range of vehicle velocity from 20 - 100 mph (8.9 - 44.7 ms^{-1}). It can be seen that in contrast to the low equivalent conicity case (0.1), the RMS carbody accelerations at the high equivalent conicity cases (0.3 and 0.5) obtained with the beneficial inertance-integrated configurations can be reduced further at higher vehicle speeds, comparing with the default suspension. These observations are consistent with the optimisation targets introduced in Section 6.2.

Further analysis of the vehicle's dynamics when using nonlinear wheel-rail contact data yield that bogie hunting behaviour begins at 100 mph, and that the inertance integrated suspensions S2 and S4 can induce higher peak and high frequency accelerations on the bogie and carbody (see Fig. 6.8). However, when an inerter is placed in parallel with a damper (S3), these effects are minimised.

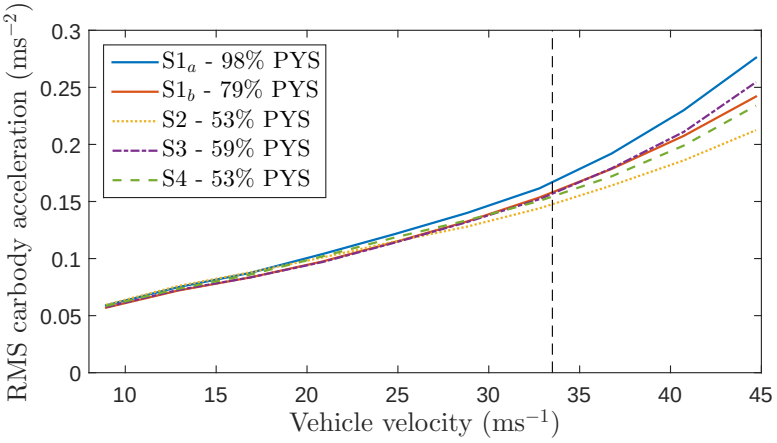

(a) Equivalent Conicity 0.5.

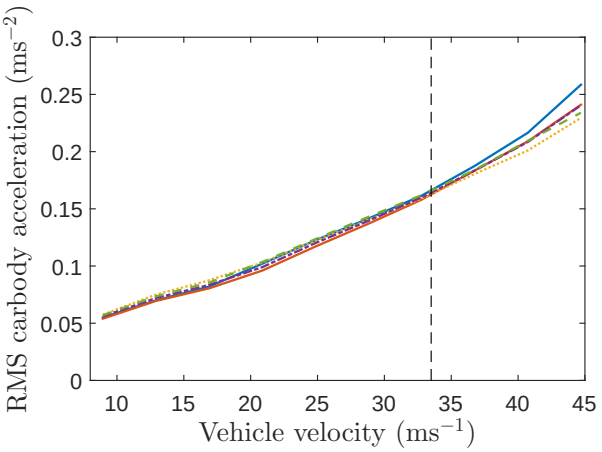

(b) Equivalent Conicity 0.3.

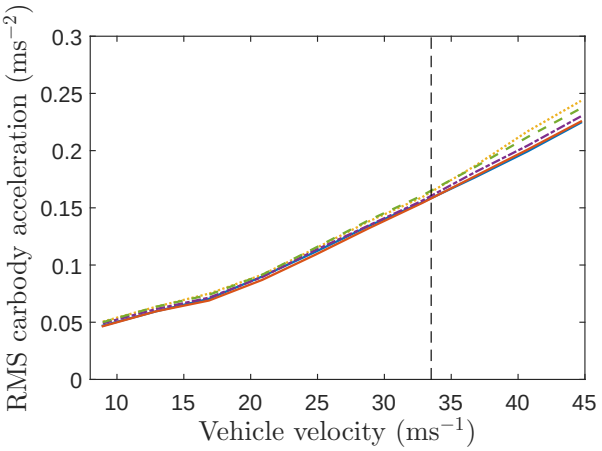

(c) Equivalent Conicity 0.1.

Fig. 6.7 Continuous velocity RMS carbody acceleration checks using nonlinear wheel-rail contact data. The vertical dashed line denotes the operational velocity of 33.5 ms^{-1}.

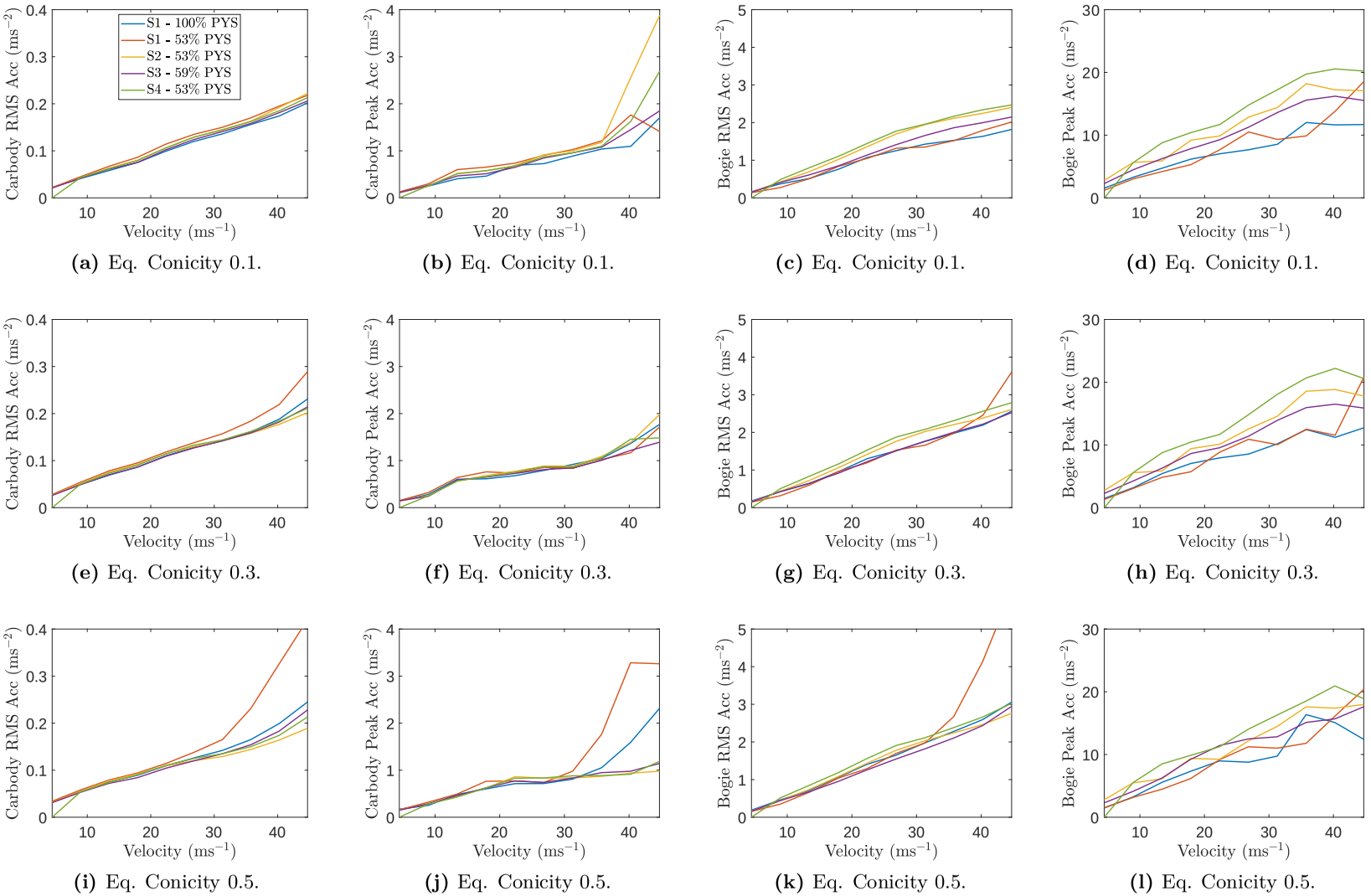

(a) Eq. Conicity 0.1. **(b)** Eq. Conicity 0.1. **(c)** Eq. Conicity 0.1. **(d)** Eq. Conicity 0.1.

(e) Eq. Conicity 0.3. **(f)** Eq. Conicity 0.3. **(g)** Eq. Conicity 0.3. **(h)** Eq. Conicity 0.3.

(i) Eq. Conicity 0.5. **(j)** Eq. Conicity 0.5. **(k)** Eq. Conicity 0.5. **(l)** Eq. Conicity 0.5.

Fig. 6.8 How different types of acceleration (Carbody RMS, Carbody Peak, Front Bogie RMS, Front Bogie Peak) vary with vehicle velocity for vehicles with the default suspension, the default suspension with 53% PYS, and the three optimal inertance-integrated suspension configurations (S2-S4).

Frequency analysis

The following plots display the timeseries and frequency content of the carbody acceleration of vehicles with default and optimised primary lateral suspensions. Figures 6.9(a)-(d) show timeseries of the carbody's lateral motion above the front bogie at equivalent conicity 0.1, 0.3 and 0.5 at 33.5 ms^{-1}, and 0.1 at 40 ms^{-1}. All six primary lateral suspension configurations considered in Table 6.2 are displayed.

The Power Spectral Densities (PSDs) of the timeseries shown in Figures 6.9(a)-(d) are shown in Fig. 6.10. Note that S1 and $S1_a$ lines are consistently very similar in nature. Observing Fig. 6.10(b) and (c) (detailing the nominal operating situations) the benefits of the inertance-integrated structures to passenger comfort are most prominent above 4 Hz; and similar to very slightly worse dynamic behaviour can be seen within the lower rigid-body frequency range. In Fig. 6.10(b) and (c) there is a brief frequency range (4 - 6 Hz) where S2 can be seen to be most beneficial, with S4 still providing significant benefits in this zone.

It is worth observing that for all curves generated at 33.5 ms^{-1} (Fig. 6.10(a)-(c)), in general, increasing the equivalent conicity increases the amplitude of response of the higher rigid-body modes (above 4 Hz), and decreases the responses of the lower rigid-body modes (below 4 Hz). This can be explained by the fact that increasing conicity increases the rrd, hence increases the centring forces. This results in a higher frequency of the motion of the wheelsets, and a more complex model interaction. It is positive to see that in all of these three cases, the inertance integrated structure, S2, provides the best reduction in amplitude between 4 - 6 Hz, however at equivalent conicity 0.1, the response is slightly deteriorated at 2 Hz when this configuration is used. The 40 ms^{-1} and Equivalent Conicity 0.1 case is used to observe the likely behavior at for a vehicle travelling at 'high-speed' and 'low conicity'. It can be seen that the inertance-integrated structures perform less well than in the 33.5 ms^{-1} cases; nominally decreasing the performance below 4 Hz, and slightly increasing the performance above 4 Hz. This can be explained by the fact that 40ms $^{-1}$ is not the optimisation velocity.

The waterfall style plots of Fig. 6.11(a) and (b) show the one-sided full amplitude FFT of two carbody acceleration timeseries (optimised S4, at equivalent conicity 0.1, and at both 33.5 ms^{-1} and 40ms $^{-1}$), plotted against both frequency and time - i.e. the power spectrum of the signal at a number of time intervals. The vehicle stability will decrease as the forward velocity increases, however the vehicle is deemed stable at 40 ms^{-1} and equivalent conicity 0.1 due to the stable nature of Figures 6.9(d) and 6.11(b). It can be observed from Fig. 6.11 that the S4 configuration produces a shift towards higher amplitudes at lower rigid-body modes at a higher speed. This phenomena is exacerbated by larger track perturbations at roughly 110 seconds.

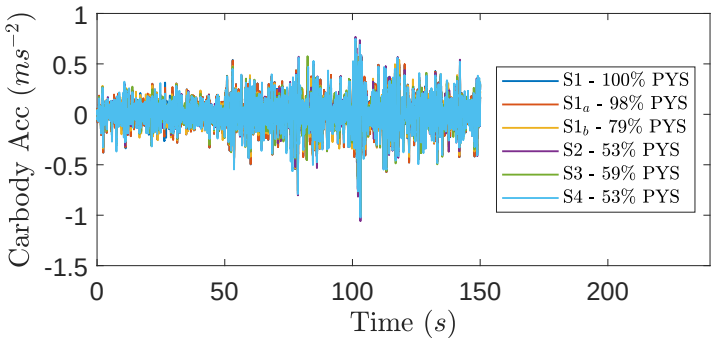

(a) Equivalent Conicity 0.1, 33.5 ms^{-1}.

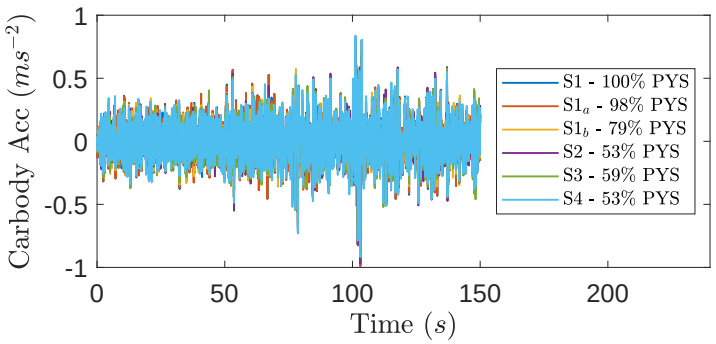

(b) Equivalent Conicity 0.3, 33.5 ms^{-1}.

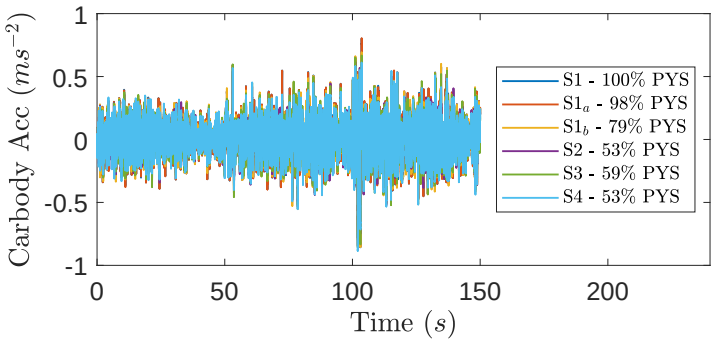

(c) Equivalent Conicity 0.5, 33.5 ms^{-1}.

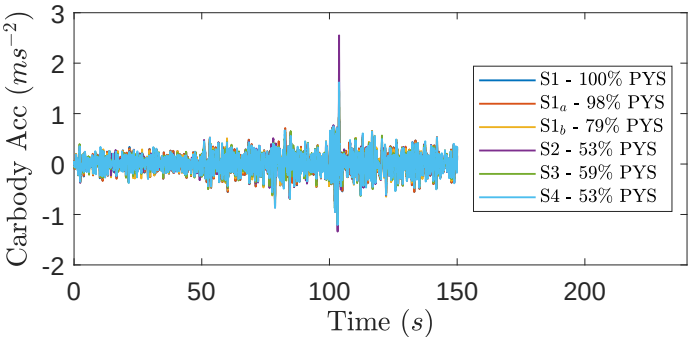

(d) Equivalent Conicity 0.1, 40 ms^{-1}.

Fig. 6.9 Acceleration timeseries of vehicles with the default suspension (comparing changes in PYS) and optimised suspensions, when subjected to a track with a rated line speed of 160 kph.

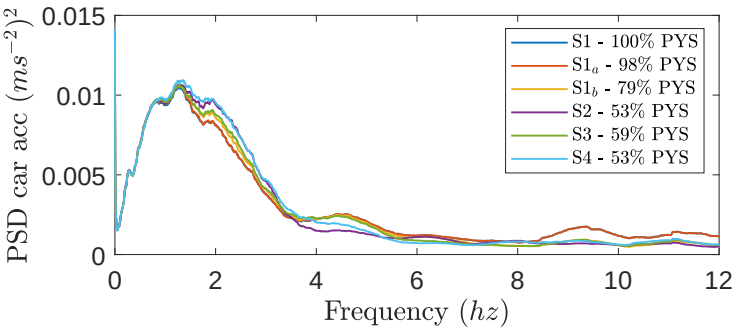

(a) Equivalent Conicity 0.1, 33.5 ms^{-1}.

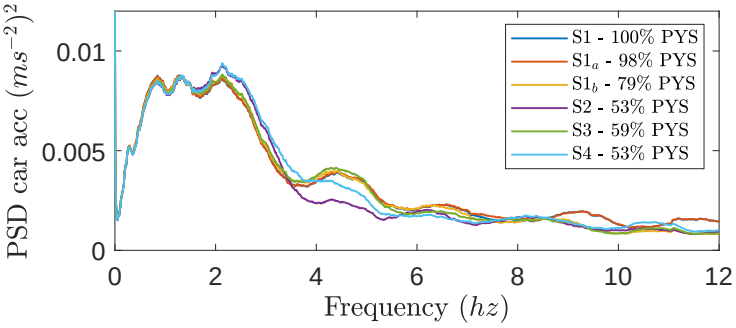

(b) Equivalent Conicity 0.3, 33.5 ms^{-1}.

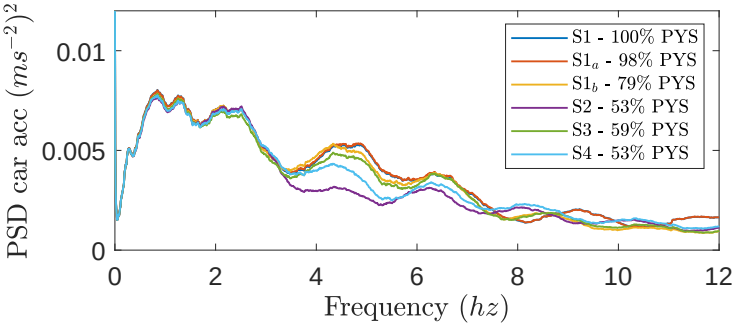

(c) Equivalent Conicity 0.5, 33.5 ms^{-1}.

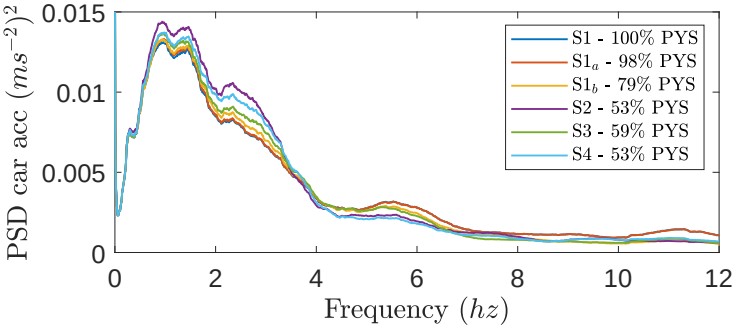

(d) Equivalent Conicity 0.1, 40 ms^{-1}.

Fig. 6.10 PSD plots of vehicles with the default suspension (comparing changes in PYS) and optimised suspensions, when subjected to a track with a rated line speed of 160 kph.

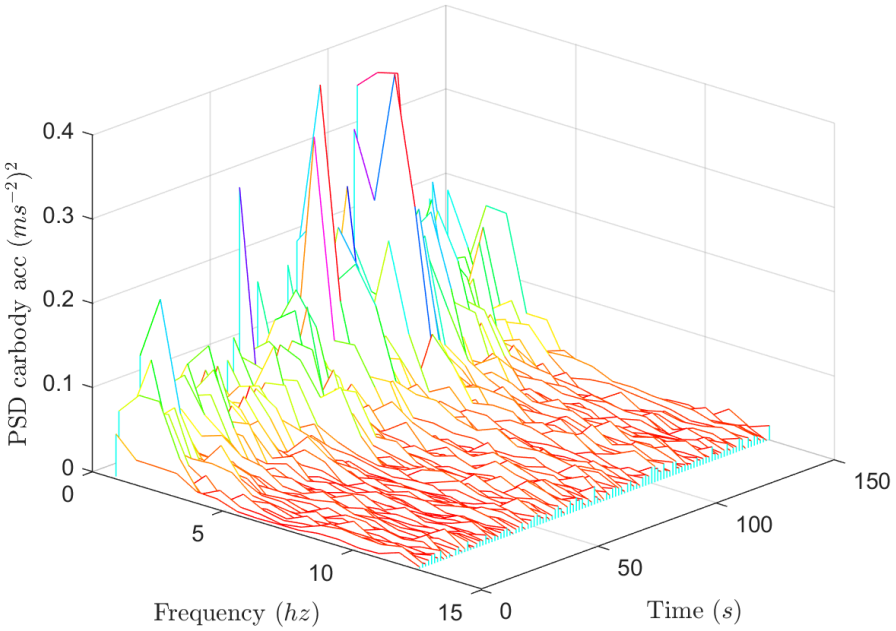

(a) Equivalent Conicity 0.1, 33.5 ms^{-1}, S4 - 53 % PYS.

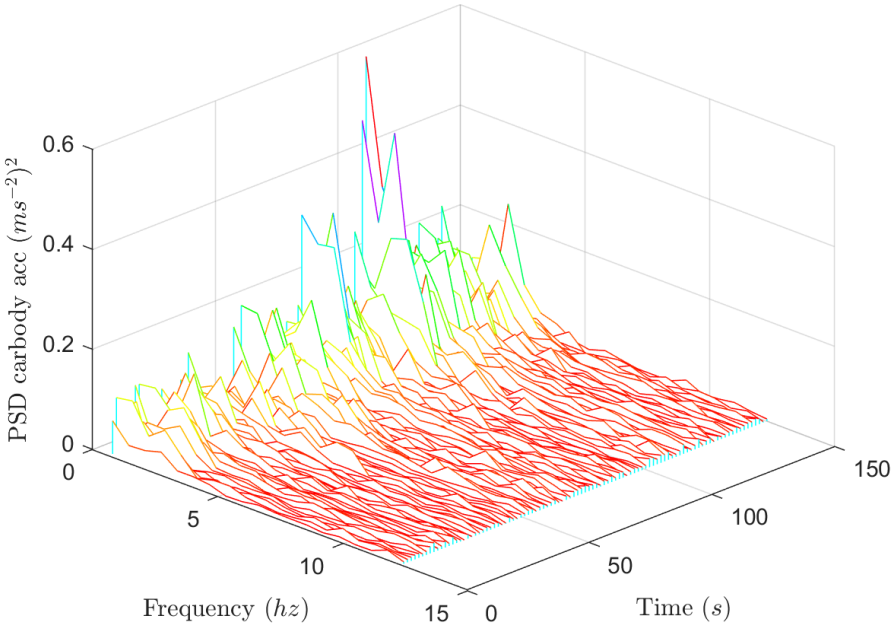

(b) Equivalent Conicity 0.1, 40 ms^{-1}, S4 - 53 % PYS.

Fig. 6.11 3D Waterfall plots of Carbody acceleration amplitude, frequency and time, for a vehicle with an optimised lateral suspension layout S4, at 0.1 conicity, and at 33.5 ms^{-1} and an increased speed of 40 ms^{-1}.

Peak counting assessment

As well as analysing carbody acceleration with nonlinear wheel-rail contact data vs velocity and a PSD analysis, peak counting assessments, in accordance with The Rail Safety and Standards Board (RSSB) Railway Group Standard GM/RT2141 [119], have been performed. The peak counting method of vehicle safety assessment states that only certain percentage of peak accelerations (maxima in the acceleration vs time curve) may exceed a certain level of acceleration, measured in g. This percentage exceedance threshold value decreases with increasing discrete levels of acceleration, as the situation is becoming more and more dangerous, and the vehicle more susceptible to derailment and roll-over. This is denoted by the bold black line in Fig. 6.12.

All vehicles with optimised primary lateral suspensions, at all velocity and conicity combinations, have been subject to a lateral peak counting assessment (a function which is built into VAMPIRE®); in every assessment the vehicle has passed, I.E. the curves lie within the safe region, below the threshold line. Figure 6.12 shows an example result, for S1 default and optimised S2, at 0.3 and 0.5 conicity, and at 33.5 ms^{-1} (the two most critical cases).

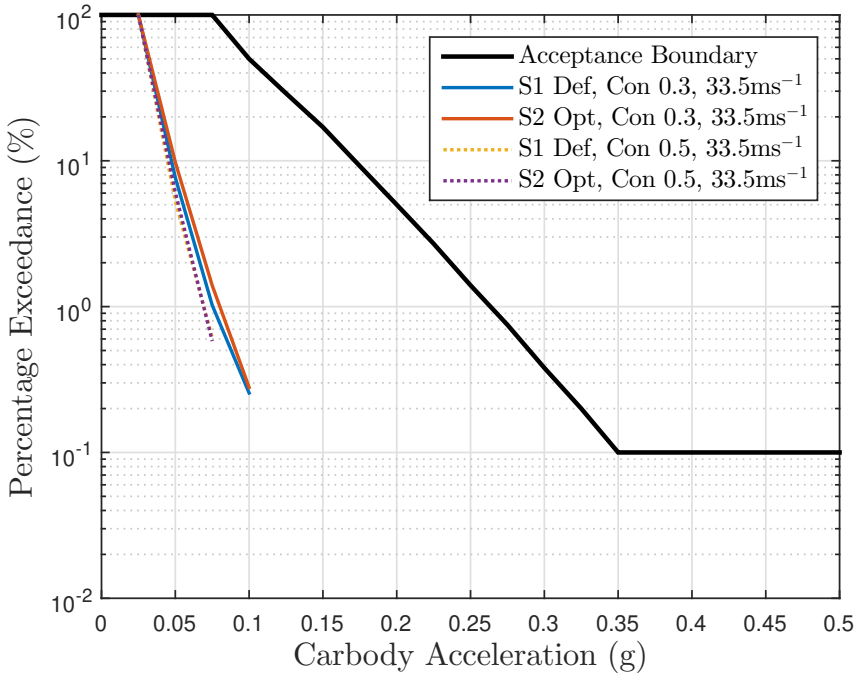

Fig. 6.12 Peak counting results for a nonlinear analysis of vehicles with the S1 default suspension layout, and the optimised S2 layout, at the two highest equivalent conicity cases, and at the vehicle's rated velocity of 33.5 ms^{-1}.

6.3.2 Reductions in Network Rail Variable Usage Charge (VUC)

Reducing a vehicle's PYS improves curving performance, and therefore reduces rail surface damage (both wear and rolling contact fatigue) during curving, due to lower values of T_γ. The benefits can be assessed using the VUC. This is made up of charges arising from signals, tracks, other structures and surface damage, and is calculated using the Network Rail spreadsheet found in [2].

Figure 6.13 shows how the VUC (measured in pence/vehicle mile) changes when the inertance-integrated suspensions allow the PYS to be reduced. Note that only the surface damage portion is affected by a reduced PYS. It can be seen that the S2 and S4 configurations with 53% PYS delivers a 26% reduction in VUC, whilst the $S1_b$ and S3 layouts, which respectively have a PYS of 59% and 79% give VUC reductions of 18% and 10%. These results are very beneficial from an economic perspective, and it is anticipated that rolling stock manufacturers will be inspired by these figures, and future research, to adopt the inerter as a standard railway vehicle suspension element in the future.

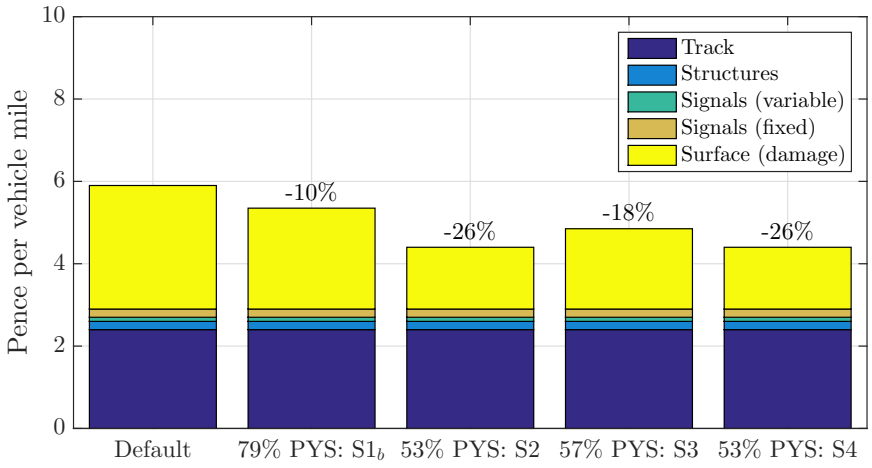

Fig. 6.13 The effect that reducing the PYS of the four-axle vehicle has on the VUC, for each beneficial suspension configuration.

6.3.3 Additional vehicle dynamics assessments using measured contact data

This section considers the behaviour of vehicles with inertance-integrated suspensions in curved transitions and when subject to one-off peak lateral irregularities; both legal requirements which must be adhered to.

Curve transitions

When a railway vehicle approaches a curve, the track is designed to transition from a straight line to a steady state curve. This can be achieved with a linear increase in the applied cant and rate of curvature (i.e. the inverse of curve radius). In the steady-state section of the curve, where the radius and cant do not change, the contact forces reduce with a reduced PYS (as implied in Section 6.3.2). In this section, the vehicle behaviour in curve transitions are considered to check whether the reduced PYS and optimised inerter-based suspensions will cause any unwanted behaviour. Simulations have been carried out for the vehicle approaching a 200 m radius curve, with a 100 mm applied cant running at at a speed of 18 ms^{-1} to give the maximum permitted cant deficiency of 150 mm [120]; a transition length of 40 m is used to give the worst-case cant gradient of 1:400 [120]. Vehicles with suspension layouts S2, S3 and S4, as well as a default vehicle with a PYS of 53% of the default value are compared. Here the default vehicle modified with a PYS of 53% is shown to allow us to see how the addition of optimised inerter-based lateral suspensions affects the overall dynamics. The vehicle is travelling through a right-hand curve, and a new P8 wheel [121] combined with a new CEN60E2 rail has been used in these simulations. The changes in curvature and cant are shown in Fig. 6.14.

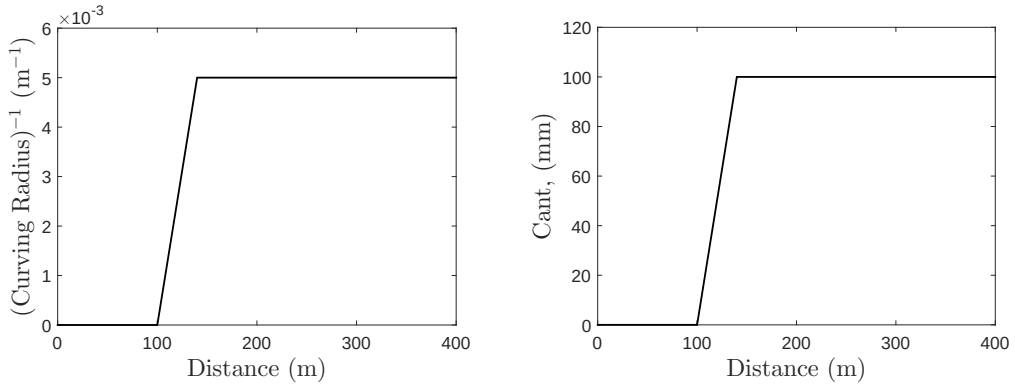

(a) Applied curvature. **(b)** Applied cant.

Fig. 6.14 Showing how the track curvature and cant angle vary in the tight curve when performing the curve transition vehicle dynamics assessment

Figures 6.15(b) and 6.16(b) show how the lateral contact forces for the right wheel on wheelset 1 and the left wheel on wheelset 2 (where the highest forces occur) on the front bogie vary during the initial 2 m in a curve transition. Figures 6.15(a) and 6.16(a) show the whole of the initial transient period. The forces for the $S1_a$, S2, S3 and S4 vehicles (with respective PYSs of 53%, 59%, 53%, and 59%) are largely similar for the majority of the 40 m duration, yet it can be seen from Fig. 6.15 that the peak lateral forces for inertance-integrated layouts are slightly higher than for the default vehicle with 53% PYS, and the peaks are at a greater distance from the start of the

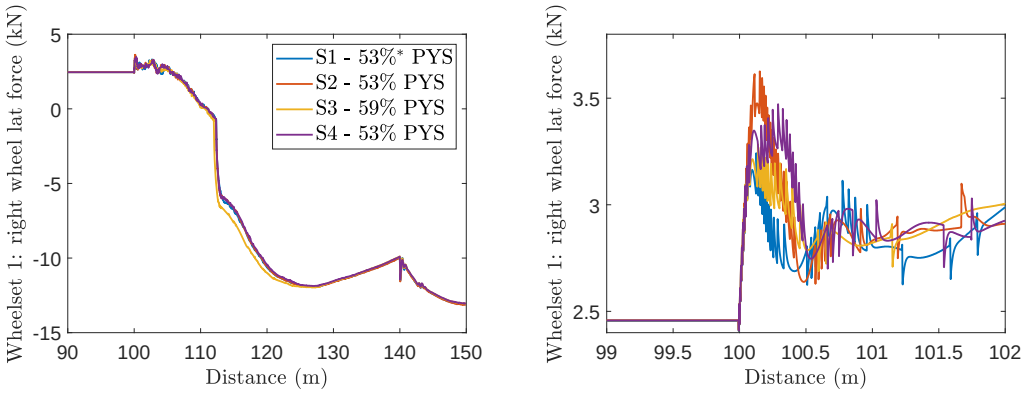

Fig. 6.15 Lateral forces at the right (inner) wheel of wheelset 1 in the initial section of the curve transition. (a) shows the full curve transition (from 100 - 140 m), and (b) shows in more detail the lateral force variations at the start of the transition. Note the S1 configuration has a modified PYS of 53%.

transition. For the left wheel on the second wheelset (Fig. 6.16), S2 gives the greatest peak lateral force whilst S3 and S4 display peak lateral forces similar in magnitude to the conventional vehicle with 53% PYS.

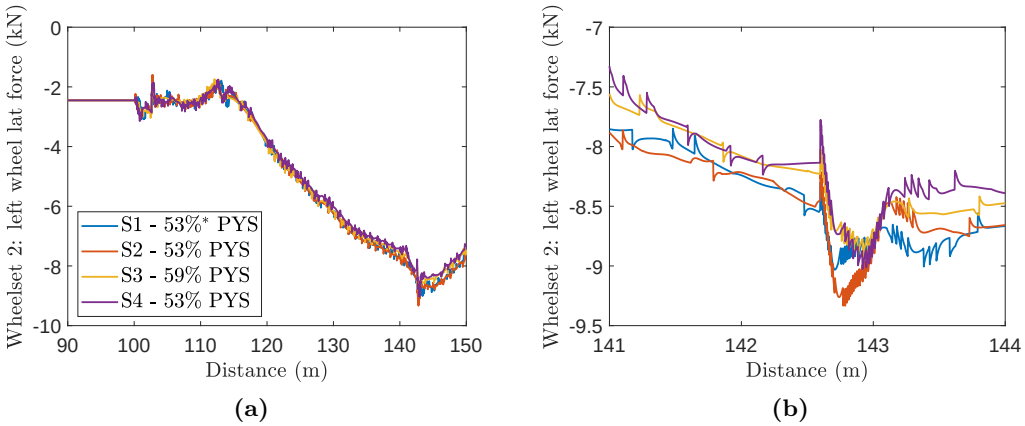

Fig. 6.16 Lateral forces at the left (outer) wheel of wheelset 2 in the initial section of the curve transition. (a) shows the full curve transition (from 100 - 140 m), and (b) shows in more detail the lateral force variations at the start of the transition.

One-off peak lateral irregularities

To further investigate the lateral dynamic behaviour of the inertance-integrated suspensions, VAMPIRE® simulations have been carried out to replicate the lateral dynamic force calculation in the standard: GM/TT0088 *Permissible Track Forces for Railway Vehicles* [122]. GM/TT0088 states that the vehicle must not subject the track to lateral forces greater than:

$$Y_{A_{max}} = \frac{W_L}{3} + 10, \tag{6.2}$$

where Y_A is the lateral force transmitted per axle box, and W_L is the static axle-load. The *BogiePassenger 39t 15yaw* vehicle has a total vehicle mass of 39 tonnes; therefore an axle load of 96 kN, hence, using Eq. (6.2) the maximum lateral force permissible per wheel is 42 kN. GM/TT0088 suggests that the lateral track force calculation must be performed on a vehicle travelling at its maximum speed, at maximum cant deficiency which then encounters a lateral kink with a gradient of 0.0039 rad. The applied cant is 128 mm, the curving radius is 600 m, and the vehicle is travelling at 33.5 ms^{-1}, giving a cant deficiency of 150 mm. The kink has a total span of 6 m, and consists of a lateral ramped track deflection of 11.7 mm. For the simulations presented in this section, again, a new P8 wheel [121], combined with a new CEN60E2 rail has been used, and it should be noted that the kink occurs during the steady state section of the curve.

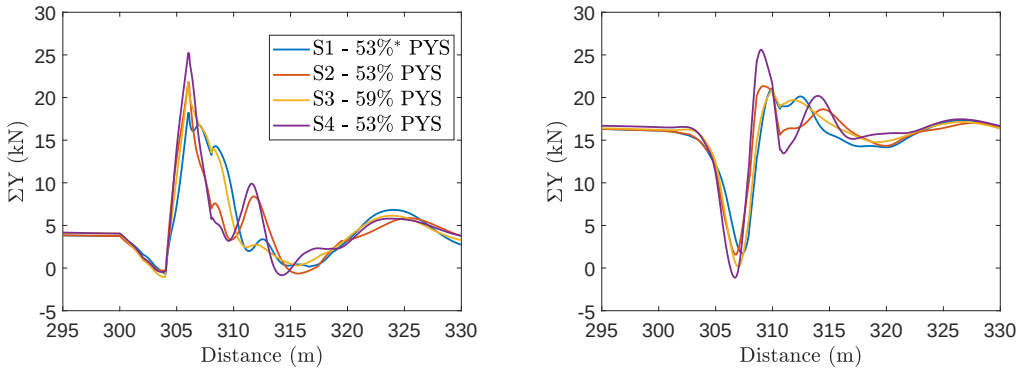

(a) Wheelset 1. **(b)** Wheelset 2.

Fig. 6.17 Total lateral wheelset force on wheelsets 1 and 2, using a 2 m sliding window average, for the optimised inertance-integrated suspensions. Note the S1 configuration has a modified PYS of 53%.

Figure 6.17 shows the sum of the lateral forces across the wheelset, ΣY_A, when the vehicle passes through the kink. The outputs are filtered using a 2 m moving average, as GM/TT0088 states that only lateral forces that are sustained for distances of 2 m or more shall be taken into account in the analysis. It is shown that the inertance-integrated suspension can increase the peak lateral forces, most notably when using the S4 layout, however, for every case it remains significantly lower than the GM/TT0088 limit of 42 kN.

6.4 Summary

The final chapter of this thesis has detailed an investigation into the relative merits of including optimised inertance-integrated suspension devices into a four-axle, VAMPIRE® railway vehicle model. Using MATLAB® and VAMPIRE® in conjunction with one another, for respectively optimisation and simulation purposes, it has been determined that when inerters are included in the lateral component of the trailing arm bush, and certain beneficial suspension configurations are optimised, the PYS is permitted to reduce by up to 47%, equating to a monetary VUC saving of 26%. The passenger comfort remains at an adequate level, or in the most beneficial case it itself reduces by 18.5%. Extra nonlinear testing yields no significant performance detriment.

Using the VAMPIRE® VTISM model detailed in Chapter 3, Section 3.3, beneficial suspension configurations have been chosen using a modified version of the structure-immittance approach. VAMPIRE® and MATLAB® have been combined in the optimisation procedure, with the cost function being PYS, and constraint being RMS lateral carbody acceleration (the passenger comfort measure). Nine speed and conicity combinations are used, to represent a range of operating conditions, and at the seven least critical speed and conicity cases, the passenger comfort constraint has been relaxed by 10%. For a fair comparison, when the default rubber bush is optimised in the suspension, reductions in PYS of only 2% are attainable, however, when the parameter space is widened, and tailored inertance-integrated fluid passageways are employed, the most beneficial layout yields a PYS reduction of 47%. A PYS reduction of this magnitude would allow the VUC to drop by 26% and hence provide significant financial benefit to the railway industry.

The results of nonlinear contact modelling validation conclude that whilst the linear contact model (used in the optimisations) is very useful for increasing computational efficiency for the optimisation, it can over predict the vehicle's lateral dynamic behaviour, especially at higher equivalent conicities. Notwithstanding, when using linear contact modelling, for the case with the highest vehicle speed and wheel conicity, the RMS carbody acceleration was reduced by 18.5% comparing with the default value, and when nonlinear contact modelling checks were carried out, the largest reduction was 12%. In addition, industrial measures such as curved transitions and one-off peak lateral irregularities have been assessed, on the vehicles modelled with nonlinear contact data, to demonstrate that the reduced PYS suspension meets the required performance. Peak counting analysis concludes that all accelerations lie within the safe range, and in curve transitions, only a slight detriment to peak lateral forces is observed, however these values still lie well within legal limits.

The overall conclusion of this project can be drawn from this final technical chapter; namely, there is increasing evidence that including optimised inerter-based devices in the primary suspensions of railway vehicles can allow their PYSs to be reduced, whilst ride quality and other performance criteria are maintained, or also improved. This PYS reduction would in turn reduce track and wheel wear, and diminish the associated maintenance costs.

Chapter 7

Conclusions and future work

This thesis has demonstrated the potential which the inerter can bring to both the vibration suppression and trackwear reduction of railway vehicles. It has been shown, using numerical simulation and optimisation, that beneficial inerter-based lateral suspension configurations permit a significant reduction in PYS, resulting in a VUC saving of 26%, whilst the vehicle's passenger comfort levels are maintained. This chapter summarises the results, findings and conclusions from this work, and also proposes further avenues of research required to aid the progression of this effective passive technology into industry.

7.1 Conclusions

7.1.1 Methods and models

The first technical chapter, Chapter 3, provided a framework of the models and methods that were used throughout this thesis. The first model introduced was the 6 DOF, two-axle, MATLAB® railway vehicle model, typical of a freight vehicle wagon. The inputs to the system were set out as ramped timeseries of track curvature and cant angle, and certain different types of lateral track input, to assess straight running and curving performance respectively. The processes by which these measures were quantified introduced and discussed: both Random and standard (real) rated tracks being used to assess the vehicle's passenger comfort, and T_γ being used as the performance measure for trackwear. Initial assessments of the vehicle's curving performance with the default lateral suspension structure demonstrated that transient carbody accelerations in the transition period are negligible in comparison to the carbody accelerations found in Chapter 4 when assessing straight running performance.

Also in this chapter, the four-axle VAMPIRE® vehicle model was introduced, and aspects such as the suspension layouts and equivalent conicity were discussed. VAMPIRE® was briefly introduced as a widely-used multi-body dynamics modelling

software, with many different file types and their applications to this project discussed. The process by which inerters are modelled in VAMPIRE® was defined and a case study was presented on how to mitigate the end-stiffness effects that the inerter inherently brings, when working in an environment that is predominately made up of mass and spring elements.

The key points to note from Chapter 3 are as follows:

- The MATLAB®, two-axle freight vehicle model was introduced, with curving and straight running performance indices established. It was found that the transient carbody accelerations seen in curved transitions were negligible in comparison with accelerations exhibited when undertaking a straight running assessment.
- A four-axle passenger railway vehicle model was introduced in the commonly used modelling software, VAMPIRE® , and modelling techniques and the concept of equivalent conicity were discussed.
- The implementation of the inerter into VAMPIRE® was validated using a two-mass model, considering inerter end-stiffness and end-damping effects.

7.1.2 Improving trackwear and passenger comfort using optimised inerter-based networks in a simplified two-axle railway vehicle

Whilst Chapter 3 focussed on models and methods, it was shown in Chapter 4 that the incorporation and optimisation of inerter-based structures in the lateral suspension of railway vehicles can concurrently improve passenger comfort and decrease trackwear. It was also discovered that when these optimised lateral suspensions are used in conjunction with an optimised HALL-bush longitudinal suspension structure, the concurrent improvement in both ride comfort and trackwear is further enhanced.

Using the two-axle MATLAB® freight vehicle model introduced in Chapter 3, which has a rated velocity of 31 ms^{-1}, five inerter-based layouts were introduced as candidate lateral suspensions. The different types of track data are assessed and it was discovered that the PSD of the Random Track was focused towards lower frequencies, thus it was decided that Track160 and Track110 (real 5 km lengths of track rated at 160 kph and 110 kph) were to be used for the bulk of the analysis in Chapter 3. RMS lateral carbody acceleration reductions of up to 45% were found to be feasible with the most optimum, lateral inerter-based layouts, using patternsearch and fminsearch optimisation techniques. A continuous velocity assessment of the vehicle dynamics with all optimised devices concluded that the more complex layouts with a single parallel

inerter provide the most benefit to straight running performance, although there is a wide variation in RMS acceleration over all layouts when the vehicle accelerates forwards.

Quantifying trackwear using the energy lost at the wheel-rail contact patch, T_γ, curving analysis in Chapter 4 concluded that whilst the use of inerters in the lateral suspension cannot directly reduce T_γ, it enables the PYS to be reduced whilst also reducing carbody accelerations under straight running conditions, which in turn allows for a reduction in T_γ. Reducing the PYS by 50% and implementing the most beneficial inerter-based layout in the lateral suspension yielded a T_γ reduction of 75% and a passenger comfort improvement of 33%. Further analysis demonstrated that inerter-based configurations in the lateral suspension provide added benefits when an optimised HALL-bush configuration, is used as the longitudinal suspension. Combined with the longitudinal HALL-bush, the passenger comfort improvement rises to 40%. When the most beneficial inerter-based layout was compared to the default lateral layout, both combined with the HALL-bush structure in the longitudinal suspension, a passenger comfort improvement of 25% could be achieved. The vehicle improvements were shown in plots detailing the curving vs straight running performance trade-off, discussed in Section 2.1. It was noted that when the default HALL-bush was used in conjunction with the default lateral suspension structure, both straight running and curving performance improved with reduced PYS, rather than there being a trade-off (see the semi-diagonal dotted black line in Figs. 4.7 and 4.8). This demonstrated that the HALL-bush is already an effective mechanism of combating this underlying trade-off.

The main conclusions that can be drawn from Chapter 4 are as follows:

- When solely optimising passenger comfort, the most beneficial inerter-based suspension layout can provide an RMS lateral carbody acceleration reduction of 45%, when compared to the default layout.
- A continuous velocity assessment concludes that configurations with single parallel inerters provide the most optimum performance across a range of vehicle speeds.
- It has been shown that using optimised inerter-based lateral suspensions permits the PYS to be reduced, which reduces trackwear, yet also decreases carbody acceleration, improving passenger comfort.
- When an optimised HALL-bush longitudinal suspension structure is used in conjunction with the most optimum lateral inerter-based device, the passenger comfort improvement rises to 40% when compared with the default version of

both structures; and 25% when compared with an optimised HALL-bush and default lateral suspension.

7.1.3 The location matrix method of dynamic system simulation

Whilst the analysis and optimisations of Chapter 4 were performed on a two-axle railway vehicle model in MATLAB®, the aim of Chapter 5 was to enable the analysis and optimisation of a more complex and realistic railway vehicle when exported from an industrial piece of software (VAMPIRE®) in MCK matrix form.

Chapter 5 introduced, derived and validated a method for simulating dynamic systems by which interchangeable suspension elements can be incorporated at certain locations via their admittance functions in the Laplace domain, whilst the base mass, stiffness and damping matrices remain unchanged. This Laplace to state-space location matrix method has the potential to allow large scale dynamic systems exported from industrial software to be analysed, and chosen suspension networks with known admittance functions to be optimised for a range of cost functions. This method can be applied when one wishes to optimise suspension parameters that are not already introduced to industrial dynamic systems, and when these systems are highly complex and the equations of motion are near-impossible to decipher. Each simulation step, it was shown to allow an input of the admittance function of a proposed suspension network, however the simulation occurs in time-domain state space-form, avoiding large and challenging matrix inversions and algebraic loops created by introducing inerters. These challenges were extensive during the initial railway vehicle validation phase. The large numbers of DOF involved made the transfer functions within the matrices extremely high in order, resulting in impossible MATLAB® *matrix-of-transfer-functions* inversions. This aspect was the main motivation for developing the location matrix simulation method.

The method developed in Chapter 5 was built on the fact that the location matrix (which defines the coupling positioning of additional suspension networks along with scaling factors) of an additional suspension device can be decomposed into decomposition matrices. When it is not feasible or impossible to correctly infer these matrices from the large dynamic system, eigenvalue decompositions or SVDs take place. Combining these with the non-unique canonical decomposition of the force to acceleration transfer function of the suspension device in question, extra, fictitious, states are introduced to the dynamics, and are present in the final state-space time-domain set of equations.

The method was successfully validated using a simple two-mass MATLAB model, and for a range of inerter and non-inerter based suspension networks, to an extremely high degree of accuracy. Both decomposition techniques yield correct results and

both forcing inputs have been tested. When applied to the VTISM four-axle railway introduced in Chapter 3, a much higher-order model, the system responses to small to medium forcing inputs were deemed correct. However, as the inputs and resulting displacements become higher, the system became more and more nonlinear due to the presence of asymmetric normal forcing at the wheel-rail contact patch. The changes in base stiffness and damping matrices became significant and could no longer be ignored, therefore the location matrix method became less effective at simulating responses.

This method has potential to produce preliminary optimisations for linearised railway vehicle models, however to perform a robust and nonlinear analysis and optimisation of the realistic passenger vehicle model, it was deemed inevitable that the VAMPIRE® simulations would have to be performed at each iteration.

The main conclusions from Chapter 5 are as follows:

- The location matrix method of dynamic system simulation has been established to enable interchangeable and optimisable suspension structures to be applied to complex dynamic systems, at known locations.
- This Laplace-domain to time-domain state space transformation ensures that no algebraic loops (due to inerters in SIMULINK®) arise and that effectively admittance function optimisations (immittance-based approach to network synthesis) can take place on complicated external models.
- The method was successfully validated using a simple two-mass model, and each location matrix decomposition technique yielded very similar results.
- When applied to the exported MCK matrices of the VTISM four axle VAMPIRE model, the method was found to become less accurate as the external forces increased, due to the presence of nonlinearly varying normal contact force variations at the wheel-rail contact patch.

7.1.4 Reducing trackwear on a four-axle industrial model in using a commercially available railway vehicle modelling software, VAMPIRE®

The final chapter of this thesis exhibited an investigation into the relative merits of including optimised inertance-integrated suspension devices into a four-axle, VAMPIRE® railway vehicle model. Using the VAMPIRE® VTISM model, beneficial suspension configurations were chosen using a modified version of the structure-immittance approach. VAMPIRE® and MATLAB® were used in conjunction with one another in the optimisation procedure, with the cost function being PYS, and

constraint being RMS lateral carbody acceleration (the passenger comfort measure). Nine speed and conicity combinations were used, representing a range of operating conditions, and at the seven least critical speed and conicity combinations, the passenger comfort constraint was relaxed by 10%. To form a fair comparison, when the default rubber bush was optimised in the suspension, reductions in PYS of only 2% were attainable, however, when the parameter space is widened, and tailored inertance-integrated fluid passageways were employed, the most beneficial layout permitted a PYS reduction of 47%. A PYS reduction of this magnitude would allow the VUC to drop by 26% and hence benefit to the railway industry significantly.

The results of a set of nonlinear contact modelling validation tests concluded that whilst the linear contact model (used in the optimisations) is very useful for increasing computational efficiency for the optimisation, it was found to over-predict the vehicle's lateral dynamic behaviour, especially at higher equivalent conicities. Nevertheless, when using linear contact modelling, for the case with the highest vehicle speed and wheel conicity, the RMS carbody acceleration was reduced by 18.5% compared with the default value, and when nonlinear contact modelling checks were carried out, the largest reduction was 12%; still significant. In addition, industrial measures such as curved transitions and one-off peak lateral irregularities were assessed on the vehicles modelled with nonlinear contact data to demonstrate that the reduced PYS suspension meets the required performance. Peak counting analysis concluded that all accelerations lie within the safe range, for all conicity and speed combinations, and for both a lateral and vertical acceleration assessment. Finally, in curve transition simulations, only a slight detriment to peak lateral forces was observed; these forces were well within legal limits.

The following conclusions can be drawn from the findings of Chapter 6:

- Using MATLAB® and VAMPIRE® in co-simulation, it has been discovered that with the use of optimised inertance-based lateral suspensions, the PYS can be reduced by up to 47%, whilst the passenger comfort remains at a satisfactory level, and at the most critical conicity and speed combination, the passenger comfort improves by 18%.
- Validation testing using nonlinear contact modelling yield lower acceleration values in general, due to the fact that equivalent conicity is measured at a 3 mm lateral offset, and PSD analyses consolidate the improved performance.
- Industry standard tests (such as peak counting, curved transitions and one-off peak lateral irregularities) have been performed on the optimised vehicles and no significant detriment to performance has been discovered.

7.2 Future work

The main finding of this thesis is as follows:

Including optimised inertance-integrated devices in the primary suspensions of railway vehicles can allow their Primary Yaw Stiffnesses to be reduced, reducing track and wheel maintenance costs, whilst ride quality and other performance criteria are maintained, or also improved.

This statement, and the project in general, forms a preliminary step towards to the inclusion of inerters in railway vehicle suspension systems. There is a significant amount of further analysis, validation, and decision making that needs to be performed, however, before industry can be confident in investing in such technologies, as the overall monetary savings, and the secondary improvements from a customer satisfaction perspective due to reduced amounts of maintenance work disruptions, need to outweigh the costs of such a step-change in infrastructure. This section briefly proposes such research and development work.

7.2.1 Optimisation and vehicle modelling development

Firstly, it is suggested that the optimisation procedure itself has potential for improvement and updating. The list of potential constraints and performance criteria for optimisation (such as many different types of stability, critical speed, passenger comfort, trackwear) is an extremely long one, therefore care must be taken when deciding which to analyse in the optimisations. Also, from a practical perspective, there is only so much theoretical analysis and optimisation that one should realistically dedicate time to, pre the validation testing phase, as slight discrepancies in performance will inevitably arise from unpredictable factors which may occur when inerters are implemented, or for a number of other reasons. Improved computational efficiency will enhance the optimisations further, and it is suggested that further optimisations should be performed on a vehicle model which includes a complete representation of wheel rail contact. This model would utilise actual wheel and rail profiles, hence nonlinear rrd, along with flange contact and creep force saturation techniques. Furthermore, consideration should also be given to how the inerter affects the vehicle's dynamics closer to it's kinematic stability boundary; with a greater emphasis on curving performance. This would effectively push the solution towards the outer portion of its performance envelope in relation to the steering vs stability compromise. Also, increasing the number of layouts optimised over increases the likelihood of enabling a yet further decreased PYS. However, as mentioned in the latter part of this section, the feasibility of physically assembling these beneficial configurations into the vehicles should be taken into account.

The analysis would also benefit from some form of weighting placed on each conicity and velocity in the optimisations, as some combinations are inherently more critical than others. This has been done to an extent in this thesis, by capping the permissible carbody acceleration increase at zero for the highest speeds and conicity, and introducing a 10% relaxed constraint for all other cases. However, a deeper investigation into how permissible higher levels of acceleration at lower conicities are is required. Expertise from industry would be beneficial when deciding on factors such as these. Future *industry standard* studies would benefit from identifying the benefits that inerter-based suspensions can bring over optimised lateral suspensions with an optimised longitudinal HALL-bush included. This would strengthen the case to industry that the inerter's addition outweighs that of merely a longitudinal HALL-bush. Note that this has been established already on a simplified two-axle model in Chapter 4.

Inerters have been proven beneficial to vertical passenger comfort when implemented in the vertical suspension, using a simplified two-axle model [103], therefore further research on an industry standard model would benefit from similar analysis, even potentially including inerters in the longitudinal direction. Within this analysis, it would be highly beneficial to include a cyclic-top style assessment, where a vehicle bounces and causes dips in the rail due to vertical track irregularities, as the results would be heavily dependent on the vehicle's vertical suspension. Furthermore, the most natural next step from a vehicle modelling point of view is to consider a *real world* vehicle (a Mark 4 coach for example) rather than a partially simplified VTISM library model.

7.2.2 Physical suspension realisations

One of the most important questions that will no doubt be posed when it comes to the real-world application of inertance-integrated suspensions is how the beneficial configurations will be realised in a fluid passageway bushing structure, and how these devices will be physically implemented into the trailing-arm bush structure.

A reverse engineering approach utilising hydraulic to mechanical network synthesis is likely to be employed, leading to optimisable design parameters of piston area, chamber volumetric stiffness, and inertia track geometry (providing the inertance) rather than the original parameters (stiffness, damping and inertance). The parameter space (i.e the upper and lower bounds) for each of these aspects is highly dependent on the type of combined fluid passageway bushing device that is used, and the amount of space which is available to insert such a device.

Regarding physical implementation, it is anticipated that feasibility studies will need to be conducted on the extent to which current bogies will either need to be re-designed, or retrofitted; the outcomes of which will have a large impact on costing, manufacturing, and the time-scale of implementation.

7.2.3 Validation testing

One of the latter stages in readying the proposed inertance-integrated suspensions for industrial uptake is the experimental testing of scaled and full-scale prototypes in environments similar to those which railway vehicles would experience in the real world. The first phase of this testing is likely to be of a sub-structuring nature, involving scaled inertance-integrated suspension prototypes. After this initial validation, the next phase of physical implementation is anticipated to be on a full-scale roller-rig. Once the benefits of such a suspension have been successfully validated in this harsh, real world environment, the technology has much potential to be adopted across the industry and bring a step change to railway vehicle performance.

References

[1] M. Burstow, VTAC calculator: Guidance note for determining t_γ values, available at https://cdn.networkrail.co.uk/wp-content/uploads/2016/12/VTAC-calculator-Guidance-note-for-determining-Tgamma-values.pdf (2012).

[2] Network Rail, Cp5 vuc calculator (current prices, february 2017), Tech. rep., Network Rail (2017).
URL https://www.networkrail.co.uk/industry-commercial-partners/information-operating-companies/cp5-access-charges/

[3] S. Iwnicki, Handbook of Railway Vehicle Dynamics, Taylor & Francis Group, 2006.

[4] M. Dumitriu, A nonlinear model of mix coil spring-rubber for vertical suspension of railway vehicle, Archive of Mechanical Engineering March 2016.

[5] M. Firat, M. Ozsoy, U. Kocabicak, E. Aba, The study on the dynamic characteristics of a railway suspension system by complete vehicle modelling, in: Trends in the Development of Machinary and Associated Technology, 2005.

[6] T. Michalek, J. Zelenka, The effect of spring pads in the secondary suspension of railway vehicles on bogie yaw resistance, Vehicle System Dynamics 53 (12) (2015) 1952–1964.

[7] RSSB Research Programme, Vtism stage 2 summary report, Tech. rep., RSSB (2010).
URL https://www.rssb.co.uk/research-development-and-innovation/research-reports-catalogue/pb009847

[8] M. Dumitriu, On the assessment of the vertical vibration behaviour of a railway vehicle, Romanian Journal of Acoustics and Vibration 8(2) (2011) 131–138.

[9] J. Evans, Application of the “hall” hydraulic radial arm bush to a 200 km/h inter-city coach, in: International Symposium on Dynamics of Vehicle on Road and Tracks, IAVSD, 2011.

[10] M. Hiensch, P. Wiersma, M. Linders, A. Zoeteman, W. van Ravenswaay, Improving track-friendliness of rolling stock, in: IHHA, Perth, Australia, 2015.

[11] M. Burstow, Whole life rail model application and development: Development of a rolling contact fatigue damage parameter (2003).

[12] M. Burstow, A model to predict and understand rolling contact fatigue in wheels and rails, in: WCRR, Montreal, Canada, 2006.

[13] P. Boyacioglu, A. Bevan, A. Vickerstaff, Prediction of rcf damage on underground metro lines, in: First International Conference on Rail Transportation, 2017.
URL http://eprints.hud.ac.uk/id/eprint/32550/

[14] R. Goodall, Tilting trains and beyond - the future for active railway suspensions part 1 improving passenger comfort, Computing & Control Engineering Journal August, 1999.

[15] R. Goodall, Tilting trains and beyond - the future for active railway suspensions part 2 improving stability and guidance, Computing & Control Engineering Journal October, 1999.

[16] R. Goodall, T. X. Mei, Mechatronic strategies for controlling railway wheelsets with independently rotating wheels, in: 2001 IEEWASME International Conference on Advanced Intelligent Mechatronics Proceedings 6-12 July 2001 Como, Italy, 2001, pp. 225–230.

[17] T. X. Mei, R. M. Goodall, Practical strategies for controlling railway wheelsets with independently rotating wheels, Journal of Dynamic Systems, Measurement, and Control 125 (203) 354–360.

[18] T. X. Mei, R. M. Goodall, Robust control for independently rotating wheelsets on a railway vehicle using practical sensors, IEEE Transactions on Control Systems Technology 9(4) (2001) 599–607.

[19] A. C. Mellando, C. Casanueva, J. Vinolas, J. G. Gimenez, A lateral active suspension for conventional railway bogies, Vehicle System Dynamics January 2009.

[20] R. Zhou, A. Zolotas, R. Goodall, H-infinity based control system and its digital implementation for the integrated tilt with active lateral secondary suspensions in high speed trains, in: Proceedings of the 32nd Chinese Control Conference, 2013.

[21] H. Li, Measuring systems for active steering of railway vehicles, Ph.D. thesis, Loughborough University (2001).

[22] F. A. Firestone, A new analogy between mechanical and electrical systems, The Journal of the Acoustical Society of America 4 (3) (1933) 249–267. doi:10.1121/1.1915605.
URL https://doi.org/10.1121/1.1915605

[23] M. Smith, Synthesis of mechanical networks: The inerter, IEEE Transactions on Automatic Control 47(10) (2002) 1648–1662.

[24] B. Otto, Synthesis of a finite two-terminal network whose driving-point impedance is a prescribed function of frequency, Journal of Mathematics and Physics 10 (1-4) 191–236. arXiv:https://onlinelibrary.wiley.com/doi/pdf/10.1002/sapm1931101191, doi:10.1002/sapm1931101191.
URL https://onlinelibrary.wiley.com/doi/abs/10.1002/sapm1931101191

[25] C. Papageorgiou, N. E. Houghton, M. C. Smith, Experimental Testing and Analysis of Inerter Devices, Journal of Dynamic Systems, Measurement, and Control 131 (1), 011001. arXiv:https://asmedigitalcollection.asme.org/dynamicsystems/article-pdf/131/1/011001/4786089/011001_1.pdf, doi:10.1115/1.3023120.
URL https://doi.org/10.1115/1.3023120

[26] C. Papageorgiou, M. C. Smith, Laboratory experimental testing of inerters, in: Proceedings of the 44th IEEE Conference on Decision and Control, 2005, pp. 3351–3356. doi:10.1109/CDC.2005.1582679.

[27] A. Gonzalez-Buelga, I. F. Lazar, J. Z. Jiang, S. A. Neild, D. J. Inman, Assessing the effect of nonlinearities on the performance of a tuned inerter damper, Structural Control and Health Monitoring 24 (3) (2017) e1879, e1879 STC-15-0213.R1. arXiv:https://onlinelibrary.wiley.com/doi/pdf/10.1002/stc.1879, doi:10.1002/stc.1879.
URL https://onlinelibrary.wiley.com/doi/abs/10.1002/stc.1879

[28] F.-C. Wang, W.-J. Su, Impact of inerter nonlinearities on vehicle suspension control, Vehicle System Dynamics - VEH SYST DYN 46 (2008) 575–595. doi:10.1080/00423110701519031.

[29] P. M. Components, Catalog of nsk ballscrew,.

[30] X. Liu, J. Z. Jiang, B. Titurus, H. J Andrew, Model identification methodology for fluid-based inerters, Mechanical Systems and Signal Processing 106. doi:10.1016/j.ymssp.2018.01.018.

[31] F.-C. Wang, M.-F. Hong, Y. C. Lin, Designing and testing a hydraulic inerter, IMECHE Mechanical Engineering Science 225 (2010) 66–72.

[32] S. J. Swift, M. C. Smith, A. R. Glover, C. Papageorgiou, B. Gartner, N. E.Houghton, Design and modelling of a fluid inerter, International Journal of Control 86(11) (2013) 2035–2051.

[33] F.-C. Wang, C.-W. Chen, M.-K. Liao, M.-F. Hong, Performance analyses of building suspension control with inerters, 46th IEEE Conference on Decision and Control.

[34] K. Ikago, K. Saito, N. Inoue, Seismic control of single-degree-of-freedom structure using tuned viscous mass damper, Earthquake Engineering & Structural Dynamics 41 (3) (2012) 453–474. arXiv:https://onlinelibrary.wiley.com/doi/pdf/10.1002/eqe.1138, doi:10.1002/eqe.1138.
URL https://onlinelibrary.wiley.com/doi/abs/10.1002/eqe.1138

[35] I. F. Lazar, S. A. Neild, D. J. Wagg, Using an inerter-based device for structural vibration suppression, Earthquake Engineering and Structural Dynamics 43 (2014) 1129–1147.

[36] J. Storer, Passive network synthesis, McGraw-Hill electrical and electronic engineering series, McGraw-Hill, 1957.
URL https://books.google.co.uk/books?id=LaI8AAAAIAAJ

[37] M. Van Valkenburg, Introduction to modern network synthesis, no. v. 1, Wiley, 1960.
URL https://books.google.co.uk/books?id=CuBSAAAAMAAJ

[38] R. Bott, R. J. Duffin, Impedance synthesis without use of transformers, Journal of Applied Physics 20 (8) (1949) 816–816. arXiv:https://doi.org/10.1063/1.1698532, doi:10.1063/1.1698532.
URL https://doi.org/10.1063/1.1698532

[39] S. Y. Zhang, J. Z. Jiang, S. Neild, Optimal configurations for a linear vibration suppression device in a multi-storey building, Structural Control and Health Monitoring 24 (3) (2017) e1887–n/a, e1887 STC-16-0018.R2. doi:10.1002/stc.1887.
URL http://dx.doi.org/10.1002/stc.1887

[40] F.-C. Wang, H.-A. Chan, Vehicle suspensions with a mechatronic network strut, Vehicle System Dynamics 49(5) (2011) 811–830.

[41] C. Papageorgiou, M. C. Smith, Positive real synthesis using matrix inequalities for mechanical networks: application to vehicle suspension, IEEE Transactions on Control Systems Technology 14 (3) (2006) 423–435. doi:10.1109/TCST.2005.863663.

[42] F.-C. Wang, M.-K. Liao, B.-H. Liao, W.-J. Su, H.-A. Chan, The performance improvements of train suspension systems with mechanical networks employing inerters, Vehicle System Dynamics 47 (7) (2009) 805–830. arXiv:https://doi.org/10.1080/00423110802385951, doi:10.1080/00423110802385951.
URL https://doi.org/10.1080/00423110802385951

[43] J. Z. Jiang, M. C. Smith, Regular positive-real functions and five-element network synthesis for electrical and mechanical networks, IEEE Transactions on Automatic Control 56 (6) (2011) 1275–1290. doi:10.1109/TAC.2010.2077810.

[44] J. Z. Jiang, M. C. Smith, Series-parallel six-element synthesis of biquadratic impedances, IEEE Transactions on Circuits and Systems I: Regular Papers 59 (11) (2012) 2543–2554. doi:10.1109/TCSI.2012.2206492.

[45] J. Z. Jiang, M. C. Smith, On the theorem of reichert, Systems and Control Letters 61 (12) (2012) 1124 – 1131. doi:https://doi.org/10.1016/j.sysconle.2012.09.009.
URL http://www.sciencedirect.com/science/article/pii/S0167691112001880

[46] S. Y. Zhang, J. Z. Jiang, S. A. Neild, Passive vibration control: a structure–immittance approach, Proceedings of the Royal Society A: Mathematical, Physical and Engineering Sciences 473 (2201) (2017) 20170011. arXiv:https://royalsocietypublishing.org/doi/pdf/10.1098/rspa.2017.0011, doi:10.1098/rspa.2017.0011.
URL https://royalsocietypublishing.org/doi/abs/10.1098/rspa.2017.0011

[47] S. McBeath, Shocks to the system: three years on from the j-damper story penske racing shocks announces its hybrid damper/inerter for wider application, Racecar Engineering November (2011) 51–56.

[48] U. of Cambridge, Secrets of the inerter revealed (Aug 2008).
URL http://www.sciencedirect.com/science/article/pii/S0167691112001880

[49] F. Sport, The fia's decision on the spy scandal (2007).
URL https://www.fia.com/mediacentre/Press_Releases/FIA_Sport/2007/December/071207-01

[50] M. Hughes, A genius idea, and why mclaren hasn't tried to stop others using it, Autosport J.

[51] C. Scarborough, Technical insight: Renault's j-damper, Earthquake Engineering & Structural Dynamics.

[52] M. Z. Q. Chen, C. Papageorgiou, F. Scheibe, F.-C. Wang, M. C. Smith, The missing mechanical circuit element, IEEE Circuits and Sytems Magazine.

[53] M. C. Smith, F.-C. Wang, Performance benefits in passive vehicle suspensions employing inerters, Vehicle System Dynamics 42 (4) (2004) 235–257. arXiv:https://doi.org/10.1080/00423110412331289871, doi:10.1080/00423110412331289871.
URL https://doi.org/10.1080/00423110412331289871

[54] F. Scheibe, M. Smith, Analytical solutions for optimal ride comfort and tyre grip for passive vehicle suspensions, Vehicle System Dynamics 47(10) (2009) 1229–1252.

[55] Y. Hu, M. Z. Chen, Z. Shu, Passive vehicle suspensions employing inerters with multiple performance requirements, Journal of Sound and Vibration 333 (8) (2014) 2212 – 2225. doi:https://doi.org/10.1016/j.jsv.2013.12.016.
URL http://www.sciencedirect.com/science/article/pii/S0022460X13010560

[56] A. Kuznetsov, M. Mammadov, I. Sultan, E. Hajilarov, Optimization of improved suspension system with inerter device of the quarter-car model in vibration analysis, Archive of Applied Mechanics 81 (10) (2011) 1427–1437. doi:10.1007/s00419-010-0492-x.
URL https://doi.org/10.1007/s00419-010-0492-x

[57] Y. Shen, L. Chen, X. Yang, D. Shi, J. Yang, Improved design of dynamic vibration absorber by using the inerter and its application in vehicle suspension, Journal of Sound and Vibration 361 (2016) 148 – 158. doi:https://doi.org/10.1016/j.jsv.2015.06.045.
URL http://www.sciencedirect.com/science/article/pii/S0022460X15005465

[58] S. Evangelou, D. J. N. Limebeer, R. S. Sharp, M. C. Smith, Mechanical Steering Compensators for High-Performance Motorcycles, Journal of Applied Mechanics 74 (2) (2006) 332–346. arXiv:https://asmedigitalcollection.asme.org/appliedmechanics/article-pdf/74/2/332/4742756/332_1.pdf, doi:10.1115/1.2198547.
URL https://doi.org/10.1115/1.2198547

[59] S. Evangelou, D. J. N. Limebeer, R. S. Sharp, M. C. Smith, Control of motorcycle steering instabilities, IEEE Control Systems Magazine 26 (5) (2006) 78–88. doi:10.1109/MCS.2006.1700046.

[60] X.-J. Zhang, S. A. Neild, M. Ahmadian, K.-H. Guo, On the benefits of semi-active suspensions with inerters, Shock and Vibration 19 (3) (2012) 257–272.
URL https://doi.org/10.3233/SAV-2011-0628

[61] M. Z. Q. Chen, Y. Hu, C. Li, G. Chen, Performance benefits of using inerter in semiactive suspensions, IEEE Transactions on Control Systems Technology 23 (4) (2015) 1571–1577. doi:10.1109/TCST.2014.2364954.

[62] P. Li, J. Lam, K. C. Cheung, Control of vehicle suspension using an adaptive inerter, Proceedings of the Institution of Mechanical Engineers, Part D: Journal of Automobile Engineering 229 (14) (2015) 1934–1943. arXiv:https://doi.org/10.1177/0954407015574808, doi:10.1177/0954407015574808.
URL https://doi.org/10.1177/0954407015574808

[63] M. Zilletti, Feedback control unit with an inerter proof-mass electrodynamic actuator, Journal of Sound and Vibration 369 (2016) 16 – 28. doi:https://doi.org/10.1016/j.jsv.2016.01.035.
URL http://www.sciencedirect.com/science/article/pii/S0022460X1600064X

[64] C. P. Szczyglowski, S. A. Neild, B. Titurus, J. Z. Jiang, E. Coetzee, Passive gust loads alleviation in a truss-braced wing using an inerter-based device, Journal of Aircraft 0 (0) (2019) 1–12. arXiv:https://doi.org/10.2514/1.C035452, doi:10.2514/1.C035452.
URL https://doi.org/10.2514/1.C035452

[65] X. Dong, Y. Liu, M. Z. Q. Chen, Application of inerter to aircraft landing gear suspension, in: 2015 34th Chinese Control Conference (CCC), 2015, pp. 2066–2071. doi:10.1109/ChiCC.2015.7259953.

[66] Y. Liu, M. Z. Q. Chen, Y. Tian, Nonlinearities in landing gear model incorporating inerter, in: 2015 IEEE International Conference on Information and Automation, 2015, pp. 696–701. doi:10.1109/ICInfA.2015.7279375.

[67] Y. Li, J. Jiang, S. Neild, H. Wang, Optimal inerter-based shock-strut configurations for landing gear touch-down performance, Journal of Aircraft 54 (5) (2017) 1901–1909. doi:10.2514/1.C034276.

[68] Y. Li, J. Jiang, P. Sartor, S. Neild, H. Wang, Including inerters in aircraft landing gear shock strut to improve the touch-down performance, Procedia Engineering 199 (2017) 1689–1694, type: Conference proceeding. doi:10.1016/j.proeng.2017.09.366.

[69] Y. Li, J. Z. Jiang, S. Neild, Inerter-based configurations for main landing gear shimmy suppression, N/A N/A (2016) N/A.

[70] Y. Li, C. Howcroft, S. Neild, J. Jiang, Using continuation analysis to identify shimmy-suppression devices for an aircraft main landing gear, Journal of Sound and Vibration 408 (2017) 234–251. doi:10.1016/j.jsv.2017.07.028.

[71] H. Frahm, Device for damping vibration of bodies, u.S. patent 989,958 (2005).

[72] J. Den Hartog, Mechanical Vibrations, Civil, Mechanical and Other Engineering Series, Dover Publications, 1985.
URL https://books.google.co.uk/books?id=-Pu5YlgY4QsC

[73] F. Sadek, B. Mohraz, A. W. Taylor, R. M. Chung, A method of estimating the parameters of tuned mass dampers for seismic applications, Earthquake Engineering & Structural Dynamics 26 (6) (1997) 617–635. doi:10.1002/(SICI)1096-9845(199706)26:6<617::AID-EQE664>3.0.CO;2-Z.

[74] S. Krenk, J. B. Hogsberg, Tuned mass dampers on damped structures (2008).

[75] N. Hoang, P. Warnitchai, Design of multiple tuned mass dampers by using a numerical optimizer, Earthquake Engineering & Structural Dynamics 34 (2) (2005) 125–144. doi:10.1002/eqe.413.

[76] S. Krenk, J. Hogsberg, Tuned mass absorber on a flexible structure, Journal of Sound and Vibration 333 (2014) 1577–1595.

[77] T. Detroux, G. Habib, L. Masset, G. Kerschen, Performance, robustness and sensitivity analysis of the nonlinear tuned vibration absorber, Mechanical Systems and Signal Processing 60-61 (2015) 799–809.

[78] N. A. Alexander, F. Schilder, Exploring the performance of a nonlinear tuned mass damper, Journal of Sound and Vibration 319 (2009) 445–462.

[79] P. Soltani, G. Kerschen, The nonlinear piezoelectric tuned vibration absorber, Smart Materials and Structures 24 (075015).

[80] G. Habib, G. Kerschen, Suppression of limit cycle oscillations using the nonlinear tuned vibration absorber 471 (2176).

[81] F.-C. Wang, M.-F. Hong, C.-W. Chen, Building suspensions with inerters, Proceedings of the Institution of Mechanical Engineers, Part C: Journal of Mechanical Engineering Science 224 (8) (2010) 1605–1616. arXiv:https://doi.

org/10.1243/09544062JMES1909, doi:10.1243/09544062JMES1909.
URL https://doi.org/10.1243/09544062JMES1909

[82] I. Takewaki, S. Murakami, S. Yoshitomi, M. Tsuji, Fundamental mechanism of earthquake response reduction in building structures with inertial dampers, Structural Control and Health Monitoring 19 (6) (2012) 590–608. arXiv:https://onlinelibrary.wiley.com/doi/pdf/10.1002/stc.457, doi:10.1002/stc.457.
URL https://onlinelibrary.wiley.com/doi/abs/10.1002/stc.457

[83] T. Furuhashi, S. Ishimaru, Mode control seismic design with dynamic mass, in: Proceedings of the 14th World Conference on Earthquake Engineering, 2008.

[84] K. Ikago, Y. Sugimura, K. Saito, N. Inoue, Modal response characteristics of a multiple-degree-of-freedom structure incorporated with tuned viscous mass dampers, Journal of Asian Architecture and Building Engineering 11 (2) (2012) 375–382. arXiv:https://doi.org/10.3130/jaabe.11.375, doi:10.3130/jaabe.11.375.
URL https://doi.org/10.3130/jaabe.11.375

[85] A. Gonzalez-Buelga, L. R. Clare, S. A. Neild, J. Z. Jiang, D. J. Inman, An electromagnetic inerter-based vibration suppression device, Smart Materials and Structures 24.

[86] L. Marian, A. Giaralis, Optimal design of a novel tuned mass-damper–inerter (tmdi) passive vibration control configuration for stochastically support-excited structural systems, Probabilistic Engineering Mechanics 38 (2014) 156–164.

[87] A. Giaralis, A. A. Taflanidis, Reliability-based design of tuned mass-damper-inerter (tmdi) equipped multi-storey frame buildings under seismic excitation (Jul 2015).

[88] A. Giaralis, F. Petrini, Wind-induced vibration mitigation in tall buildings using the tuned mass-damper-inerter, Journal of Structural Engineering 143 (9) (2017) 04017127.

[89] H. Garrido, O. Curadelli, D. Ambrosini, Improvement of tuned mass damper by using rotational inertia through tuned viscous mass damper, Engineering Structures 56 (2013) 2149 – 2153. doi:https://doi.org/10.1016/j.engstruct.2013.08.044.
URL http://www.sciencedirect.com/science/article/pii/S0141029613004112

[90] R. M. Hessabi, O. Mercan, Investigations of the application of gyro-mass dampers with various types of supplemental dampers for vibration control of building structures, Engineering Structures 126 (2016) 174 – 186. doi:https://doi.org/10.1016/j.engstruct.2016.07.045.
URL http://www.sciencedirect.com/science/article/pii/S0141029616303819

[91] Y. Hu, M. Z. Q. Chen, Inerter-based passive structural control for load mitigation of wind turbines, in: 2017 29th Chinese Control And Decision Conference (CCDC), 2017, pp. 3056–3061. doi:10.1109/CCDC.2017.7979033.

[92] Y. Hu, M. Z. Q. Chen, Passive structural control with inerters for a floating offshore wind turbine, in: 2017 36th Chinese Control Conference (CCC), 2017, pp. 9266–9271. doi:10.23919/ChiCC.2017.8028833.

[93] N. Alujević, D. Čakmak, H. Wolf, M. Jokić, Passive and active vibration isolation systems using inerter, Journal of Sound and Vibration 418 (2018) 163 – 183.

doi:https://doi.org/10.1016/j.jsv.2017.12.031.
URL http://www.sciencedirect.com/science/article/pii/S0022460X17308908

[94] J. Luo, J. H. Macdonald, J. Z. Jiang, Use of inerter-based vibration absorbers for suppressing multiple cable modes, Procedia Engineering 199 (2017) 1695 – 1700, x International Conference on Structural Dynamics, EURODYN 2017. doi:https://doi.org/10.1016/j.proeng.2017.09.370.
URL http://www.sciencedirect.com/science/article/pii/S1877705817338602

[95] I. Lazar, S. Neild, D. Wagg, Vibration suppression of cables using tuned inerter dampers, Engineering Structures 122 (2016) 62 – 71. doi:https://doi.org/10.1016/j.engstruct.2016.04.017.
URL http://www.sciencedirect.com/science/article/pii/S0141029616301286

[96] L. Sun, D. Hong, L. Chen, Cables interconnected with tuned inerter damper for vibration mitigation, Engineering Structures 151 (2017) 57 – 67. doi:https://doi.org/10.1016/j.engstruct.2017.08.009.
URL http://www.sciencedirect.com/science/article/pii/S0141029617300743

[97] F.-C. Wang, M.-K. Liao, The lateral stability of train suspension systems employing inerters, Vehicle System Dynamics 48 (5) (2010) 619–643. arXiv:https://doi.org/10.1080/00423110902993654, doi:10.1080/00423110902993654.
URL https://doi.org/10.1080/00423110902993654

[98] F.-C. Wang, M.-R. Hsieh, H.-J. Chen, Stability and performance analysis of a full-train system with inerters, Vehicle System Dynamics 50 (4) (2012) 545–571. arXiv:https://doi.org/10.1080/00423114.2011.606368, doi:10.1080/00423114.2011.606368.
URL https://doi.org/10.1080/00423114.2011.606368

[99] A. Z. Matamoros-Sanchez, R. M. Goodall, Novel mechatronic solutions incorporating inerters for railway vehicle vertical secondary suspensions, Vehicle System Dynamics 53 (2) (2015) 113–136. arXiv:https://doi.org/10.1080/00423114.2014.983529, doi:10.1080/00423114.2014.983529.
URL https://doi.org/10.1080/00423114.2014.983529

[100] J. Z. Jiang, A. Z. Matamoros-Sanchez, R. M. Goodall, M. C. Smith, Performance benefits in two-axle railway vehicle suspensions, Institution of Engineering and Technology, 2012, Ch. 11.

[101] J. Jiang, T. Mei, M. Smith, Curving performance for railway vehicles with advanced passive suspensions, in: 23rd International Symposium on Dynamics of Vehicle on Road and Tracks, IAVSD, 2013.

[102] J. Z. Jiang, A. Z. Matamoros-Sanchez, R. M. Goodall, M. C. Smith, Passive suspensions incorporating inerters for railway vehicles, Vehicle System Dynamics: International Journal of Vehicle Mechanics and Mobility 50:sup1) (2012) 263–276.

[103] J. Z. Jiang, A. Z. Matamoros-Sanchez, A. Zolotas, R. M. Goodall, M. C. Smith, Passive suspensions for ride quality improvement of two-axle railway vehicles, IMECHE: Journal of Rail and Rapid Transit 229(3) (2015) 315–329.

[104] A. Z. Matamoros-Sanchez, R. M. Goodaoll, Applications of the inerter in railway vehicle suspension, in: 2014 UKACC International Conference on Control (CONTROL), 2014, pp. 555–560. doi:10.1109/CONTROL.2014.6915200.

[105] Y. Zhao, G. Tucker, R. Goodall, S. Iwnicki, J. Jiang, M. Smith, Developing an inerter model using multibody dynamics software, in: 25th International Symposium on Dynamics of Vehicle on Road and Tracks, IAVSD, 2017.

[106] Resonate, Vampire help manual, Tech. rep., DeltaRail Group Limited (2016).

[107] British-Adopted European Standard, BS EN 12299:2009, Railway applications. Ride comfort for passengers. Measurement and evaluation, 2009.

[108] B. Kufver, R. Persson, J. Wingren, Certain aspects of the cen standard for the evaluation of ride comfort for rail passengers, 2010, pp. 605–614. doi:10.2495/CR100561.

[109] J. J. Kalker, The computation of three-dimensional rolling contact with dry friction, International Journal for Numerical Methods in Engineering 14 (9) (1979) 1293–1307. doi:10.1002/nme.1620140904.
URL http://dx.doi.org/10.1002/nme.1620140904

[110] Prediction of wheel profile wear, Wear 144 (1) (1991) 343 – 351. doi:https://doi.org/10.1016/0043-1648(91)90025-P.
URL http://www.sciencedirect.com/science/article/pii/004316489190025P

[111] R. Licciardello, G. Malavasi, S. Ricci, P. Vitali, Wear rates in urban rail systems, 2017, pp. 559–569. doi:10.2495/UT170481.

[112] W. Klingel, Uber den lauf der eisenbahnwagen auf gerader bahn, Organ fur die Fortschritte des Eisenbahnwesens in technischer Beziehung 20 (1883) 113–123.

[113] British Standard, BS EN 15302:2008+A1:2010, Railway applications. Method for determining the equivalent conicity, 2008.

[114] F. F. Kuo, Network Analysis and Synthesis, 2nd Edition, John Wiley and Sons, 1962.

[115] RSSB, Bogiepassenger39t15yaw vehicle model (2010).
URL https://www.rssb.co.uk/research-development-and-innovation/research-reports-catalogue/pb009847

[116] S. Y. Zhang, J. Z. Jiang, S. A. Neild, The structure-immittance approach for passive vibration control, Procedia Engineering 199 (2017) 1834 – 1839, x International Conference on Structural Dynamics, EURODYN 2017. doi:https://doi.org/10.1016/j.proeng.2017.09.099.
URL http://www.sciencedirect.com/science/article/pii/S187770581733535X

[117] S. J. Swift, M. C. Smith, A. R. Glover, C. Papageorgiou, B. Gartner, N. E. Houghton, Design and modelling of a fluid inerter, International Journal of Control 86 (11) (2013) 2035–2051. arXiv:https://doi.org/10.1080/00207179.2013.842263, doi:10.1080/00207179.2013.842263.
URL https://doi.org/10.1080/00207179.2013.842263

[118] Research and Development Programme RSSB, Controlling rail vertical contact stresses, Tech. rep., RSSB (2011).
URL https://www.rssb.co.uk/library/research-development-and-innovation/research-brief-T889.pdf

[119] R. Illingworth, Resistance of railway vehicles to derailment and roll-over: Gm/rt2141 (1998).

[120] Railway Group Standard, Track system requirements: Gc/rt5021 (2011).

[121] British Railways Board, Railway wheelsets: Gmrt2466 (2017).

[122] British Railways Board, Permissible track forces for railway vehicles: Gmtt0088 (1993).